Single-molecule studies of nucleic acid dynamics using carbon nanotube-based field-effect transistors

Nathan Scott Daly

Submitted in partial fulfillment of the

requirements for the degree

of Doctor of Philosophy

in the Graduate School of Arts and Sciences

COLUMBIA UNIVERSITY

2017

ABSTRACT

Single-molecule studies of nucleic acid dynamics using carbon nanotube-based field-effect transistors

Nathan Scott Daly

This thesis describes the development and implementation of single-molecule carbon nanotube-based field-effect transistors (smFETs) for studies of nucleic acid dynamics. Single-molecule techniques, most notably fluorescence resonance energy transfer (smFRET) and single-molecule force spectroscopy, have been employed to investigate biomolecular dynamics due to their ability to directly observe discrete, rare events, as well as to characterize structural motions in a diverse ensemble. However, these techniques are hampered by difficulties in measuring millisecond-scale dynamics, such as base pair rearrangements, as well as the inability to observe unperturbed individual molecules for long times. Alternatively, smFETs allow observation of the dynamics of charged biomolecules, such as charged amino acids in proteins or the phosphate groups of nucleic acid backbones, with microsecond temporal resolution. Structural rearrangements of a single charged molecule on the surface of a single-walled carbon nanotube (CNT) transistor can lead to measureable fluctuations in conductance through the CNT. Thus, this technique allows for simultaneous characterization of fast events and, due to the label-free and minimally-invasive nature of smFET technology, the quantification of how the frequency of these events change over long time-scales.

A portion of this work describes smFET fabrication, focusing on improvements to the functionalization method, a critical step to reliably generate individual attachment sites on the CNT for subsequent single-molecule studies. A new synthetic chemistry approach is performed in ultraminiaturized, nanofabricated reaction chambers; using lithographically-defined nanowells, single-point attachments are achieved on hundreds of individual carbon nanotube transistors, providing robust statistics and unprecedented spatial control in adduct positioning. Each device

acts as a sensor to detect, in real-time and through quantized changes in conductance, single-point functionalization of the nanotube, as well as consecutive chemical reactions and subsequent molecular interactions molecular conformational changes.

In particular, this thesis is focused on studying the dynamics of nucleic acids using smFET technology. First, the smFET technique presented is verified by studying the thermodynamics and kinetics of DNA hybridization, the results of which compare favorably both with predicted values and previous smFET studies using alternative device architectures. Next, the reversible folding of a single-stranded telomeric DNA sequence known to form a G-quadruplex structure is studied, revealing the characteristic increased stability of the G-quadruplex structure in the presence of potassium ions relative to sodium ions. Finally, smFET studies of the dynamics of the adenine-sensing *pbuE* riboswitch aptamer found in *Bacillus subtilis* are discussed. These results demonstrate how long-lived, ligand-dependent intermediates form at a base-pair level and suggest that these intermediates have consequences for riboswitch-regulation by adenine binding to the aptamer. With the increased time resolution of smFET technology, this work has achieved the first observation of RNA zipping and unzipping at the single-molecule level, as well as label-free observations of the effects of a three-way junction motif on helix zipping and unzipping.

Table of Contents

List of Figures

List of Tables

Acknowledgements

I would like to begin by acknowledging my immediate family, whose unwavering support and encouragement has been instrumental during my graduate studies. My parents Kevin Daly, Kristine Bird, Alicia Gutierrez Alonso, and Bruce Bird as well as my siblings Derek Daly, Nicole Daly, Rachel Bird, and David Daly have all helped me to get to where I am today. I would like to especially thank my twin sister Nicole Daly, who has always been there for me whenever I needed. My large extended family has also been a source of support for which I am grateful.

There are far too many friends and coworkers for me to acknowledge individually, but I will give particular acknowledgement to Dr. Michelle Ziperstein, Dr. Dat Hoang, Dr. Colin Kinz-Thompson, and Dr. Mark Hendricks for their companionship and advice. In addition I would like to thank Jason Hon, Dr. Bridget Huang, Dr. Delphine Bouilly, Nevette Bailey-Hill, Dr. Kelvin Caban, and Dr. Hasti Amiri for being amazing labmates and mentors throughout my graduate studies. Finally I would like to thank my coworkers in the Shepard lab, Dr. Steven Warren, Scott Trocchia, Dr. Sefi Vernick, and Charishma Puliyanda for the enjoyable and productive collaboration that has made my dissertation possible.

Throughout my education, various teachers and professors have helped shape me into the scientist I am today. I would particularly like to thank my high school teacher Laura Saunders-Layton for first developing my interest in biology, my undergraduate professor Frederick Northrup for guiding me to a career in chemistry, and my undergraduate advisor Prof. Richard Van Duyne for allowing me to develop my analytical laboratory skills and exposing me to the world of museum conservation science. I am extremely thankful of the support, guidance, and mentorship of both of my graduate advisors, Prof. Ruben Gonzalez and Prof. Colin Nuckolls, along with my collaborative advisor Prof. Kenneth Shepard. I am truly grateful to have been able to work with such great advisors and in such an open, collaborative environment.

Chapter 1

Introduction

1.1 Single-Molecule Methods

1.1.1 Single-molecule versus ensemble techniques

Since the first single-molecule measurements were made in the 1970s [1], a variety of single-molecule techniques have been developed to study molecules ranging in size from individual ions [2] to macromolecular machines such as the ribosome [3]. These techniques can augment information available from ensemble or bulk methods, where a large number of molecules are studied simultaneously and a general description of the population is obtained. By observing one molecule at a time, single-molecule techniques can identify rare subpopulations of a group of molecules that would otherwise be averaged out by bulk measurements [4]. This averaging can also affect the ability of ensemble techniques to detect heterogeneity in the dynamics of molecules over time. By performing a large number of measurements, single-molecule methods can utilize statistics to build a description of a population of molecules as a whole while identifying rare states and dynamics that might be invisible to ensemble techniques. Additionally, a significant disadvantage of ensemble techniques is their tendency to miss transient molecular changes due to the unsynchronized dynamics of the entire population [5]. Single-molecule techniques, on the other hand, do not require synchronization of molecular dynamics in order for short-lived intermediates to be detected. While single-molecule methods each pose a variety of technical challenges and limitations [6] as outlined in the following subsections, the valuable information that they can provide has propelled their advancement and increasingly widespread use in the field of biophysics.

1.1.2 Fluorescence techniques

Single-molecule fluorescence approaches have become one of the most popular single-molecule methods for studying the dynamics of biomolecules in part due to the flexibility and variety of fluorescence-based configurations. These approaches typically involve the conjugation of one or more fluorophores to a molecule of interest and then the observation of fluorescence emitted by those fluorophores following excitation with laser light. For instance, fluorescence correlation spectroscopy (FCS), a single-fluorophore method, has been used to measure fluctuations in fluorophore intensity that correlate to diffusion of molecules in and out of a small excitation volume with high temporal resolution [7]. Alternatively, a powerful, multi-fluorophore technique for monitoring single molecules is Fluorescence Resonance Energy Transfer (FRET). This method involves a dipole-dipole interaction between two fluorophores whereby the emission spectrum of one fluorophore, termed the donor, overlaps with the excitation spectrum of the other fluorophore, termed the acceptor. Excitation of the donor fluorophore results in energy transfer to and subsequent light emission from the acceptor fluorophore, the efficiency of which, E_{FRET}, can be described as

$$E_{FRET} = \frac{1}{1 + (R/R_0)^6}$$

where R is the distance between the donor and acceptor fluorophore and R_0 is the fluorophore pair-specific distance which results in $E_{FRET} = 0.5$ [8]. Because the FRET efficiency is dependent on the distance between the two fluorophores, E_{FRET} can be used as a spectroscopic ruler to estimate the relative position of donor and acceptor [9], [10]. FRET has been successfully used to monitor both intermolecular interactions [11] and intramolecular dynamics of biomolecules [12], [13].

Over the past few decades many improvements have been made to existing fluorescence-based methods to alleviate some of the technical challenges they face. The development of statistical reconstruction algorithms such as photoactivated localization microscopy (PALM) [14]

and stochastic optical reconstruction microscopy (STORM) [15] have allowed spatial resolution of molecules to extend beyond the diffraction limit of hundreds of nanometers, and have been implemented to elucidate the motion of molecular motors [16], [17] and to track single molecules *in vivo* [18]. Alternatives to the standard epifluorescence microscopy setup, such as confocal microscopy [19] and total internal reflection fluorescence (TIRF) microscopy [20], as well as advances such as nanofabrication of zero-mode waveguides (ZMWs) [21], reduce the contribution of background fluorescence, thereby allowing higher concentrations of fluorophore-labeled molecules to be used in solution. Additionally, TIRF microscopy and ZMWs can be configured to increase throughput by simultaneously imaging large arrays of fluorophores, while the challenge of missed dynamics due to temporal resolution limitations is being met by improvements in detector and camera technology [22].

Despite these advancements in fluorescence-based single-molecule techniques, tradeoffs between all of these factors still exist. For example, for extremely fast dynamics FCS is preferred over a TIRF microscopy setup, which is limited to 1-10 ms time resolution [6]. While FCS can allow for measurements as fast as 1 ns, this technique suffers significantly from throughput limitations as only one fluorophore can be observed at a time. Additional concerns inherent to fluorescence-based methods, such as perturbations to molecular dynamics from bulky fluorophore labelling and limits to extended observation time caused by fluorophore photobleaching [23], are absent from other single-molecule techniques as outlined below.

1.1.3 Force spectroscopies

Force spectroscopies have been developed for single-molecule measurements and provide a tool for precise position and force measurement and manipulation of biomolecules. Atomic Force Microscopy (AFM), while generally used for topographical imaging by horizontal scanning [24], [25], can be configured to move in the vertical plane and to apply force to a biomolecule tethered between the AFM probe and a surface. AFM has been used to interrogate the strength of covalent bonds [26] as well as protein unfolding [27] and DNA hybridization [28]. While

advances in AFM-based methods have allowed for competitive temporal resolution [29], other configurations such as optical and magnetic tweezers have gained in popularity due to their increased temporal resolution and ability to apply smaller forces on biomolecules than AFM [30]. Optical tweezers rely on focusing laser light through a high numerical aperture microscope objective to create an optical trap that exerts a spring-like restorative force on nearby particles that move away from the focus of the trap [31]. The stiffness of the trap can be controlled by laser intensity and particle size, and detection of asymmetry in the laser spot caused by movement of the particles allows for measurement of both position and force applied on trapped molecules [30]. By tethering biomolecules to polymer beads, either in a configuration with one optical tweezer and bead at one end and the other end surface-immobilized or in a configuration where a biomolecule is tethered at two ends to beads placed in optical traps [30], optical tweezers have been used to study movement of molecular motors [32], [33] and the folding of proteins and nucleic acids [34] and has also achieved sub-nanometer resolution [35]. Magnetic tweezers, conceptually similar to optical tweezers, use magnetic beads to control the position and applied force on tethered biomolecules. Magnetic tweezers are particularly useful for rotational control and applying twisting force to molecules of interest, such as in the study of DNA uncoiling by topoisomerase [36].

As with fluorescence-based techniques, force spectroscopies face tradeoffs between throughput, temporal resolution, and position and force sensitivity. AFM-based techniques generally have better spatial resolution than tweezer techniques, though recent advances in optical tweezer technology has made this method more competitive [35]. Alternatively, tweezer techniques can apply smaller amounts of force to molecules of interest than AFM, including rotational force in the case of magnetic tweezers [30]. Optical tweezers have an advantage over magnetic tweezers in terms of both temporal and spatial resolution, though they cannot be used for extended observation due to photodamage caused by the high-powered lasers used to create the optical traps [6]. A significant advancement in optical tweezer-based methods is the

4

integration of holographic technology, which allows for the creation of an array of optical traps to increase throughput [37]. A particular concern for all force-based techniques is their invasiveness and the effects of applied force on measured molecular dynamics. For example, optical tweezers can induce local heating of biomolecules of interest depending on the wavelength of light used to generate the optical trap [30]. Additionally, it has been discovered that force-based techniques can induce an entropic energy barrier that is responsible for the appearance of two-state hopping phenomena widely observed in force-pulling experiments [38].

1.1.4 Field-Effect Transistors

While both fluorescence and force-based single-molecule techniques have proven to be extremely useful in biophysical studies, the technical limitations of each provide motivation for the development of complementary single-molecule techniques, such as single-molecule field-effect transistor (smFET) technology [39]. As electronic sensors, smFETs create signals through transduction of molecular motion directly to electron current rather than *via* photons and/or trap or probe displacement as is the case with fluorescence and force-based methods [39]. This direct signal transduction is a contributing factor to the increased temporal resolution of smFETs, which are capable of sampling rates in the MHz range without decreases in signal or throughput [40]. As this technique is label-free, and particularly chromophore-free, smFETs exhibit extended stability for single-molecule observation so long as the molecule itself is not labile. The inherent wide-bandwidth of this technique allows for characterization of fast events, as well as quantification of long time-scale dynamic heterogeneity.

As discussed in more detail in Section 1.2.3, structural rearrangements of a charged molecule near the smFET device can lead to measurable fluctuations in current through the smFET conductive channel. While FETs can be fabricated using inorganic materials such as silicon nanowires, the most promising material for smFET applications has been carbon nanotubes (CNTs), the principles and applications of which are discussed in Section 1.2. To

date CNT-based smFETs have been utilized to study the dynamics of both nucleic acids [41]–[43] and proteins [44]–[46] with microsecond temporal resolution.

1.2 Overview of Carbon Nanotubes

Carbon nanotubes (CNTs) are solid-state one-dimensional materials that have found use across many fields due to their favorable mechanical, electronic, and thermal properties [47]. They have been used as atomic force microscopy probe tips [47], stabilizers in polymer composites [48], ion channels and nanopores [49], components in transistors and photovoltaics [50], chemical sensors [51], materials for drug delivery [52], and have even been proposed as cables in the development of a space elevator [53]. The wide application of CNTs is due in part to their relatively low cost of production [47], well-defined and atomically-smooth structure, and ability to change their surface chemistry with relative ease [54].

1.2.1 Properties of carbon nanotubes

Described as sheets of graphene wrapped into cylindrical tubes, CNTs exist in both single-walled (swCNT) and multi-walled (mwCNT) varieties [55]. While graphene itself is a zero bandgap semiconductor, CNTs can exhibit either metallic or semiconducting properties depending on their chirality. CNT chirality is determined by a chiral vector $\mathbf{C}_h$

$$\mathbf{C}_h = n\mathbf{a_1} + m\mathbf{a_2}$$

described by a pair of indices (*n, m*) denoting the number of unit vectors $\mathbf{a_1}$ and $\mathbf{a_2}$ contained in the graphene lattice created by $\mathbf{C}_h$ [56]. Nanotubes with (*n, m*) such that $n = $ m are known as armchair CNTs, while nanotubes with (*n, m*) such that $n = 0$ or $m = 0$ are known as zigzag CNTs and all other nanotubes are known as chiral CNTs. All armchair nanotubes are truly metallic in nature and have zero bandgap, while CNTs with (*n, m*) such that n – $m = 3k$ where k is a nonzero integer have an extremely small bandgap and are considered quasi-metallic (Fig. 1.1)
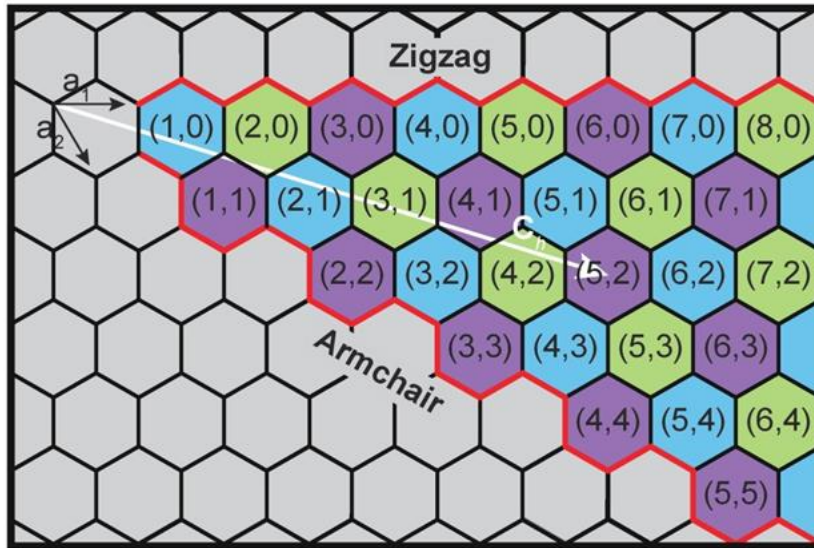
Figure 1.1. Depiction of chiral vector $\mathbf{C}_h$ used to describe a swCNT as a rolled sheet of graphene, where the pair of indices (n, m) indicates the number of unit vectors $\mathbf{a_1}$ and $\mathbf{a_2}$ that compose $\mathbf{C}_h$. All purple hexagons represent metallic or quasi-metallic CNT chiralities, while blue and green hexagons indicate the existence of a band gap in the electronic band structure of the CNT. Figure adapted from Ref. [57].

[57]. All other CNTs are semiconductors with bandgaps that are inversely proportional to their diameter [47]. The diameter d of a CNT can be determined from its (n, m) indices as

$$d = \frac{\sqrt{3}}{\pi} a_{CC} \, (m^2 + mn + n^2)^{1/2}$$

where a_{CC} is the distance between two carbon atoms in the graphene lattice, or 1.421 Å [56]. While diameters are usually between 0.6 and 3.0 nm for swCNTs and 1.4 to more than 100 nm for mwCNTs, CNTs have notably high aspect ratios, with lengths typically ranging from microns to millimeters [47]. Researchers have pushed the limits in both of these dimensions, having produced swCNTs with the smallest theoretically-possible diameter of 0.4 nm [58] as well as ultralong CNTs more than half a meter in length [59]. Because both the diameter and the chirality of a swCNT can greatly affect its mechanical and electronic properties [55], a considerable amount of research has been aimed at either achieving better synthetic control over these nanotube properties [60] or developing post-synthesis CNT sorting methods [57].

1.2.2 Use of carbon nanotubes in electronic devices

Carbon nanotubes have seen use in a wide array of electronic device geometries owing to their tunable properties based on size and chirality. The one-dimensional nature and crystalline structure of CNTs makes them ideal molecular wires which could potentially replace traditional semiconductor materials like silicon [50]. Metallic CNTs have proven to be particularly promising in thin film transistors, where damage to a single CNT does not impede device performance, with potential applications in control of organic light-emitting diodes (OLEDs) [61]. Individual swCNTs, particularly semiconductors, have been used in field-effect transistor architectures due to their sensitivity to local charge environment [62] and ability to create low-power, high-speed electronic switches [63]. CNTFETs have been successfully used to detect enzyme-induced pH changes [64] as well as DNA hybridization [65], though these early applications cannot be considering single-molecule studies. Additionally, the unique optical properties of CNTs have been exploited to create optoelectronic biosensors [66]. For the purpose of integrating CNTs into single-molecule devices, the CNTFET device architecture with single-walled CNTs has proven to be the most effective as described below.

1.2.3 CNTFET theory

As shown in Figure 1.2, the basic components of a CNT-based FET are a conductive channel, in this case a CNT, spanning a metallic source and drain electrode with a third electrode used to gate the system. It is essential to have a barrier between the conductive channel and gate electrode, either a thin insulating oxide layer in the case of a back gate or electrolytic solution in the case of a liquid gate, in order for the gate to properly modulate current flow through the conductive channel [67]. Using gate bias control, the Fermi level of CNTFETs can be tuned – under positive gate bias CNTFETs behave as n-type materials and conduct electrons whereas under negative gate bias CNTFETs behave as p-type materials and conduct holes [63]. This ambipolarity of CNTFETs is particularly useful for logic gate applications [68].
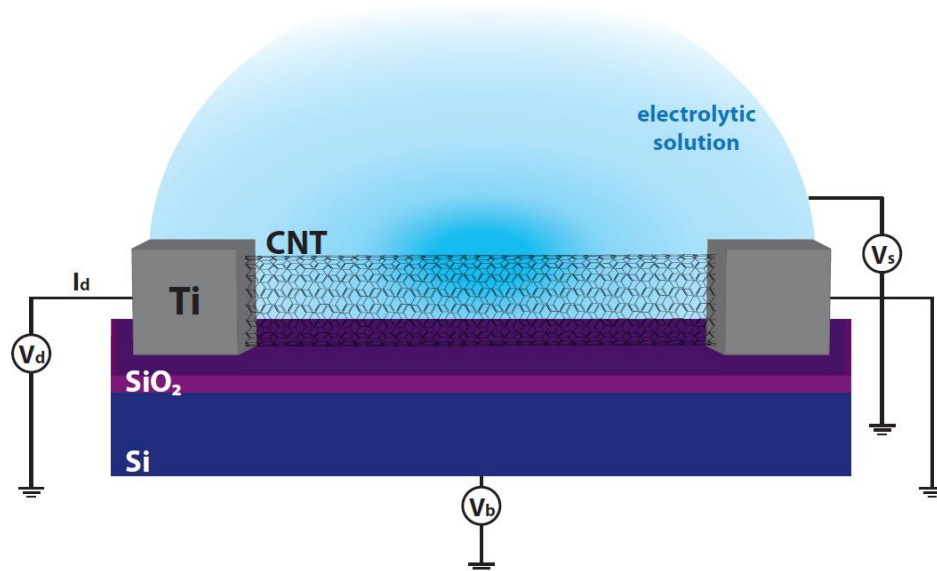
Figure 1.2. Typical CNTFET setup. A bias is placed across the titanium (Ti) source and drain electrodes (V_d) which results in current (I_d) through the CNT conductive channel. A silicon dioxide layer (SiO_2) separates the conductive channel from the back gate through which a bias (V_b) may be applied. In the setup shown an alternative strategy is to gate the CNTFET using a bias (V_s) in an electrolytic solution.

CNTFET device performance is highly dependent on the interaction between the CNT and the metal electrodes. The difference in work function between these two materials, determined primarily by CNT diameter and metal composition, creates an energy barrier known as the Schottky barrier [69].The choice of electrode metal, in addition to creating Schottky barriers at both source and drain, can shift CNTFETs to more unipolar behavior, where either electrons or holes are conducted through the CNT more efficiently [63].

Conductance through swCNTs occurs at the surface, making CNTFETs especially sensitive to their local charge environment. While high sensitivity to charge fluctuations is ideal for sensing single molecules of interest, this sensitivity can contribute to the flicker noise inherent to CNTFETs [70]. For example, conductance fluctuations caused by CNT lattice defects and unpassivated metal electrodes can dominate the CNTFET signal [71]. In order to maximize the signal to noise ratio for CNTFETs in a single-molecule configuration, electrodes can be passivated with polymer resists or metals with native oxide layers like titanium can be used [69]. Additionally, exposure of inherent defects to charge stimuli can be minimized by covering

9

portions of the CNT channel with resist or, alternatively, these defects can be exploited as attachment sites for a single molecule of interest. In an electrolytically-immersed configuration, the magnitude of FET conductance fluctuations caused by a biomolecule is modulated by both the distance between the molecule and the FET [42], [72] as well as the buffer concentration [73]. This relationship is best described using the concept of an electric double layer to describe the interface between a charged solid, in this case the CNTFET, and an electrolytic solution (Fig. 1.3) [74]. In this model, the charge on an electrode induces the formation of a layer of oppositely-charged ions on the electrode surface, known as the Helmholtz layer. Beyond this densely-packed layer is a diffuse layer of oppositely-charged ions, which extends a characteristic distance known as the Debye length. The Debye length, λ_D can be described as
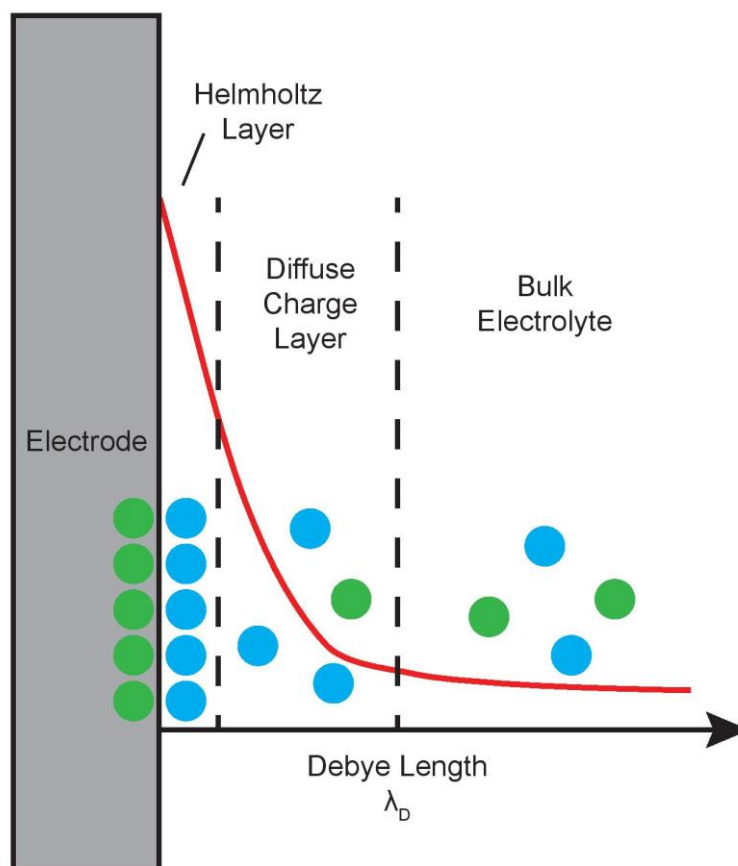
Figure 1.3. Model of the electric double layer between an electrode (CNTFET) and electrolyte (buffer solution). In red electrostatic potential is plotted as a function of distance from the electrode. Charges of opposite sign are shown as green and blue particles.

$$\lambda_D = \sqrt{\frac{\varepsilon k_B T}{2nz^2e^2}}$$

where ε is electrical permittivity of a liquid, k_B is the Boltzmann constant, T is temperature, and n is the concentration of ions with charge z. Beyond this distance electrostatic effects of the charged electrode on the ionic solution are negligible and ion concentrations approach that of the bulk electrolyte. This relationship between the CNTFET and buffer can also be used to explain the sensitivity of the CNTFET; beyond a certain distance from the CNT surface, charges of interest become screened by ions in solution and are no longer detectable. As such temperature, ionic strength and charge are incredibly important tools that can be used to selectively screen or detect charges in the vicinity of a CNTFET. As described in the following section, nucleic acids are ideal candidates for CNTFET sensing due to their high charge density and ability to undergo large-scale structural rearrangements.

1.3 Overview of Nucleic Acids

1.3.1 Structure of nucleic acids

Since the double helix structure of deoxyribonucleic acid (DNA) was famously solved in 1953 [75] and ribonucleic acid (RNA) structures were discovered soon thereafter [76], [77], an astounding number of structural motifs and regulatory roles have been uncovered for both nucleic acids. Beyond the typical Watson-Crick base-pairing interactions that both DNA and RNA use to form double helix structures (Fig. 1.4), each can form more complex structures, such as hairpins and pseudoknots, that utilize non-canonical nucleotide interactions like Hoogsteen and wobble base pairs [78]. As DNA is the form in which most genetic information is stored, many of its higher order structures have a primary goal of compaction and repair, such as supercoiled plasmids in prokaryotes and Holliday junctions in eukaryotic cells [79]. RNAs exist in a variety of forms to suit their many roles, such as single-stranded messenger RNAs
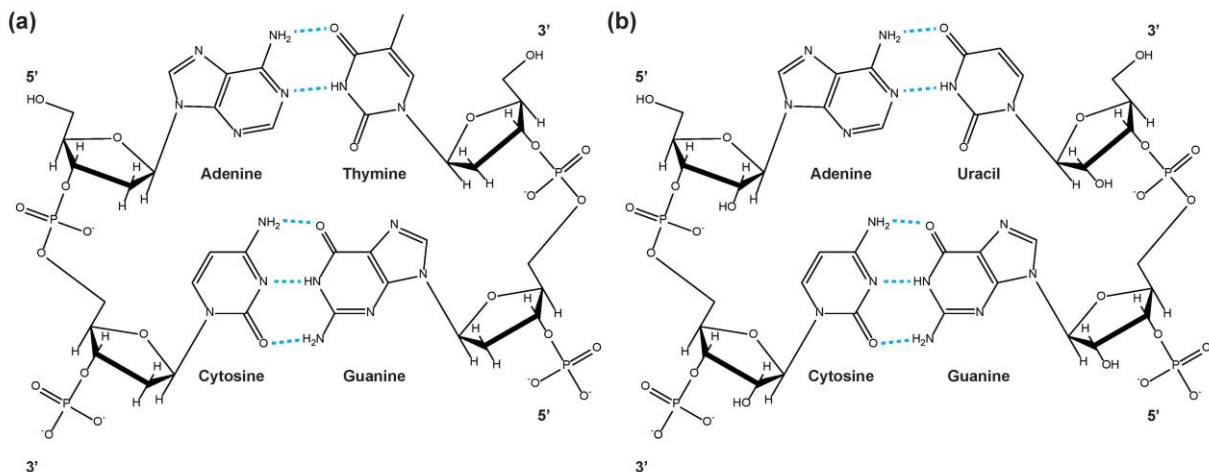
Figure 1.4. Base pairing in (a) DNA and (b) RNA. In each case the phosphate-sugar backbones run anti-parallel (5' to 3' and 3' to 5'). Hydrogen bonds are shown in blue to denote A-T/U and G-C base pairs. An additional difference to note is the presence of a 2' hydroxyl on the sugar of each nucleoside in RNA. The primary helical form of DNA is Z-form and that for RNA is A-form [78].

(mRNAs), folded transfer RNAs (tRNAs), and complexed with proteins to form molecular machines such as in the case of ribosomal RNA (rRNA) [80]. The formation of these structures is generally guided by the hydrophobic nature of nucleotides compared to the charged phosphate-sugar backbone, as well as by the stability imparted to base pairing by both the formation of hydrogen bonds between bases as well as π-orbital interactions between stacked nucleotides [81]. Depending on the role of the nucleic acid sequence, many of the structures formed exist as transient or metastable states and undergo dynamic fluctuations with regulatory consequences as outlined below.

1.3.2 Nucleic acid dynamics

While it is convenient to think of DNA and RNA as static structures, in solution they adopt an ensemble of conformations that can interconvert. The dynamics of these structural rearrangements can vary in complexity and in duration between picoseconds and hundreds of seconds. As depicted in the energy landscape of Figure 1.5, many of these conformations are concerted rather than isolated, forming a hierarchical structure whereby within a globally-altered configuration, smaller-scale rearrangements can take place [82]. These dynamics can include

12
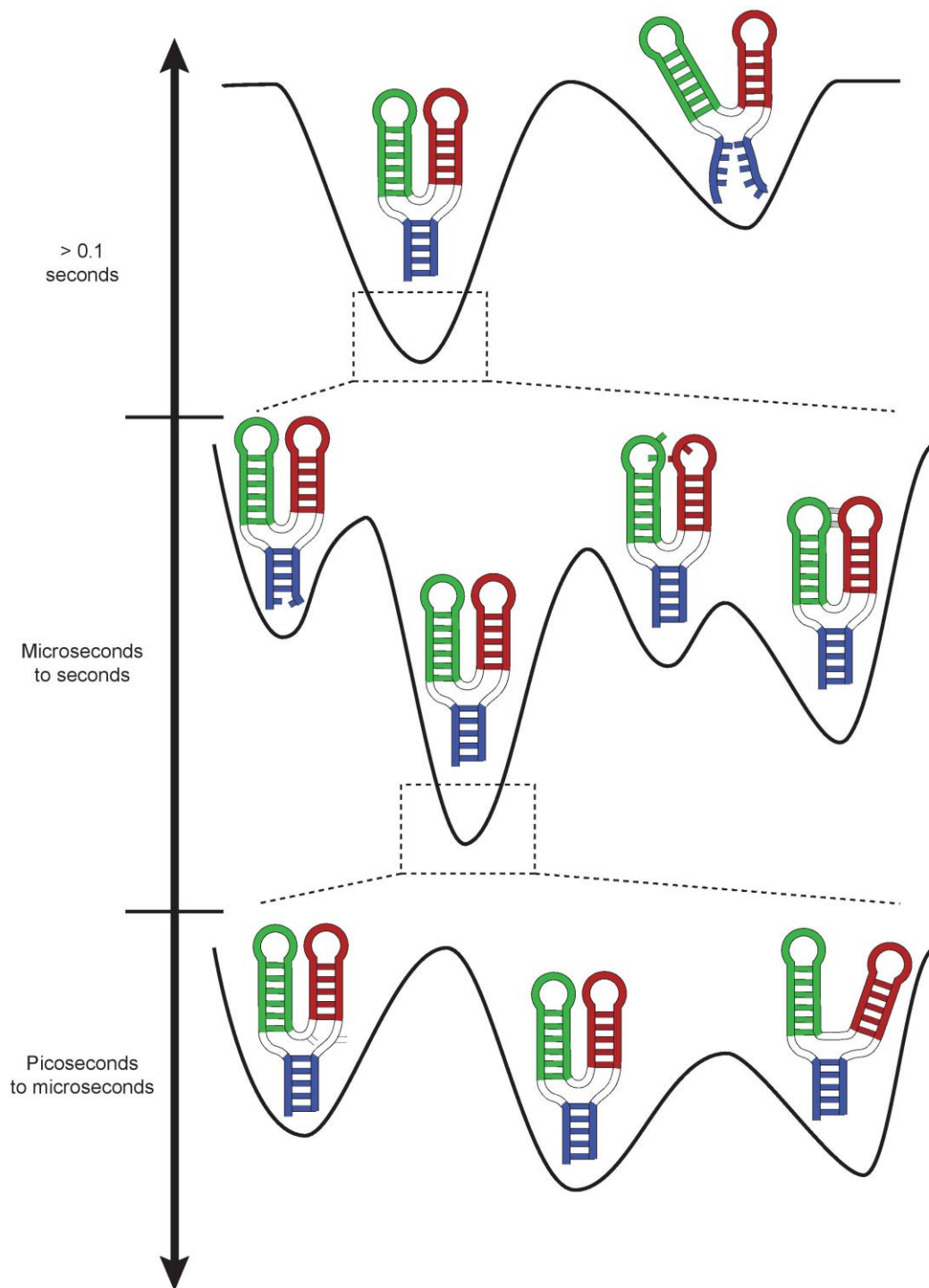
Figure 1.5. Free energy landscape showing the hierarchical nature of nucleic acid structural rearrangements, ranging from picosecond to second-long dynamics. The top level includes secondary structure rearrangements, such as dehybridization of a paired region. Within each energy minimum of the top level is an ensemble of states that include single base-pair melting (left), as well as tertiary pairing (right). The fastest dynamics, shown in the bottom level, include jittering dynamics of loop regions and junction regions.

large changes such as hybridization of two single-stranded DNAs to form a DNA duplex, but can include subtler, faster dynamics such as zipping and unzipping a single base pair at a time and, to a further extreme, minor motions of unpaired nucleotides known as jittering dynamics. Importantly, the energy landscape encompassing these hierarchical dynamics can be altered by cellular cues, such as a change in pH, temperature, ion strength, or protein or ligand concentration [83]. It is this sensitivity coupled to highly-organized, dynamic structural rearrangements that allow nucleic acids to adopt regulatory roles in genetic expression.

1.3.3 Regulatory function of nucleic acids

For many years after their discovery and even after their basic structures were initially solved, both DNA and mRNA were assumed to simply encode and transfer genetic information to ribosomes for translation into proteins. It has become apparent over the past few decades that DNA, and even more so RNA, play regulatory roles in gene expression. For example, while the initial discovery of the DNA structure known as a G-quadruplex occurred *in vitro* [84] and for years this structure was used primarily in applications in materials science [85], more recently DNA G-quadruplexes have been implicated in biological mechanisms underlying cell aging and the proliferation of cancer cells, in that their formation is known to inhibit the replication of chromosomal telomeres [86], [87].

In the case of RNA it has been hypothesized that some of these control elements, such as the class of RNAs known as riboswitches, may be remnants from a time before proteins existed to perform regulatory roles [88]. Riboswitches are genetic control elements located within 5' untranslated region (UTRs) of messenger RNAs (mRNAs) that undergo metabolite-dependent structural rearrangements so as to regulate mRNA transcription, splicing, translation, or stability [89], [90]. While they occur in all domains of life, riboswitches have been proposed as antibiotic drug targets due to their prevalence in bacteria [91]. Because of their relative simplicity and selectivity, riboswitch motifs have also been utilized in the field of genetic engineering [92], [93]. Additional RNAs that perform important regulatory functions in cells include microRNAs and

small interfering RNAs (siRNAs), which are responsible for gene silencing in animals and plants [94]. In order to better understand how both DNA and RNA are involved in genetic control, as well as to better inform bioengineering and drug development to exploit this control, it is imperative to understand how these nucleic acids sense environmental cues and undergo structural rearrangements over a broad range of timescales.

1.4 Dissertation Overview

The purpose of this thesis work is to further development of a relatively new, but promising single-molecule biophysical technique that may provide complementary insight into biomolecular dynamics. Chapter 2 of this work describes the general process of generating CNT-based FETs with a focus on CNT functionalization. While the reactivity of CNTs makes them amenable to a variety of chemistries, obtaining control over CNT reactivity in order to reproducibly generate single attachment sites for single-molecule studies has remained a challenge in the smFET field. Using lithographic techniques, we were able to confine covalent reaction chemistry to nanowells and prevent overfunctionalization of our devices. Additionally, this chemistry generates attachment sites that allow for longer single-molecule observation than those created by noncovalent adsorption of functional groups to CNTs.

The charge sensitivity of CNT-based field-effect transistors makes highly-charged molecules like nucleic acids ideal for smFET studies. Additionally, the breadth of timescales over which DNA and RNA dynamics occur make a wide bandwidth technique necessary to fully characterize fast dynamics as well as their heterogeneity over longer time periods. As such, in Chapter 3 we study DNA hybridization dynamics as well as structural rearrangements and cation sensitivity of G-quadruplex DNA. These dynamics occur on the millisecond to second timescale whereas those investigated in Chapter 4, namely smFET studies of the adenine-sensing *pbuE* riboswitch aptamer, span from hundreds of microseconds to seconds-long.

Additionally, Chapter 4 addresses heterogeneity observed in these RNA dynamics and proposes a hierarchically-organized model of aptamer structural rearrangements in response to adenine sensitivity. Finally Chapter 5 briefly concludes with an outlook on the future of smFET technology.

Chapter 2

Generating Single-Molecule Field-Effect Transistors

2.1 Methods

2.1.1 Carbon nanotube preparation

Since the first observation of carbon nanotubes a quarter of a century ago [95], CNT generation techniques have expanded to include both physical processes such as arc discharge [95] and laser ablation [96], as well as gas-phase chemical processes such as high-pressure catalytic growth from carbon monoxide (HiPco) [97] and chemical vapor deposition (CVD) using hydrocarbons [98]–[100]. While both the arc discharge and laser ablation methods tend to make nanotubes with fewer defects, gas-phase methods generate much higher CNT yields and do not require post-synthesis separation of CNTs from by-products such as amorphous carbon or fullerenes [101]. Additionally, CVD methods are capable of growing CNTs orders of magnitude longer than other methods and allow for nanotube growth *in situ*. This feature has allowed for control of orientation [98] and position [100] of grown CNTs. While the exact mechanism of CNT growth using CVD is still being investigated, the process generally involves the formation of molten metallic nanoparticles on a substrate at extremely high temperatures and flowing gas-phase hydrocarbons or alcohols over the substrate [102]. The nanoparticles absorb the hydrocarbons and begin to extrude a crystalline CNT at the edges of the nanoparticles once a saturation point has been reached [103]. The choice of substrate, nanoparticle composition, and hydrocarbon can all affect the CVD growth mechanism and rate, as well as quality of CNTs produced [104].
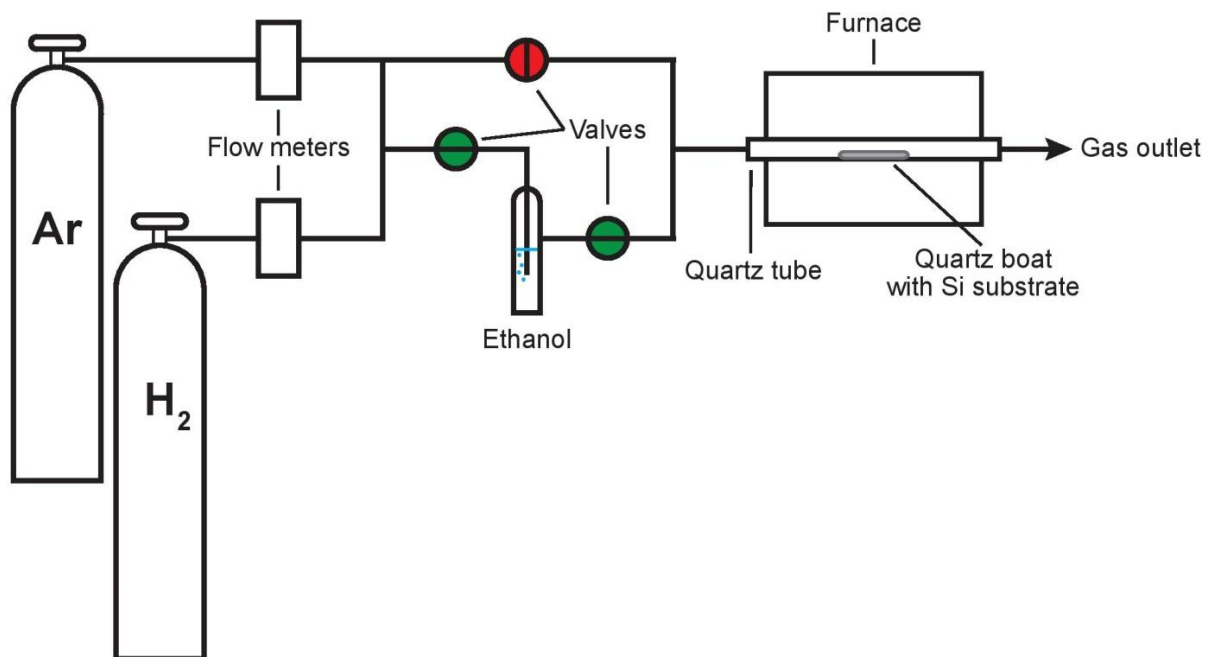
Figure 2.1. Home-built CVD setup. Argon (Ar) and hydrogen (H₂) gas flow rates are controlled by flow meters. Valves are switched to bubble gases through ice-cold ethanol, which acts as the carbon source for growth. Silicon substrates are placed on a quartz boat inside a quartz tube in a furnace. Gas flow promotes directional growth of CNTs.

To generate devices, carbon nanotubes were grown via ferritin-based chemical vapor deposition using a home-built CVD furnace setup (Fig. 2.1). Ferritin is an iron-storage protein that can contain a controlled number of iron atoms in its core. This allows for the creation of iron nanoparticles with a narrow size distribution, which in turn can be used as CVD catalysts to create CNTs with a narrow diameter distribution [105]. A 1:200 aqueous dilution of 10 mg/mL ferritin cationized from horse spleen in 0.15 M NaCl (Sigma Aldrich) was deposited onto the edge of on 1x1 cm^2 silicon substrates (diced from a wafer of 525 µm degenerately-doped silicon covered with 285 nm thermally-grown oxide). Prior to use, substrates were sonicated in acetone for 15 minutes to remove a protective layer of poly(methyl methacrylate) (PMMA) from their surface, followed by 15 minute sonication in isopropyl alcohol and drying with nitrogen gas. Substrates were positioned on a quartz boat such that the edge with ferritin was facing the gas inlet, allowing for the growth of long CNTs in the direction of gas flow. Substrates were annealed

18

under flow of argon/hydrogen gas (80 standard cubic centimeters per minute (sccm) total in a 5:1 ratio) for 20 minutes at 750°C to decompose and remove all organics and to create discrete Fe_2O_3 nanoparticles. The presence of hydrogen gas promotes the reduction of Fe_2O_3 to Fe nanoparticles. Nanotube growth was then initiated by switching valves to bubble the argon/hydrogen gas mixture (now 50 sccm total in a 9:2 ratio) through ice-cold ethanol, the CVD carbon source for which our setup is optimized, and over the annealed iron catalyst for 1 hour at 890°C. After switching valves to stop exposure to ethanol, the setup was allowed to cool to room temperature before substrates were removed.

2.1.2 Carbon nanotube characterization

The CVD method described above can be used to create oriented, straight CNTs up to 1 cm long and with a diameter distribution centered around 1.5 nm [105]. Scanning Electron Microscope (SEM) images were collected using a Hitachi S-4700 FE-SEM with 0.8 kV acceleration voltage and a 5 mm focal distance. Under these conditions CNTs generally scatter electrons more efficiently than the underlying Si substrate and therefore can be seen as brighter objects by SEM. As shown in the SEM images in Figure 2.2, CNTs grow densely in the catalyst deposition region and grow parallel to the direction of gas flow across the entire 1x1 cm^2 substrate.

While electron microscopies such as SEM are useful for obtaining images of CNTs, other methods must be used to characterize the intrinsic properties of individual CNTs. For CNTs grown on a substrate the preferred characterization methods are atomic force microscopy (AFM), photoluminescence, and Raman spectroscopy. Using tapping mode AFM the outer diameter of CNTs can be determined; additionally, conductive tip AFM configurations can be used to obtain spatially-resolved information about the electronic properties of CNT-based devices as described elsewhere [41]. In order to make sensitive smFET devices, single-walled CNTs are required. Thus the most crucial aspect of initial CNT characterization is determination of the number of walls in a candidate CNT, which cannot be determined explicitly using AFM.
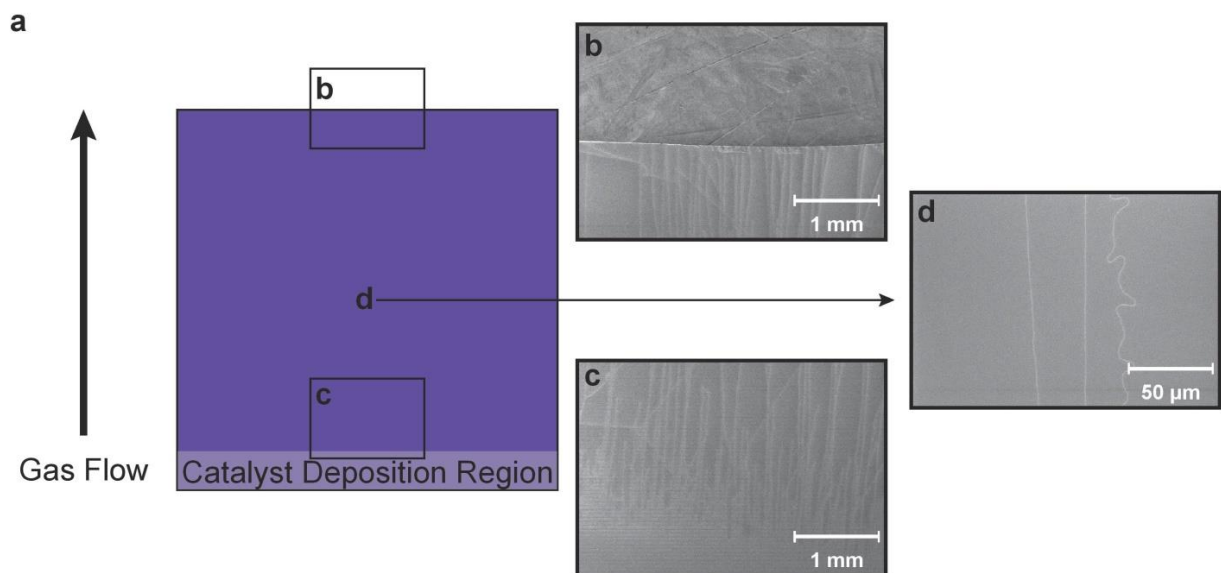
Figure 2.2. SEM characterization of CVD-grown CNTs. (a) scheme of substrate showing direction of gas flow and the catalyst deposition region. (b), (c) 30x magnification SEM images near the catalyst region and at the far edge of the substrate, respectively. (d) 700x magnification SEM image at the center of the substrate showing CNT spacing and straightness.

Both photoluminescence and Raman spectroscopy are sensitive to CNT diameter and chirality, though metallic nanotubes cannot be detected by photoluminescence. As such, we have utilized Raman spectroscopy to reliably characterize individual CNTs by their diameter, wall number, chirality, conductive properties, and degree of intrinsic defectivity [56].

A Raman signal is created by the interaction of incident monochromatic light with phonons or molecular vibrations in a material and subsequent inelastic scattering of light. This signal can be enhanced when the energy of the incident photon is similar in energy to an electronic band gap in a process known as resonant Raman spectroscopy [106]. The relative shift in the wavelength of scattered light provides information about characteristic vibrational modes of individual CNTs, most notably the G-band, the radial breathing mode (RBM), and the disorder-induced D-band [56]. The G-band, a pair of peaks located around 1590 cm^{-1} (G$^+$) and 1570 cm^{-1} (G$^-$), arises from planar vibrations of the carbon atoms in the CNT, similar to the singular G peak found in 2D graphene. While the G$^+$ peak of CNTs generally overlap, the frequency and linewidth of the G$^-$ peak is dependent on both the CNT diameter and its electronic properties. Semiconducting

nanotubes have sharp G⁻ bands that tend to have higher frequencies than the more broad G⁻ bands of metallic nanotubes (Fig. 2.3). The number of G⁻ peaks can be used as an indicator of the number of walls an individual CNT contains, or could suggest the presence of a CNT bundle. Because of the intensity of the G⁺ peak, this Raman-active mode can be used to pinpoint the position of CNTs within 0.1 μm using a 100x microscope objective on a Raman confocal microscopy setup (Renishaw inVia with 532 nm and 633 nm lasers).
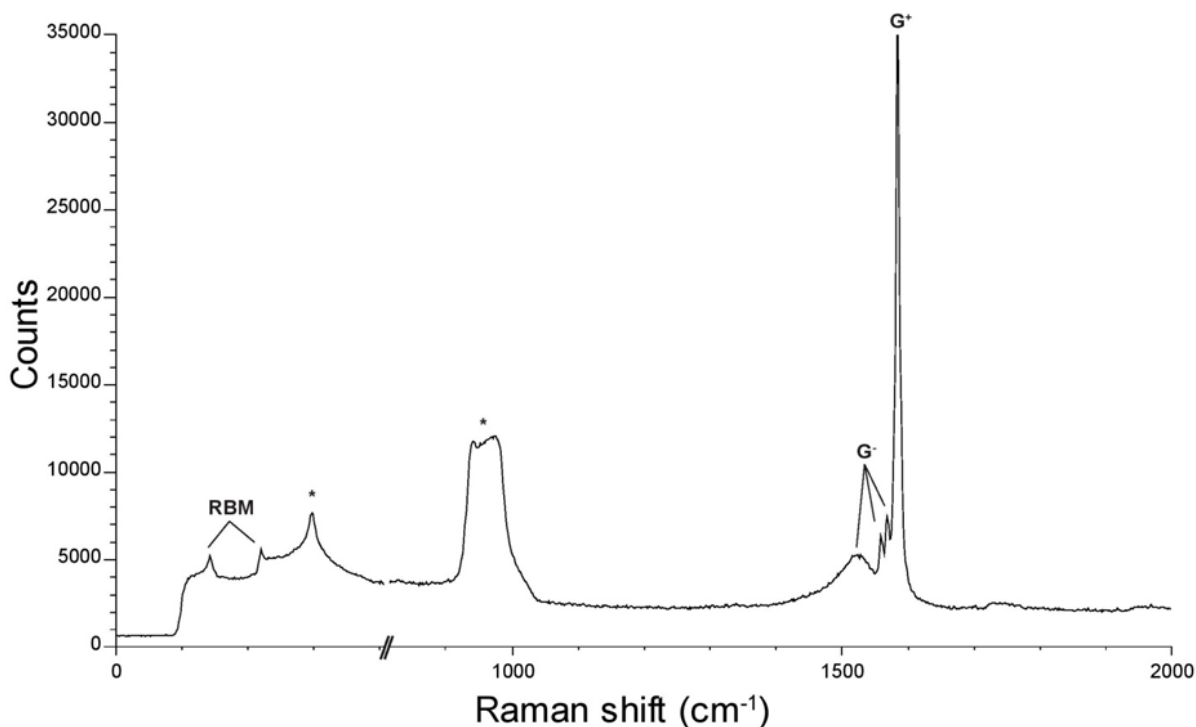
Figure 2.3. Raman spectrum collected using a 100x objective, 1800 l/mm diffraction grating, and 2 mW 532 nm laser light integrated over 30 seconds. Two RBM peaks are observed at 150 and 229 cm⁻¹, the G⁺ peak appears at 1595 cm⁻¹, and three G⁻ peaks are observed – one for a metallic CNT at 1531 cm⁻¹ and two for semiconducting CNTs at 1574 and 1580 cm⁻¹. Peaks marked with * originate from the Si substrate.

The RBM is a Raman-active mode unique to CNTs that arises from coherent vibration of carbon atoms in a CNT wall outward from the center of the nanotube. Typically found between 100 and 500 cm⁻¹, the RBM frequency, ω_{RBM}, is inversely proportional to the diameter d of the CNT and has been experimentally determined to be

$$\omega_{RBM} = 248 \, / \, d \text{ cm}^{-1}$$

for swCNTs and dwCNTs [56]. In the example shown in Figure 2.3, the RBM peaks at 150 and 229 cm^{-1} correspond to a mwCNT with walls of diameter 1.65 and 1.08 nm, respectively. While the frequency of the RBM is not laser wavelength dependent, the intensity of the mode can be enhanced by pairing the laser energy with an electronic excitation energy in the CNT band structure. Because CNT chirality is correlated to both diameter and electronic band gap, a resonant Raman RBM peak can be used to identify the exact chirality of a swCNT [107].

An additional feature of Raman spectra of CNTs is the disorder-induced D-band. This feature, found around 1200 to 1400 cm^{-1}, is thought to be caused by defects in the carbon lattice of graphitic materials [108]. As shown in Figure 2.3, the absence of a D-band indicates low-defect density, and therefore high-quality, CVD growth. Additionally, the progress of chemical reactions that disrupt the carbon lattice of CNT walls can be monitored by the magnitude of this Raman feature (discussed further in Section 2.2.3). Using Raman microscopy to identify CNT G-bands, RBMs, and D-bands allows for identification of CNTs that are single-walled, isolated, and free of defects. Together with SEM, which is primarily used to identify CNTs that appear isolated and span the majority of the centimeter-long substrate, Raman microscopy provides a comprehensive evaluation method of CNT candidates for subsequent device fabrication.

2.1.3 Device fabrication

Two types of devices were used in this dissertation work:

(1) For all real-time electrical measurements (Sections 2.2.1-3 and Chapters 3 and 4), smFET devices are fabricated from previously characterized CNTs grown by CVD on Si substrates. Thirty-two parallel titanium (Ti) electrode pairs (roughly 75 nm in height) with source-drain separation of 4 μm are patterned perpendicular to the direction of nanotube growth using thermal evaporation through a photolithographically-defined mask, after which the substrate is annealed in vacuum at 350 °C. Titanium forms low-resistance electrical contacts with nanotubes [69], as well as a native oxide layer after air exposure that passivates the electrodes. After electrode deposition and CNT characterization, an individual nanotube candidate is chosen to

form the device channels. The portions of the chosen CNT between electrode pairs is protected with PMMA and all other nanotubes are removed using O_2 plasma reactive ion etching (RIE) followed by removal of PMMA using acetone (Fig. 2.4).
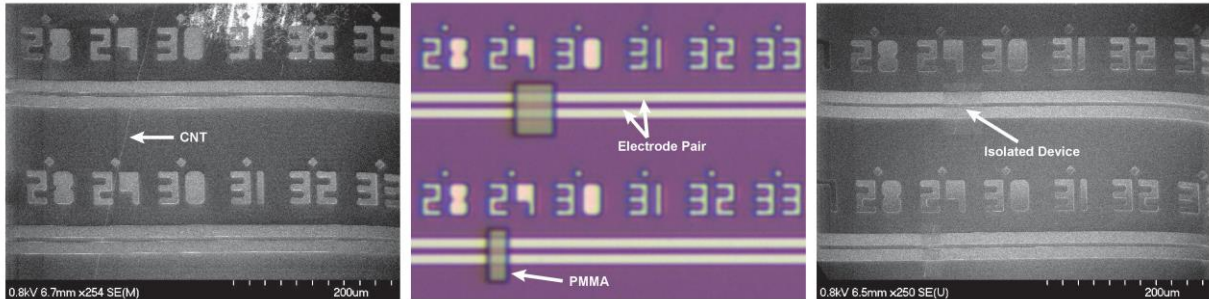
Figure 2.4. Device isolation. Left – a 250x zoom SEM image showing the candidate CNT. Additional nanotube fragments appear white. Center – a 250x optical image showing PMMA deposited over the CNT between electrode pairs. Right – a 250x zoom SEM image of devices post RIE and PMMA removal.

(2) A second geometry with dense arrays of devices is used to develop the nanowell-confined chemistry method that is discussed in Section 2.2.3. Gold (Au) alignment marks are defined after nanotube growth in an 8 mm x 8 mm grid with a pitch of 50 μm. As before, CNT characterization is used to identify and isolate a candidate nanotube using PMMA protection and reactive ion etching. Using electron-beam lithography, a dense array of electrodes can be defined along the nanotube, comprising 20 blocks of 35 electrode pairs separated by 4 μm each (Fig. 2.5). The electrodes are made by evaporating Ti (0.5 nm), palladium (Pd) (20 nm) and Au (50 nm), with Pd ensuring good electrical contacts to the nanotube [69].
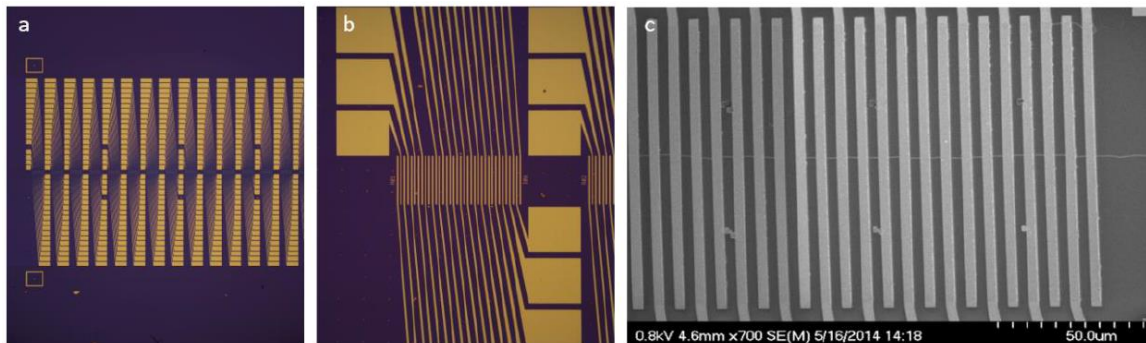
Figure 2.5. Layout for large arrays of carbon nanotube devices. Up to 700 devices are fabricated over a 1 cm long CNT by defining densely-packed arrays of electrodes. (a) Optical image, zoom 2.5x (b) optical image, zoom 20x (c) SEM image, zoom 700x showing a long CNT running perpendicular to electrodes.

23

2.1.4 smFET platform and measurements

Once all CNT characterization and fabrication procedures are complete, the substrate can be placed in a 272-pin ball grid array chip carrier and each electrode can be wirebonded to the carrier with aluminum (Al) wires. A microfluidic flow cell (800 µm wide x 7 mm long) made in polydimethylsiloxane (PDMS) is then stamped over the device array to allow measurement in aqueous conditions (Fig. 2.6). The chip carrier is installed into a custom-printed circuit board that allows for data to be collected at 20,000 Hz using a field-programmable gate array (Opal Kelly XEM6010). Devices are gated using either the substrate back gate (V_G) or electrolytically in saline buffer using on-chip Pt bars as pseudo-reference electrodes (V_L) and their source-drain potential (V_{DS}) is controlled. Real-time device conductance is recorded and processed using custom Python software script. As outlined in the following section, data is then analyzed using a hidden Markov model (HMM) to simultaneously obtain the most probable sequence of device conductance states and to construct baseline-corrected trajectories [41], [109], [110].
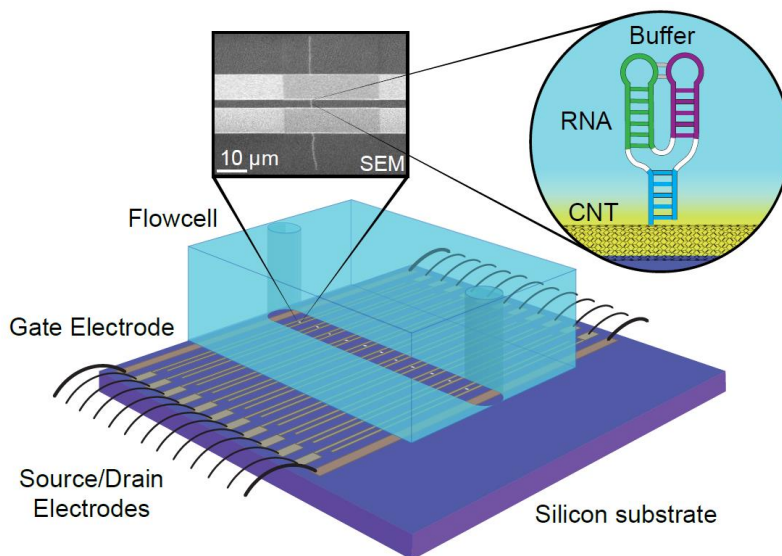
Figure 2.6. smFET experimental setup. Chip design allows for dozens of devices to be generated from a single CNT. All Ti source/drain electrodes and both Pt gate electrodes are positioned under the PDMS microfluidic flow cell for liquid gating and buffer exchange. The inset shows an SEM image (700x zoom) of a single device and a cartoon of an RNA molecule tethered to the CNT surface.

2.1.4 Data manipulation and modeling

Single-molecule FET data, a trajectory of current or conductance fluctuation over time, can be modeled similarly to smFRET data, trajectories of fluorescence intensity or FRET ratio over time. However additional complications to smFET data, namely the well-documented baseline drift in FET device current and the lack of inherent normalization across traces, must be addressed before adapting smFRET data analysis methods for smFET data [70], [109]. As noted by Bruno *et al.*, data from single-molecule devices can be viewed as a Markovian process involving three components: fluctuations that describe the dynamics of the system being studied, baseline drift that can be modelled as a random walk, and noise caused by the device itself [109]. Because the number of states in this hidden Markov model (HMM) is defined, a maximum likelihood (ML) estimation can be used to identify baseline drift and to create a background-subtracted, idealized smFET trace.

The signal caused by the stochastic fluctuations of the biomolecule attached to the smFET, however, is not best modelled using an ML estimation. In the case where the number of states is not known, the ML method suffers from bias towards increasingly complex models. In other words, ML estimation tends to overfit data and converge on a model with too many states [110]. This drawback can be avoided by maximizing marginal likelihood, or evidence, rather than ML. A Bayesian approach can be employed to determine the posterior probability distribution over parameter settings given the observed data, or $p(\boldsymbol{v}|y,K)$, by maximizing evidence, or $p(y|K)$, in the following relationship:

$$p(\boldsymbol{v}|y,K) = \frac{p(y|\boldsymbol{v},K)\,p(\boldsymbol{v}|K)}{p(y|K)}$$

where observed data is y, a chosen model is K, and a vector of parameters is $\boldsymbol{v}$ [110]. It is from the posterior probability distribution that rates between states in a single-molecule data trace can be determined.

2.2   Functionalization of Carbon Nanotubes

Many of the proposed applications of carbon nanotubes rely on manipulation of the structure and solubility of CNTs via functionalization, whether to selectively sort or process CNTs for subsequent device fabrication [57] or to increase the uptake of CNTs for drug delivery [52]. In the case of CNT-based sensors on substrate, functionalization is necessary to render nanotubes amenable to bioconjugation. Various functionalization methods have been developed to either exploit existing defects in the CNT structure [111] or to generate new functional groups both at the ends [112] and along the walls of CNTs [113], [114]. In an effort to create single-molecule devices from CNTs it is necessary to use a functionalization method that is controllable, scalable to the single-molecule level, and can generate a stable functional group for further bioconjugation. Each of the three methods discussed in the following sections have been used to successfully generate smFETs for biophysical studies.

2.2.1   Electrochemical oxidation

One method to functionalize nanotubes involves the electrochemical oxidation of CNT devices using sulfuric acid (H_2SO_4) [114]. The benefit of this method over other covalent functionalization methods is that by controlling the solution potential (V_L), devices can be exposed to oxidative conditions for a controlled time period and their current monitored in real-time. As can be seen in Figure 2.7, exposure of devices to 1.0 M H_2SO_4 does not result in a current drop, indicative of defects created by a chemical reaction, until the solution potential is dropped below a threshold of -1.0 V. After reaching a potential of -1.0 V, once a gate-independent drop in current is observed the solution potential can be brought back to 0 V and the defect can be further oxidized by exposure to 6.5 mM potassium permanganate ($KMnO_4$) to maximize the likelihood of carboxylic acid formation for subsequent attachment chemistry [115]. While device functionalization yields are quite high, the yield of smFET devices successfully used for single-molecule experiments was low, as reported elsewhere [41]. This could
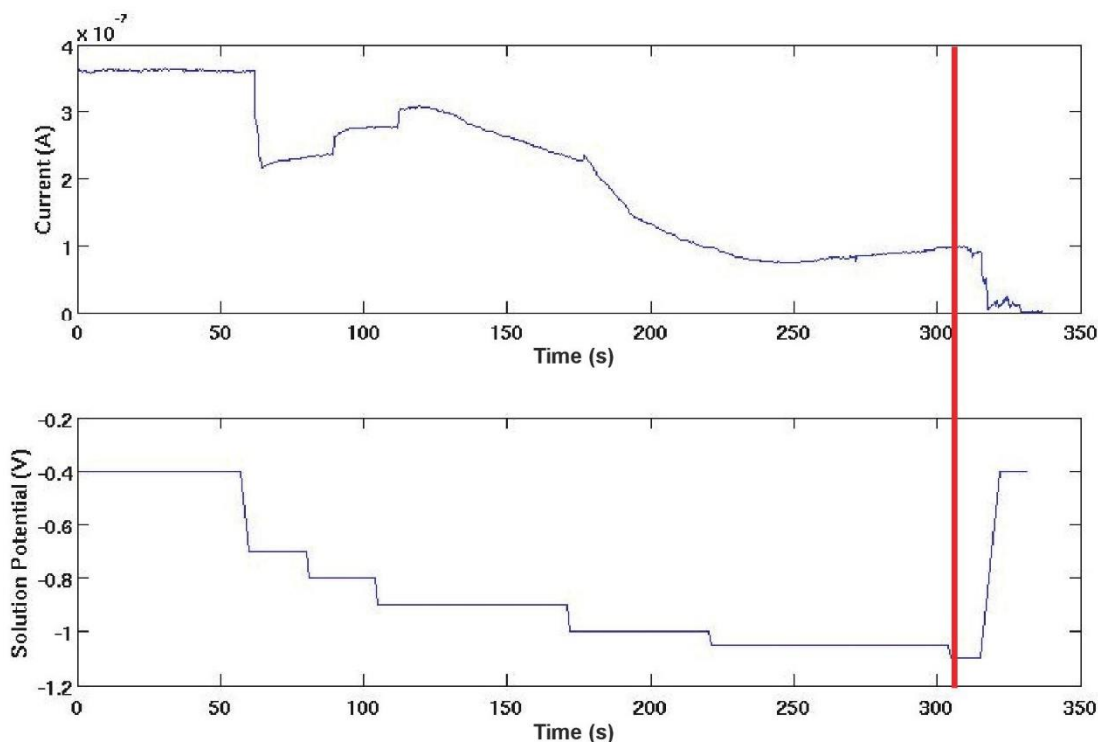
Figure 2.7. Real-time electrochemical oxidation of an smFET. Incremental changes in the solution potential (bottom) result in direct changes in the device current (top). However once a critical potential of – 1.0 V is reached (red line), the device becomes oxidized by the 1.0 M H_2SO_4 and device current drops to about 10% of its original value. The potential is then quickly raised to avoid overoxidation of the CNT.

potentially be due to the generation of functional groups on the CNTs other than carboxylic acids, rendering them inert to subsequent carboxylic acid-amine coupling reactions. Additionally, overoxidation of the CNT can lead to the generation of large holes in the CNT sidewall that create insulating nanotubes incapable of operating as transistors [116].

2.2.2 Noncovalent attachment

Alternative methodology has been developed to functionalize carbon nanotubes without damaging their sidewalls, the most common of which is noncovalent attachment of pyrene-based molecules. Pyrene moieties are known to interact strongly with graphene and CNTs through π-stacking interactions, and are very insoluble in aqueous conditions [113]. Thus, following attachment of pyrene to CNTs in a solvent such as dimethylsulfoxide (DMSO) or dimethylformamide (DMF), smFETs can be exposed to aqueous conditions at room temperature
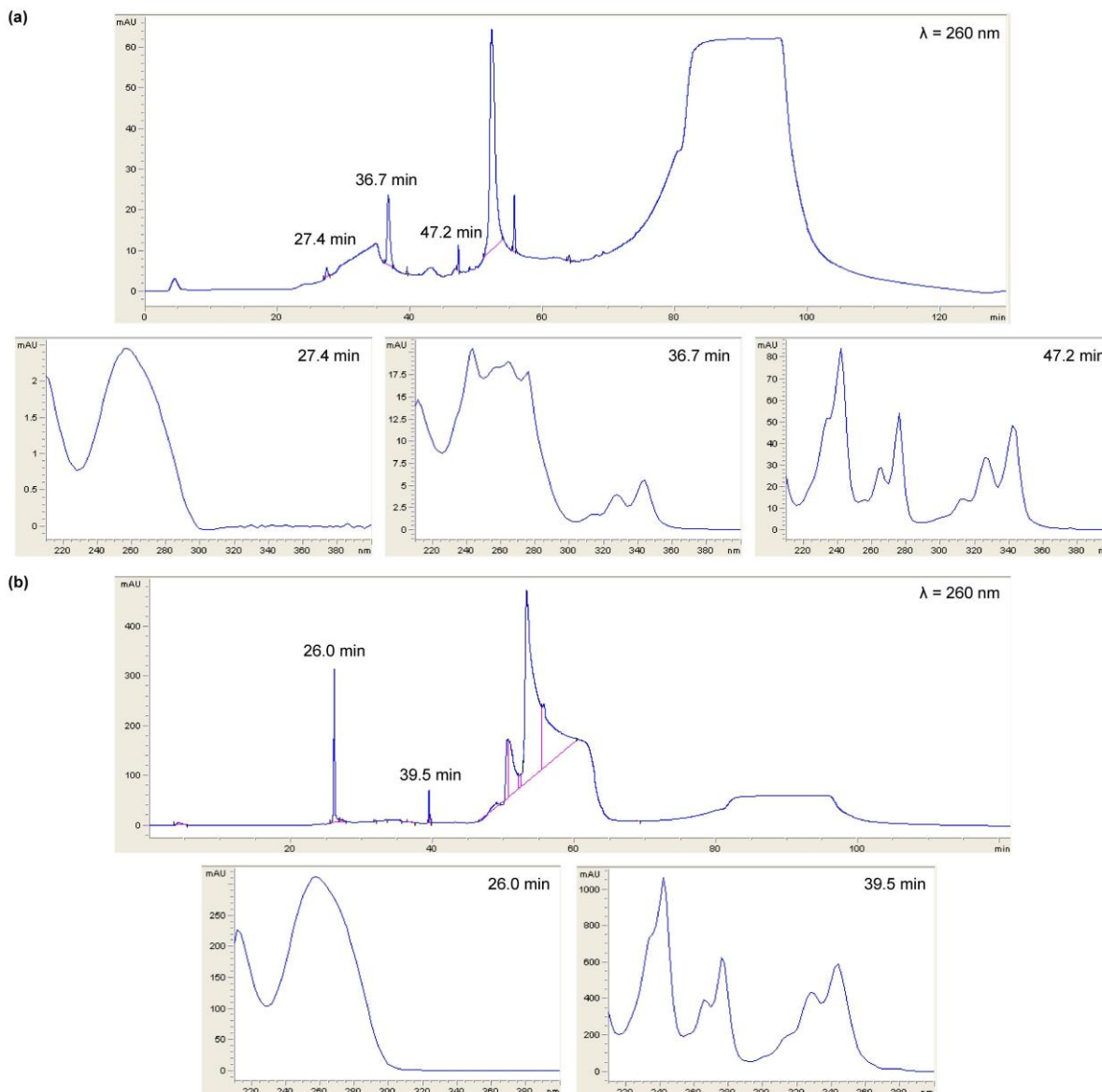
Figure 2.8. Reverse-phase HPLC in 100 mM triethylammonium acetate with a gradient from 5% to 90% acetonitrile. 100 µM amine-terminated DNA was incubated for 30 minutes in 100 mM sodium phosphate buffer (pH 8.4) and 15% DMSO with 20 mM of either (a) 1-pyrenebutyric acid NHS ester or (b) 1-pyrenecarboxylic acid. (a) the peak at 27.4 minutes corresponds to DNA, the peak at 47.2 minutes corresponds to 1-pyrenebutyric acid NHS ester, and the peak at 36.7 corresponds to pyrene-conjugated DNA. (b) the peak at 26.0 minutes corresponds to DNA, the peak at 39.5 minutes corresponds to 1-pyrenecarboxylic acid and no pyrene-conjugated DNA peak is visible. The estimated DNA functionalization yield is 67%.

without pyrene desorbing readily into solution [44]–[46]. For our experiments we opted to use 1-pyrenebutyric acid N-hydroxysuccinimide (NHS) ester (Sigma Aldrich, 95%), which can be subsequently functionalized with primary amine-containing biomolecules [117]. The conditions

for this amide-forming reaction were assessed using reverse-phase high-pressure liquid chromatography (HPLC) to determine the yield of functionalization of an amine-terminated 10 nucleotide single-stranded DNA sequence (see Section 3.1) with 1-pyrenebutyric acid NHS ester (Fig. 2.8). Incubation of the 100 µM DNA with 20 mM 1-pyrenebutyric acid NHS ester in 100 mM sodium phosphate buffer (pH 8.4) and 15% DMSO for 30 minutes resulted in a 67% DNA functionalization yield as calculated by HPLC peak integration (Fig. 2.8a). A control reaction run in parallel using 1-pyrenecarboxylic acid, which cannot readily form a covalent bond to the DNA, showed no pyrene-linked DNA peak by HPLC (Fig. 2.8b).

Using these reaction conditions we further characterized the interaction of pyrene with CNTs using AFM. After initial AFM characterization, isolated CNTs grown on Si substrate as described in Section 2.1.1 were exposed to 100 mM 1-pyrenebutyric acid NHS ester in DMSO for 10 minutes then washed briefly with fresh DMSO. The substrate was then immersed in a solution of 400 nM amine-functionalized gold nanoparticles (AuNP, 10 nm diameter) in 100 mM sodium phosphate buffer (pH 8.4) for 30 minutes and rinsed with fresh buffer before more AFM measurements were performed (Fig. 2.9) . As a control, a separate substrate was incubated in a solution of AuNPs without exposure to 1-pyrenebutyric acid NHS ester (Fig. 2.9c). As shown in
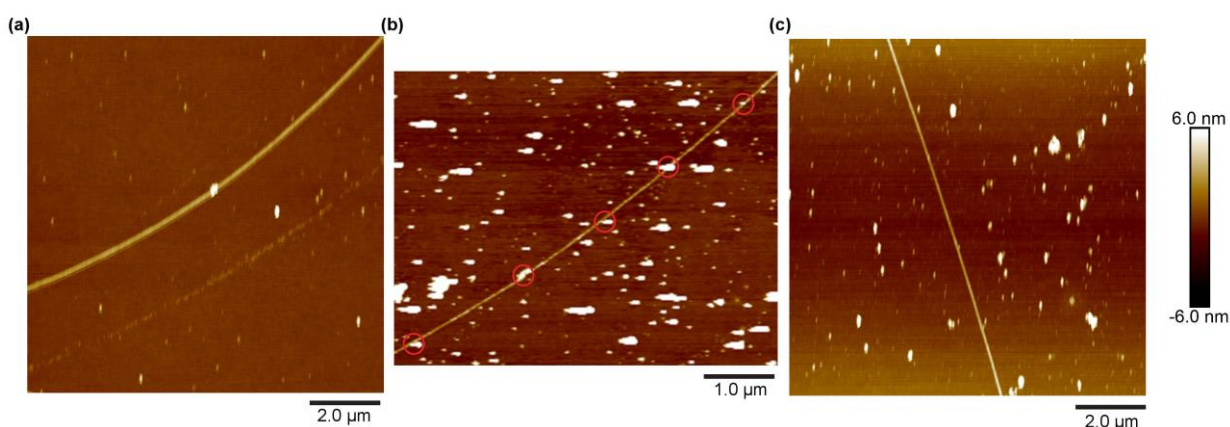
Figure 2.9. AFM characterization of AuNP functionalization of CNTs with pyrene. (a) CNT pre-reaction (b) CNT post incubation with 1-pyrenebutyric acid NHS ester and functionalization with AuNPs. Circled in red are AuNPs adsorbed directly on the underlying CNT. The average spacing between CNT-adsorbed AuNPs is 2 µm. (c) CNT post incubation in a solution of AuNPs shows nonspecific adsorption of AuNPs.

Figure 2.9b, pyrene adsorption and AuNP conjugation resulted in an increase in particles located directly on top of the CNT with an average spacing of 2 μm. As our devices are 4 μm in length, this experiment shows that these conditions should lead on average to the adsorption of one to two pyrene molecules per device.

2.2.3 Covalent reaction chemistry[†]

Typical chemical reactions performed on carbon nanotube surfaces haphazardly distribute over the entire surface of the nanotube [54], [118], [119]. The approach described herein relies on high-yield covalent chemistry and confinement within nanowells patterned in a thin polymer layer to achieve the formation of stable, isolated functional groups at a set of predetermined positions on an array of carbon nanotube devices (Fig. 2.10). Using this method, hundreds of devices can be functionalized in one chemical step, with predictable yields in the number of functional groups as well as unprecedented control over the position of functional sites. After the
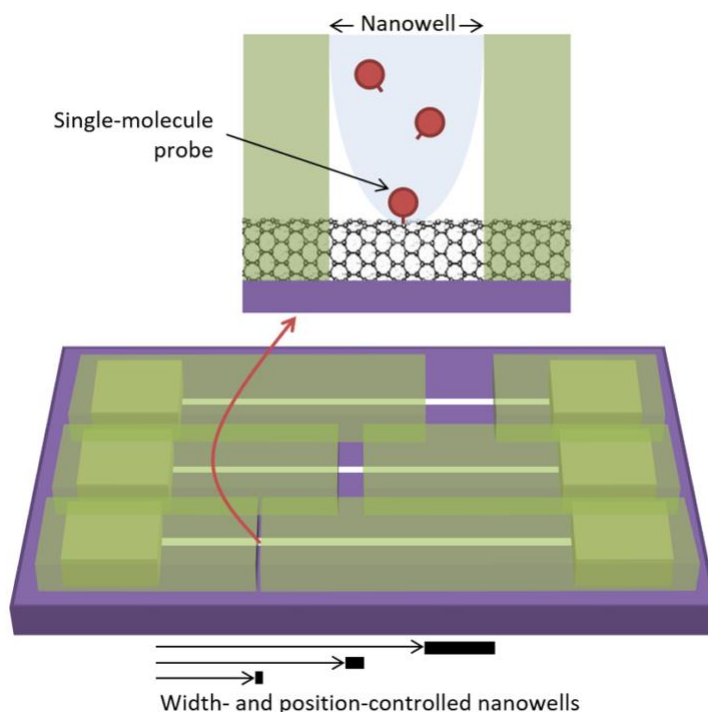
Figure 2.10. Nanowells of controlled width and position are patterned using high-resolution electron-beam lithography in a thin polymer layer covering carbon nanotube devices. The resulting nanowells confine chemical reactions performed within them in order to achieve formation of a single-molecule probe. Figure and caption adapted from Ref. [43].

initial chemical reaction on the nanotube, the polymer mask can be dissolved, and the remaining functional group acts as a single-molecule probe to support a variety of successive, secondary reactions and interactions with single-molecule resolution.

Nanowell-confined chemistry is developed and optimized using carbon nanotube transistors fabricated as described in Section 2.1.3. Nanowells, ranging from 5 nm to the full 4 µm channel length, were patterned in a thin polymer layer (PMMA A2 950k) that is spincoated onto substrates at 5000 rpm for 60 seconds. Writing was done using a high-resolution electron beam lithography writer (NanoBeam nB4). To maximize the resolution, writing was done at low current (1 nA) and patterns were developed in a 4 °C solution of isopropyl alcohol and deionized water (3:1 IPA:H2O). The masks were designed to cover the electrodes and to expose only a portion of the nanotube channel as illustrated in Figure 2.11a. Nanotube segments outside the electrodes were kept fully covered on one side and fully exposed on the other side to act as negative and positive controls, respectively. Figure 2.11b shows AFM images of a 4-µm-long nanotube device covered by a mask with a 20-nm-wide nanowell (middle) and the same
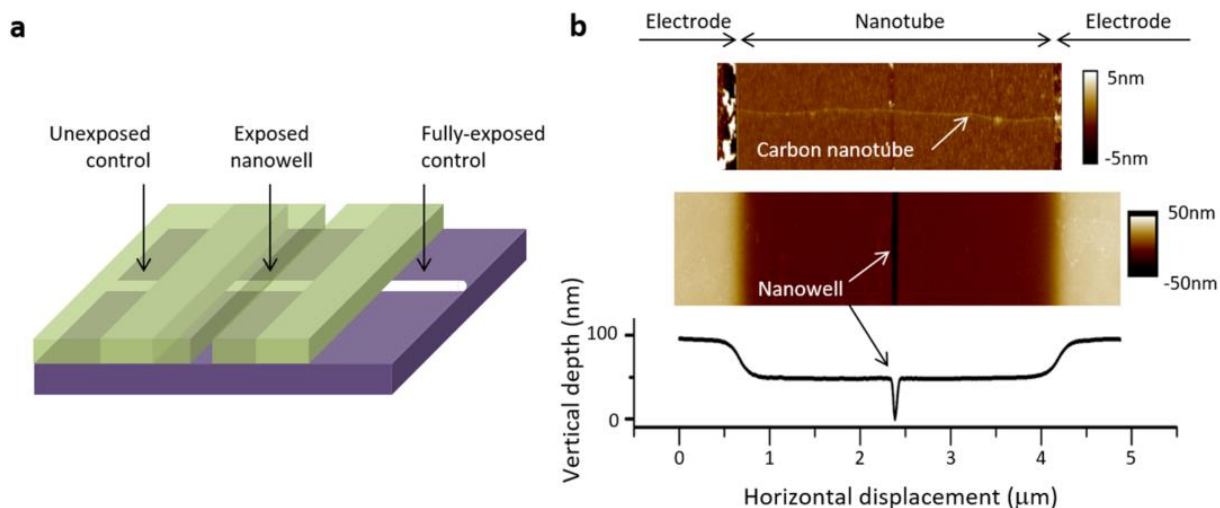
Figure 2.11. Nanowell design and characterization. (a) Mask design showing a nanowell of controlled position and width over the device channel. Positive and negative controls are designed outside the device channel using full exposure and full protection of the nanotube, respectively. (b) AFM image showing a carbon nanotube between metallic electrodes (top) and the same device covered with a protecting mask opened with a 20 nm nanowell (middle), along with the corresponding height profile (bottom). Figure and caption adapted from Ref. [43].

nanotube after removal of the mask (top). The corresponding height profile in Figure 2.11b (bottom) reveals a polymer thickness of approximately 70 nm and confirms the position and width of the nanowell. To confirm full-depth opening of the nanowells down to substrate level, we evaporated an 8-nm-thick layer of titanium over test masks with nanowells of various widths. SEM of the resulting metal lines post mask lift-off (Fig. 2.12) indicates that the smallest wells that can be reliably fabricated are 20 nm wide. After incubation for ~24 h in saline buffer, we observed no significant deterioration in the polymer defining the nanowells (Fig. 2.13).

To install functional groups on the nanotube sidewall, we perform covalent chemistry inside the nanowells formed in the polymer mask. Aryl diazonium chemistry was chosen because it is a reliable, well-characterized reaction [120] that forms stable adducts [121], [122]. This reaction also provides good electronic coupling with the nanotube [123], and attached single-molecule
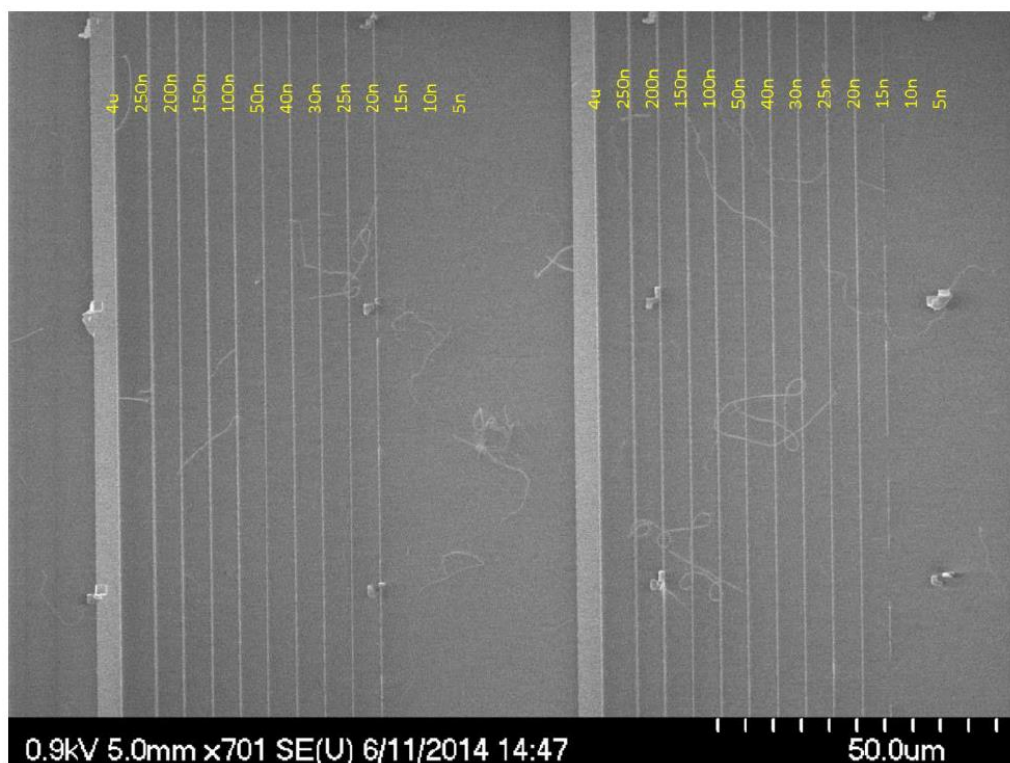
Figure 2.12. SEM characterization of metal patterns produced with PMMA masks. Metal lines (Ti, 8 nm thick) evaporated through masks with different nanowell widths and imaged with SEM. Nanowells down to 20 nm form reproducible, continuous metallic lines indicating development all the way down to the substrate. Figure and caption adapted from Ref. [43].
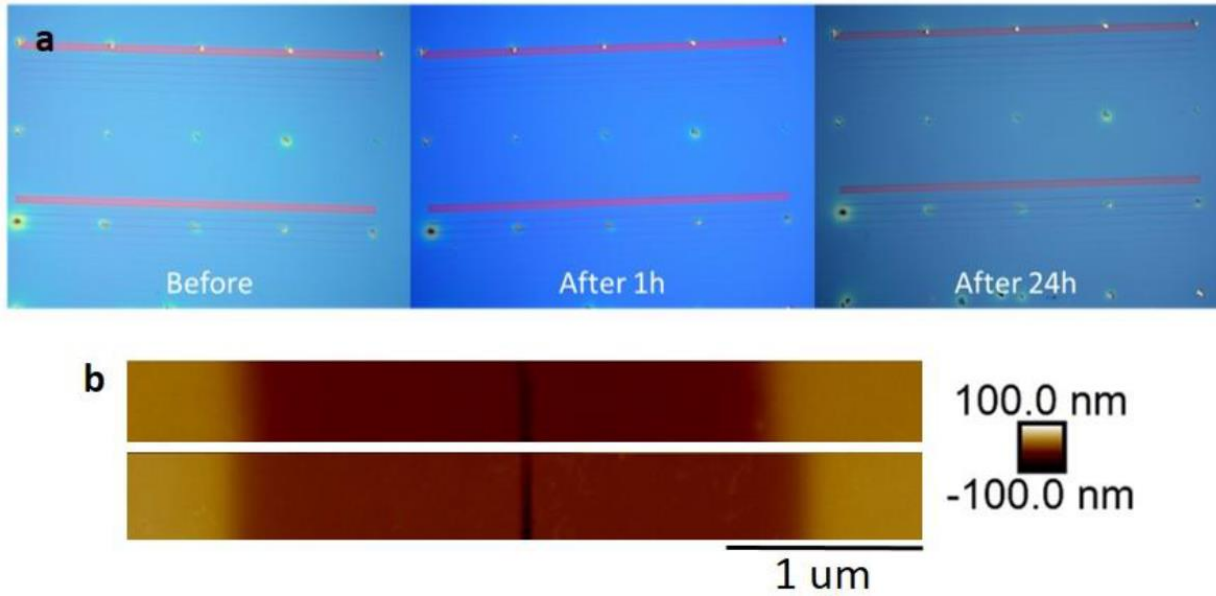
Figure 2.13. Stability of PMMA masks. (a) Optical images before and after immersion for 24 hours in phosphate buffer solution (0.1 M, pH 8) (b) AFM images of a mask before and after reaction in CBDT solution. Figure and caption adapted from Ref. [43].
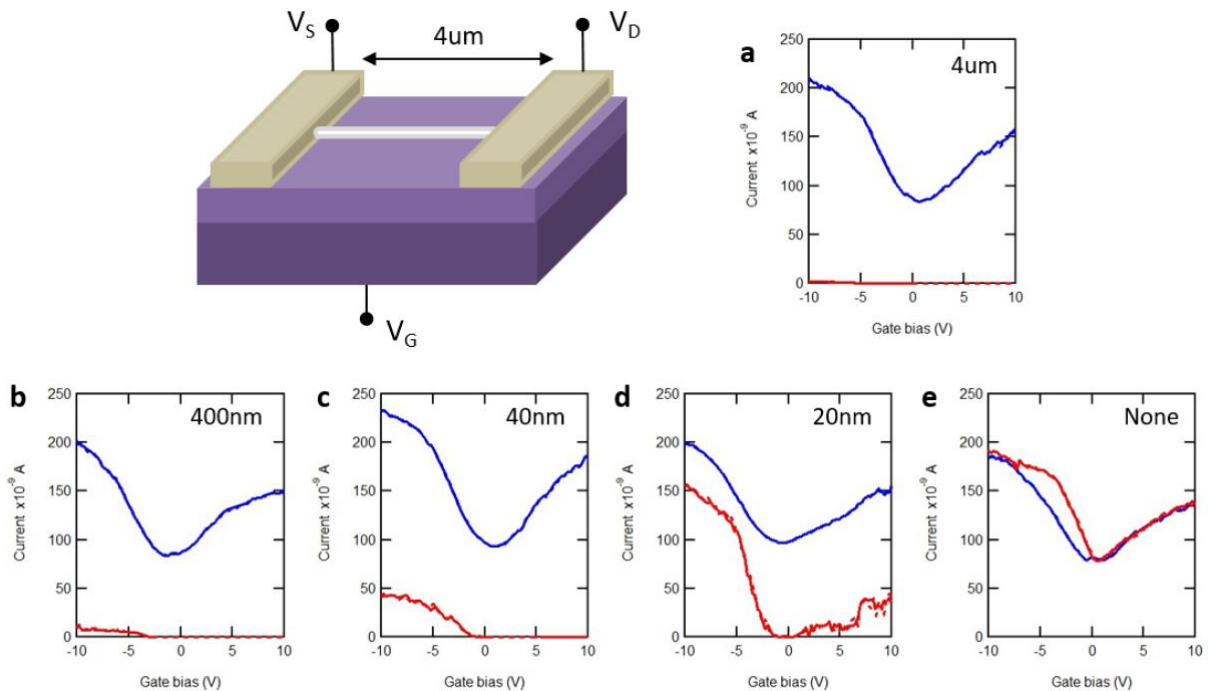
Figure 2.14. Device layout and back-gated current-voltage curves. Device illustration showing source (S), drain (D) and gate (G) electrodes and channel length of 4um. Examples of I-V curves acquired with V_S=50mV, V_D=0mV and sweeping the back-gate potential V_G. Blue is in pristine state and red is after functionalization through a nanowell. Nanowell widths tested are (a) 4um (i.e. no mask), (b) 400nm, (c) 40nm, (d) 20nm, and (e) no exposure (i.e. control). Figure and caption adapted from Ref. [43].

probe groups can be terminated with reactive functional groups, such as a carboxylic acid group, to facilitate subsequent bioconjugation [124]. Carbon nanotubes were functionalized by incubating mask-covered devices for 24 h in a room-temperature 10 mM solution of 4-carboxybenzenediazonium tetrafluoroborate salt (CBDT), synthesized according to McNab et al. [125], in phosphate buffer (100 mM, pH 8). AFM profiles taken before and after functionalization confirm the absence of swelling or other alterations in the mask (Fig. 2.13). After the reaction, the mask was removed by soaking devices in room-temperature acetone, thus making the functional groups available for chemical reactions in organic solvents and with larger, more complex molecules. We studied the statistics of nanowell-confined chemistry by exposing hundreds of devices created from the same, ultra-long nanotube to the CBDT reaction fabricated as described in Section 2.1.3. The width of the nanowells was varied from 20 nm to 4 μm, and some devices were kept fully covered with resist to serve as negative controls. We compared the electrical source-drain conductance before and after functionalization and report the conductance change, defined as

$$G/G_0 = G_{Functionalized}/G_{Initial}$$

, at V_{DS} = 50 mV and V_G = −10V (Fig. 2.14). Figure 2.15a shows histograms of the data for each nanowell width on a typical nanotube, as well as the mean conductance change obtained from a log-normal fit of the distributions [122], [123]. As expected, the fully-exposed devices exhibit a more than an order of magnitude drop in conductance as well as a defect-related D-band in their Raman spectra (Fig. 2.16) [123], [126]–[128].

As the nanowell width is decreased, the conductance change and D-band intensities also decrease (Fig. 2.17). Unexposed control devices do not show any conductance drop or measurable D-band. These observations confirm that functionalization does occur on the nanotube and only inside the nanowell. In the case of the smallest 20-nm-wide nanowell, we observe a small but consistent conductance change when compared to the unexposed controls (Fig. 2.15b), as tested on four different nanotubes. Mean conductance change was calculated
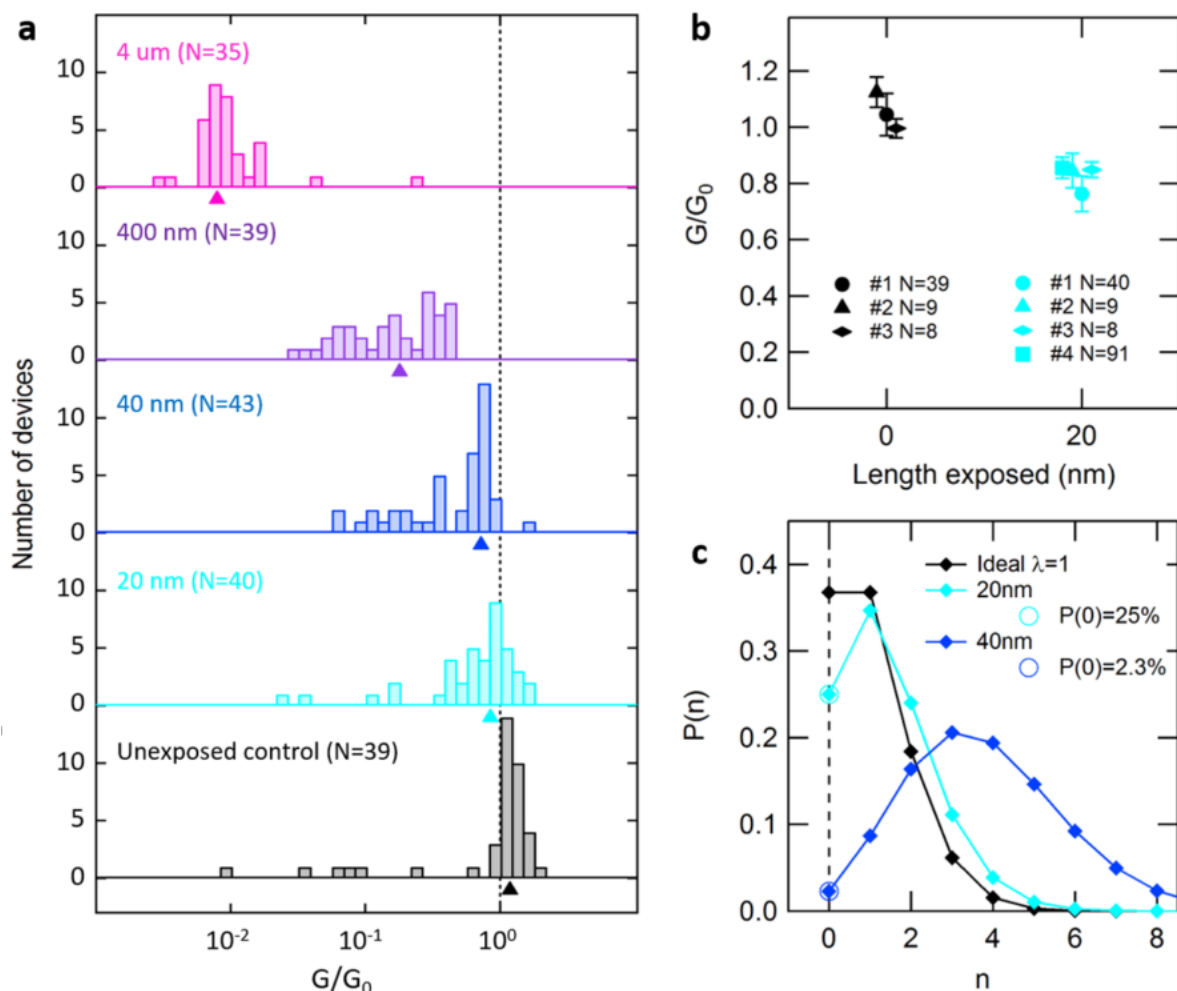
Figure 2.15. Device functionalization through nanowells. (a) Distribution of conductance change G/G_0 after functionalization within nanowells of different widths, compiled on N individual devices from the same nanotube (N_{total} = 196). Arrows indicate the mean conductance change obtained from a log-normal fit of the distribution. (b) Conductance change and error bars obtained using 20 nm nanowell masks (cyan) compared to control devices (black). Each data point is an N-device average from a different nanotube. (c) Modeled probability of getting a number n of functional groups using small nanowells. Circles represent measured points based on data in panel a; others are extrapolated from a Poisson distribution. Figure and caption adapted from Ref. [43].

using 8−91 different devices on each nanotube. In contrast to the exposure through large nanowells, where current drops are highly variable for different nanotubes (Fig. 2.17), reaction in 20-nm-wide nanowells generates a reproducible ~20% average current drop on all tested nanotubes. This difference between large-scale and localized functionalization is likely due to the fact that, in the case of large nanowells, CBDT molecules have a high probability of encountering intrinsic, reactive defects along the nanotube, resulting in inhomogeneous
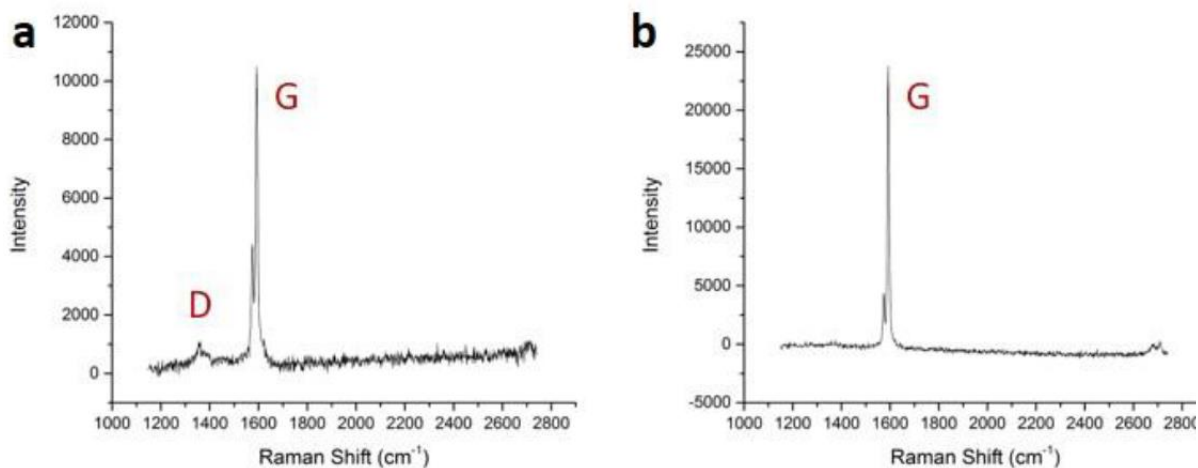
Figure 2.16. Raman spectroscopy of nanowell controls. Raman spectra of fully-exposed (a) and unexposed (b) nanotubes, for positive and negative controls. Exposed nanotubes show a D peak around 1300 cm^{-1} indicating functionalization with CBDT. Figure and caption adapted from Ref. [43].
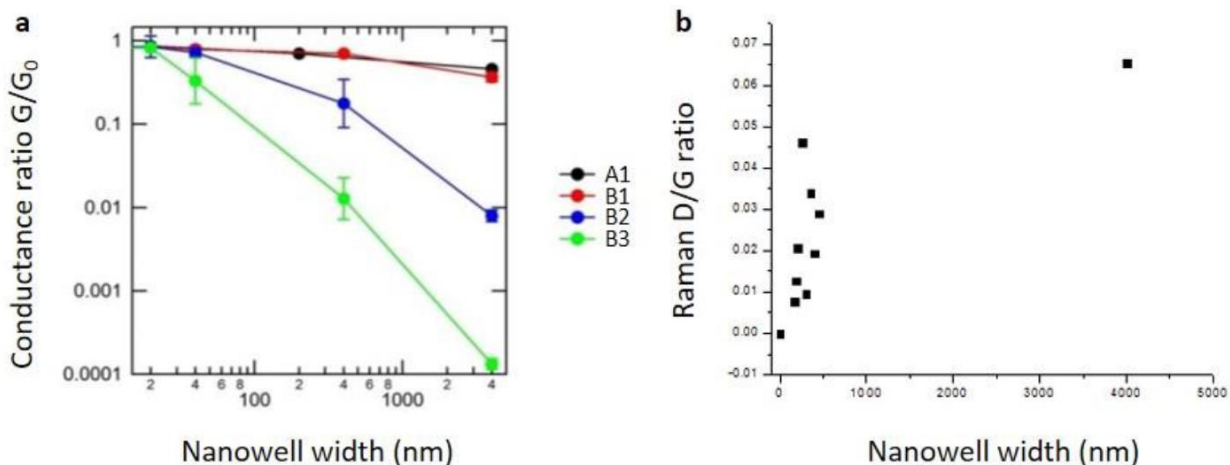
Figure 2.17. Effect of nanowell width. (a) Conductance change G/G_0 after functionalization as a function of nanowell width in several ensembles of devices. Each color represents a set of devices made from a different carbon nanotube, named A1-B1-B2-B3. Each set was divided in subsets in which devices were functionalized using a different nanowell width. Each data point in the figure represents the conductance change averaged over all devices in a subset (between N=5 and N=90) and the error bar represents the standard deviation of that ensemble. (b) Raman D/G ratio, which decreases as nanowell width decreases. Each data point is acquired from a separate device exposed using a different nanowell width. Figure and caption adapted from Ref. [43].

36

reactions, whereas, in the case of 20 nm-wide nanowells, CBDT molecules have a very low probability of encountering such defects.

Consistency in the current drop for small nanowells across different devices and nanotubes suggests that it stems from the creation of a consistent number of functional groups. The actual number of functional groups is extracted from the population of unreacted devices for each nanowell width. We find that the overlap between the G/G_0 distributions of 20 nm nanowell devices and unexposed control devices is about 1 in 4, which is assigned to the population of unreacted devices. Using a Poisson distribution

$$p(n) = \lambda^n e^{-\lambda}/n!$$

to model the probability $p(n)$ to get a number n of individual functional groups, we first estimate $p(0)$ from the fraction of devices with no or positive change in conductance, then extrapolate to find the average number λ of functional groups. For 20 nm nanowells, we find an average of $\lambda = 1.39$ functional groups per device and a population of devices having single-molecule probe attachment of $p(n = 1) = 35\%$, which approaches the $\lambda = 1$ theoretical optimum for single-molecule devices illustrated in Figure 2.15c. In contrast, larger nanowells allow for a wider distribution in the number of functional groups per device, as illustrated by the Poisson distribution calculated for 40 nm nanowells in Figure 2.15c and by the corresponding broadening of histograms in Figure 2.15a. Finally, we note that the ~20% average conductance drop associated with this single-molecule reaction is consistent with recent experimental work on CBDT-induced defects [129] and that this value is significantly less in amplitude than that obtained by oxidative defect-mediated single-point approaches [41], [114], in agreement with hybrid density functional theory (DFT)/non-equilibrium Green's function calculations that predict the oxidative method to generate a greater alteration than a single-point chemical bond [130].

To confirm the presence of a single-molecule functional group and to test the ability of the platform to monitor sequential chemical reactions on this probe, we used an array of ten smFETs functionalized using nanowell-confined chemistry and integrated with a microfluidic

platform (Fig. 2.18a). Of ten devices, seven were exposed through 20-nm-wide nanowells using

CBDT chemistry ("exposed" devices), and three were designed to be controls by fully covering

them with the polymer mask ("unexposed" devices), as summarized in Table 2.1. As before,

Raman spectroscopy was used on positive and negative controls to confirm, respectively, the

reactivity of the nanotube to the diazonium chemistry and the effectiveness of the protective

mask (see Fig. 2.11a). After completing the reaction, five of the exposed devices experienced

an average drop in conductance of ~20%, a signature consistent with that obtained above in the

statistical analysis for the binding of single-molecule probes. The two other exposed devices
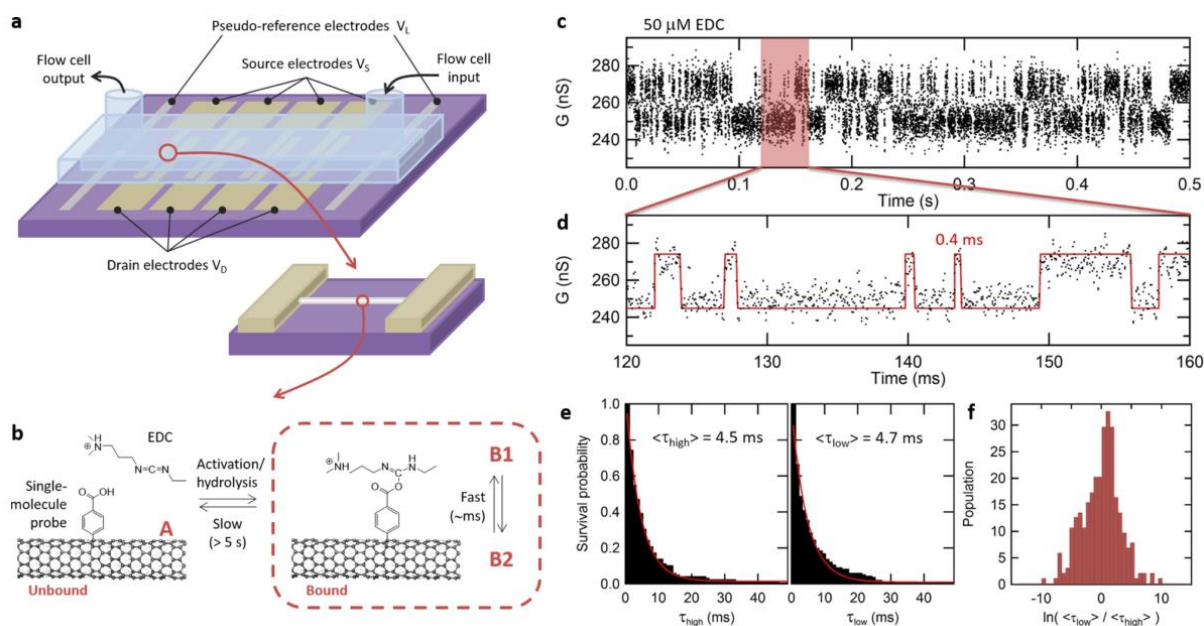
Figure 2.18. Real-time sensitivity to secondary reactions on the primary single-molecule probe. (a) Design of smFET devices, including carbon nanotube channel, drain, and source electrodes, as well as pseudoreference electrodes for electrolytic gating in the microfluidic cell. (b) Reaction kinetics between an EDC molecule and a single-molecule carboxyphenyl probe covalently attached on the nanotube. Two levels of kinetics can be observed: slow transition between the unbound and bound states, corresponding to the reversible activation and hydrolysis reactions on the COOH probe, as well as fast kinetics due to fluctuations within a bound COOH/EDC complex. (c) Real-time response of a device in the presence of 50 µM EDC, after baseline correction, showing an active phase with two-state activity characteristic of rapid fluctuations in a single carboxy-EDC adduct (B1/B2 fluctuations). (d) Zoomed region of the trajectory superimposed with an idealized trace obtained from a hidden Markov model, revealing events resolved in the submillisecond range. (e) Survival probability plot for the high- and low-conductance states, fitted with a single-exponential function to obtain average lifetimes $\langle \tau_{high} \rangle$ and $\langle \tau_{low} \rangle$. (f) Distribution of $\langle \tau_{high} \rangle / \langle \tau_{low} \rangle$ ratios obtained from multiple, successive, 1-s-long segments of a long trajectory, showing kinetics centered on the symmetric case in which $\langle \tau_{high} \rangle = \langle \tau_{low} \rangle$, with a level of heterogeneity in the distribution that is typical of single-molecule experiments. Figure and caption adapted from Ref. [43].

Table 2.1. Summary of device status and activity on the smFET platform.

Device	ID	Type	Conductance drop	Functionalization status	Single-molecule EDC activity
1	A1	Unexposed	No	--	No
2	A3	Exposed	0.75	Functionalized	No
3	A4	Exposed	0.81	Functionalized	No
4	A6	Exposed	0.91	Functionalized	No
5	A8	Exposed	No	Unfunctionalized	No
6	B1	Unexposed	No	--	No
7	B3	Exposed	0.6	Functionalized	Yes
8	B6	Exposed	No	Unfunctionalized	No
9	B8	Exposed	0.82	Functionalized	Yes
10	C1	Unexposed	No	--	No
Yield				5/7 = 71% functionalized 2/7 = 29% unfunctionalized	2/7 = 29% EDC-active
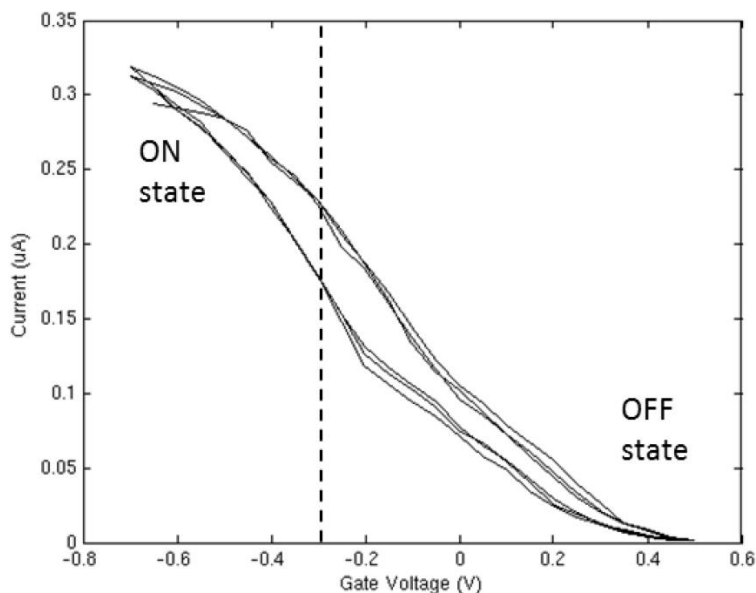
Figure 2.19. Typical transfer curve of an smFET in aqueous conditions. Conductance of the nanotube switches from an ON-state at high negative gate bias to an OFF-state at positive bias. Real-time measurements are performed at -300 mV gate bias to have the nanotube conductance between ON and OFF states. Drain-source potential is fixed at 100 mV and gate potential is applied through Pt pseudoreference electrodes in contact with the electrolytic solution (see Fig. 2.15a). This specific transfer curve is from device B3 (see Table 2.1). Figure and caption adapted from Ref. [43].

show no conductance drop, consistent with remaining not functionalized, as discussed above. These devices are labeled as "functionalized" and "unfunctionalized", respectively (see Table 2.1). Similarly, all unexposed devices preserve their conductance due to the protection provided by the mask. All devices were immersed in aqueous 2-(N-morpholino)-ethanesulfonic acid (MES) buffer solution (100 mM, pH 4.5) in the flow cell, and their drain-source current was measured in real-time using a constant DC applied bias of V_{SD} = 100 mV and an electrolytic gating potential of V_L = −300 mV, chosen to place the electrostatic potential of the nanotubes between their electrical ON and OFF states (Fig. 2.19). Under these conditions, all devices exhibit a baseline current of several hundreds of nA with $1/f$ background noise and no distinguishable activity (Fig. 2.20).

The buffer solution was then switched to a 50 µM solution of 1-ethyl-3-(3-(dimethylamino)propyl)-carbodiimide (EDC) in aqueous MES buffer (100 mM, pH 4.5). EDC is an activating and dehydrating agent that forms an O-acylisourea derivative of a carboxylic acid [124]. These intermediate derivatives hydrolyze quickly in the presence of water with a typical turnover period of 10−100 s in such conditions [114], [131], as illustrated by the slow kinetics between the unbound (A) and bound (B) states in Figure 2.18b. In the presence of EDC, two of the functionalized devices were found to exhibit successive phases of random telegraph noise (RTN) in their conductance, separated by inactive phases as shown in Figure 2.21.

Following Goldsmith et al. [114], we attribute the inactive phases to the unbound, hydrolyzed state (A) and the active phases with RTN to rapid fluctuations (B1/B2) within a single COOH/EDC complex. The period of active or inactive phases was observed to be longer than 5 s (Fig. 2.21), which is consistent with the turnover rate of the activation/hydrolysis reaction [114], [131]. An example trajectory measured in an active phase is shown in Figure 2.18c and d, after baseline correction for clarity (see raw trajectories and baseline fit in Fig. 2.21) [109]. The trajectory shows rapid two-state RTN activity, in which dwell times with submillisecond duration can be resolved (Fig. 2.18d). Using a hidden Markov model, we extract the distribution of dwell
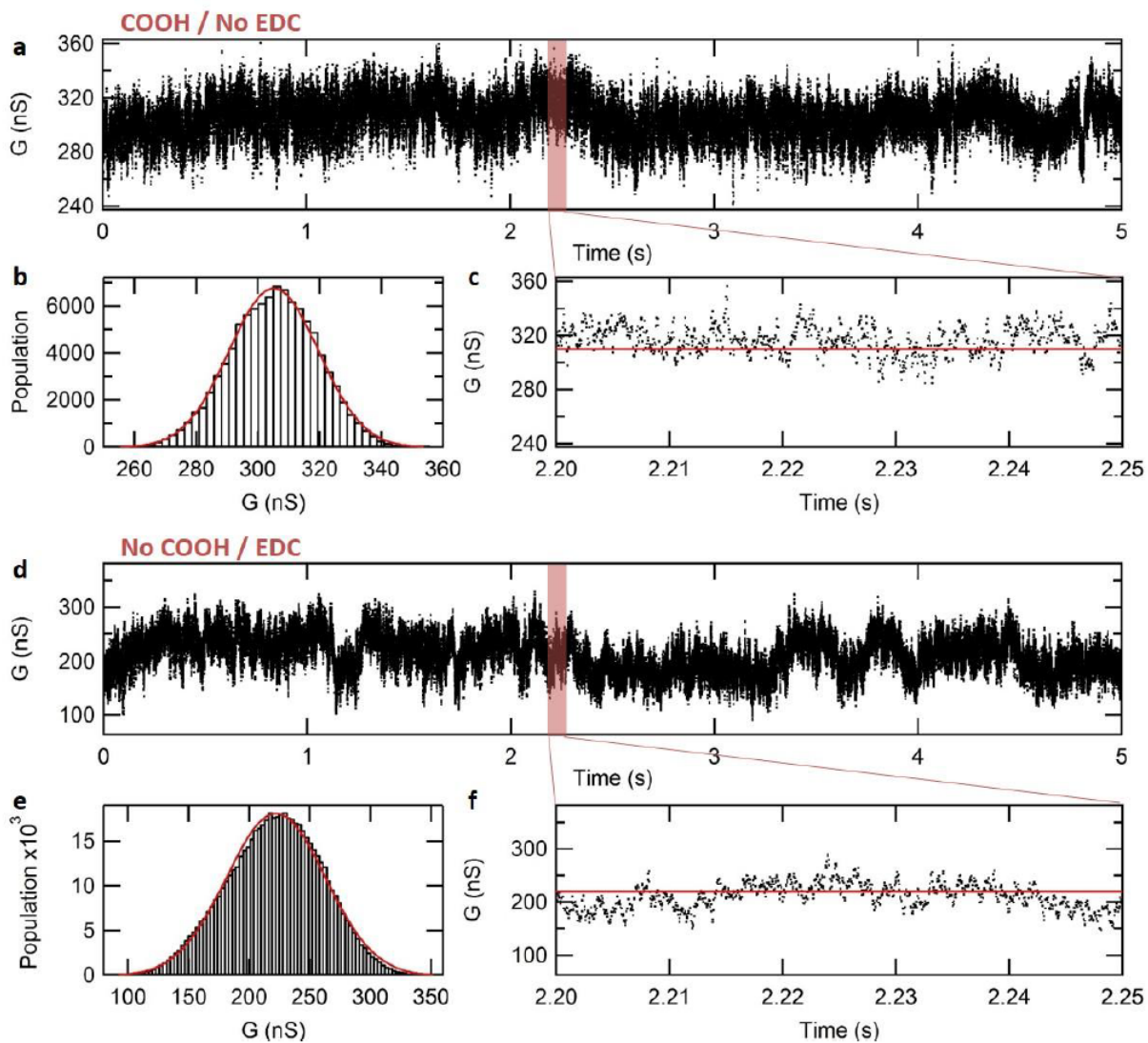
Figure 2.20. Control experiments for EDC activity. (a) Control trace from a functionalized device in absence of EDC. (b) Distribution of conductance values in the above trace, with a single Gaussian fit indicative of single-state dynamics. (c) Zoom on a 50 ms region and idealized trace (red) for single-state dynamics. (d) Control trace from an unexposed device in presence of 50 μM EDC. (e) Distribution of conductance values in the above trace, with a single Gaussian fit indicative of single-state dynamics. (f) Zoom on a 50 ms region and idealized trace (red) for single-state dynamics. Figure and caption adapted from Ref. [43].

times in the high- and low-conductance states and build survival probability plots, presented in

Figure 2.18e. These plots can be fit with a single-exponential function, indicating simple kinetics

with average lifetimes of $\langle \tau_{high} \rangle$ = 4.5 ms and $\langle \tau_{low} \rangle$ = 4.7 ms for the high- and low-conductance

states, respectively. The similarity between the lifetimes of the two states in that trajectory
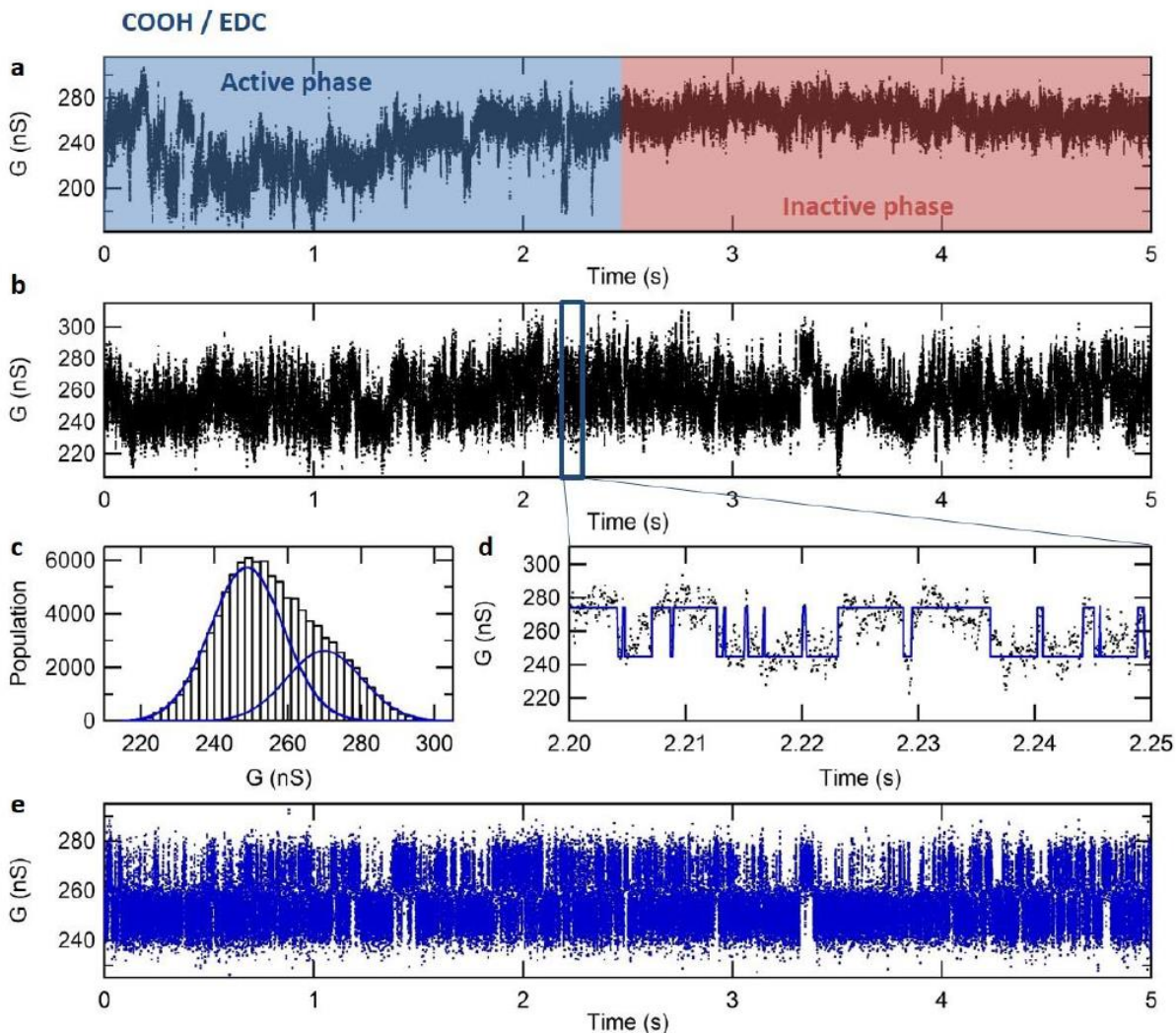
Figure 2.21. Real-time COOH/EDC activity. (a) Example of transition between an active and inactive phase in the COOH/EDC dynamics. Typical lifetime of each phase is > 5 s. (b) Real-time trajectory of a functionalized device in presence of 50 µM EDC. (c) Distribution of conductance values in the above trace, fitted with two Gaussians as indicative of two-state dynamics. (d) Zoom on a 50 ms segment, superimposed with the idealized two-state trajectory obtained from a Hidden-Markov model (HMM) fit. (e) Baseline-corrected trajectory obtained from the HMM fit. Figure and caption adapted from Ref. [43].

indicates that both states are almost equally probable, i.e., that the equilibrium constant between B1 and B2 is close to 1. When repeating this analysis on multiple, successive 1-s-long segments, we obtain a distribution of $\langle \tau_{high} \rangle / \langle \tau_{low} \rangle$ ratios centered around the case in which $\langle \tau_{high} \rangle$ = $\langle \tau_{low} \rangle$, as presented in Figure 2.18f. The width of the distribution illustrates a level of heterogeneity in the kinetics which is commonly observed in single-molecule measurements. We also performed several controls to ensure that the active phases with rapid two-state RTN

42

are strictly related to the COOH/EDC adduct (Fig. 2.20). First, the observed two-state RTN disappears after flushing the device with fresh buffer, consistent with the fact that the system remains in the unbound state (A) after the EDC molecule is washed away. In addition, none of the three unexposed devices nor the two unfunctionalized devices exhibit any activity when exposed to EDC (Table 2.1). Examples of trajectories for these different types of controls are presented in Figure 2.20. The presence of multisecond-long inactive and active phases, millisecond-scale fast RTN in the active phase, and heterogeneous kinetics centered on $\langle \tau_{high} \rangle = \langle \tau_{low} \rangle$ are all consistent with results reported for the interaction of the EDC molecule with a single carboxylic acid group [114]. Moreover, the ratio of exposed devices exhibiting this specific signature (2 out of 7) is compatible with the proportion of devices functionalized with a single-molecule probe as derived from the earlier, large-array study. This remarkable agreement obtained from two independent experiments (i.e., the conductance change experiment and the real-time reactivity experiment) corroborates the ability of our nanowell-confined chemical approach to produce single-molecule probes with high and reproducible yields. More practically, the presence of this specific COOH/EDC signature can be used as an indicator to identify, from a large array of devices, the set of devices holding a single-molecule probe, which can be further used as a template to support a variety of other individual molecules, as demonstrated in the following chapters.

2.3 Conclusions

The approaches able to produce single-point functionalization described in Sections 2.2.1 and 2.2.2, namely feedback-controlled electrochemical oxidation and noncovalent attachment, rely on unfavorable statistics that result in minimal control of the position and the yield of the chemistry. Moreover, the necessity to individually monitor each device in feedback-controlled methods imposes throughput limitations in the preparation of devices. Noncovalent approaches

also bear time scale limitations in that only short device measurement times are possible due to the instability of the molecule−nanotube coupling. Nanowell-confined chemistry on carbon nanotube devices, presented in Section 2.2.3, provides a versatile platform to support and monitor individual chemical reactions. We obtain a high yield for the attachment of the primary single-molecule probe, and the covalent chemistry ensures strong nanotube-molecule coupling and long-term stability of the adduct. The method is independent of a specific chemical reaction and generalizable to any aqueous nanotube chemistry. It is also easily scalable to the wafer scale, enabling the production of a large number of devices and robust statistical analysis. Once the mask defining the nanowells is removed, the platform supports an even larger variety of reactions and reagents, for instance reactions in organic solvents or bioconjugation with large macromolecules. Successive secondary single-molecule reactions on the same single-molecule probe can be recorded in real time, with submillisecond resolution and for many hours. This platform opens routes to investigate a variety of other fundamental chemical mechanisms such as lifetimes of intermediates in catalytic reactions and to improve chemical sensor and lab-on-chip technology with localized functionality. DNA hybridization studies using smFETs, presented in Section 3.1, were performed using pyrene adsorption. It was determined that nanowell-controlled diazonium chemistry would be used for the G-quadruplex DNA studies discussed in Section 3.2 due to the slow dynamics of this molecule and the need for long-lived attachments. For all riboswitch studies discussed in Chapter 4, where many mutant sequences were investigated, pyrene adsorption was again used due to the benefit of device recyclability with this nanotube functionalization method.

Chapter 3

Studies of DNA Dynamics

3.1   DNA Hybridization

3.1.1   Experimental setup

In an attempt to validate the use of the pyrene noncovalent CNT attachment chemistry presented in Section 2.2.2, we performed studies of DNA hybridization using a 10 nucleotide DNA duplex that has been previously studied using electrochemical oxidation as the CNT functionalization method [41]. The single-stranded DNA to be attached to the nanotube, named the probe DNA, was purchased (Integrated DNA Technologies, HPLC grade) with the following sequence: 5'-$NH_2(CH2)_6$ GTG AGT TGT T-3' with the alkyl amine functionalization placed at the 5' terminus. Additional single-stranded DNAs, named target DNAs, were purchased (Integrated DNA Technologies, HPLC grade) with sequences as noted in Table 3.1. The sequences of the target DNAs were designed to investigate the effects of a single mismatch on DNA hybridization dynamics and to determine whether the mismatch position affected the ability of smFET devices to detect the mismatch. After functionalization of smFET devices with 1-pyrenebutyric acid *N*-hydroxysuccinimide (NHS) ester (Sigma Aldrich, 95%) as described in Section 2.2.2,   we introduced 10 µM of the 5'-amino-modified probe DNA oligomer in a sodium phosphate buffer

Table 3.1. Summary of target DNA sequences. Melting temperature (T_m) were calculated at room temperature with 100 nM target DNA in sodium phosphate buffer (45 mM, pH 8.0) using the nearest neighbor method [132].

	DNA ID	Sequence	T_m
1	Noncomplement	5'-TCT GTC GTG G-3'	n/a
2	Complement	5'-AAC AAC TCA C-3'	22.3 °C
3	CNT-side mismatch	5'-AAC AAC TCA T-3'	19.5 °C
4	Solution-side mismatch	5'-TAC AAC TCA C-3'	19.9 °C

solution (45 mM, pH 8.0) for 30 min. The 5' amino moiety reacts with the NHS ester [117] to form an amide bond between the 5' terminus of the DNA oligomer and the alkyl chain on the pyrene probe adsorbed to the nanotube sidewall. After the reaction, the flow cell was flushed with fresh sodium phosphate buffer (45 mM, pH 8.0) for 10 min to rinse away any residual unconjugated DNA oligomer.

3.1.2 smFET DNA hybridization signals are two-state and temperature-dependent

After functionalization with the DNA probe we measured the conductance of the device array in real-time for 15 minutes, with V_{DS} set between 10 and 100 mV to maintain a tens to hundreds nA-scale current and V_L = −300 mV. The conductance of the devices was recorded at room temperature in the presence of 100 nM complementary DNA in sodium phosphate buffer (45 mM, pH 8.0). Under these conditions, candidate devices exhibit fluctuations between a low-current state centered at 294 nA and a high-current state centered at 314 nA, as shown in the baseline-corrected trajectory in Figure 3.1a. Subsequently raising the temperature of the system using a Thermostream and allowing 15 minutes for thermal equilibrium to be reached, we observed a shift in the two-state equilibrium towards the high-conductance state (Fig. 3.1b and c). This is consistent with observations with this short DNA duplex tethered via electrochemically-oxidized smFET devices which assigned the low-conductance state to the DNA duplex and the high-conductance state to the single-stranded DNA probe [41]. Attempts to probe these effects at higher temperatures were hampered by promoted desorption of the pyrene, and therefore the attached DNA probe, from the surface of the smFET.

3.1.3 smFETs can distinguish single mismatches in DNA hybridization

To further characterize the smFET DNA hybridization signal beyond pairing with the complementary DNA target, we performed measurements in sodium phosphate buffer (45 mM, pH 8.0) with 100 nM of one of the three additional DNA target sequences presented in Table 3.1. The aim of these experiments was to ascertain whether smFETs are sensitive to single
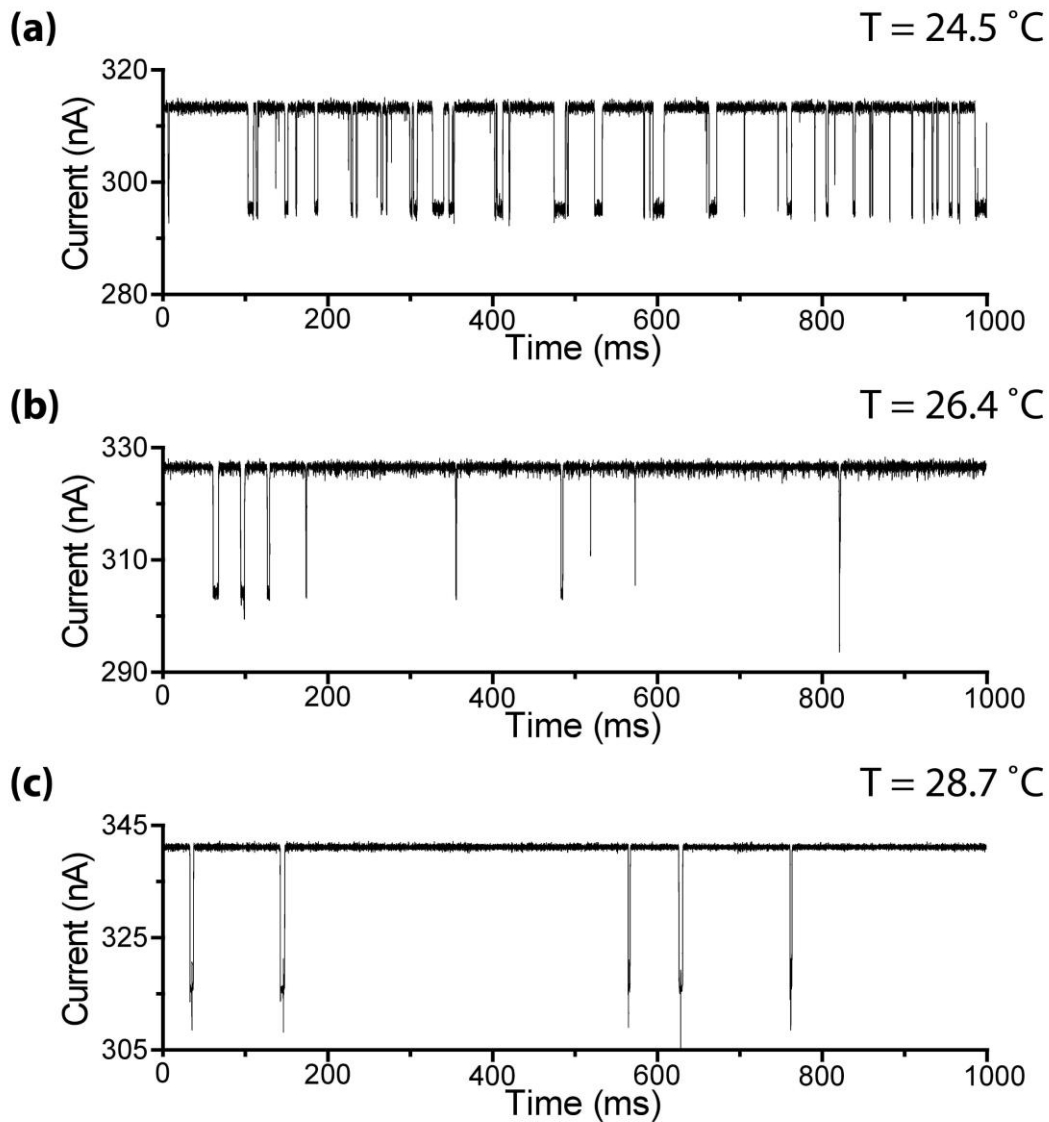
Figure 3.1. DNA hybridization dynamics are sensitive to temperature. Measurements with 100 nM complementary DNA in sodium phosphate buffer (45 nM, pH 8.0) at (a) 24.5 °C (b) 26.4 °C and (c) 28.7 °C .

mismatches in a short DNA duplex, and furthermore whether the location of this mismatch relative to the CNT tethering point affects the smFET DNA hybridization signal. As discussed in Section 1.2.3, due to Debye screening effects smFET signals are sensitive to the distance between the CNT sidewall and the charged species responsible for conductance fluctuations. This relationship was tested explicitly in previous studies using the same 10 nucleotide DNA probe sequence and DNA target sequences missing one or two nucleotides closest to the CNT
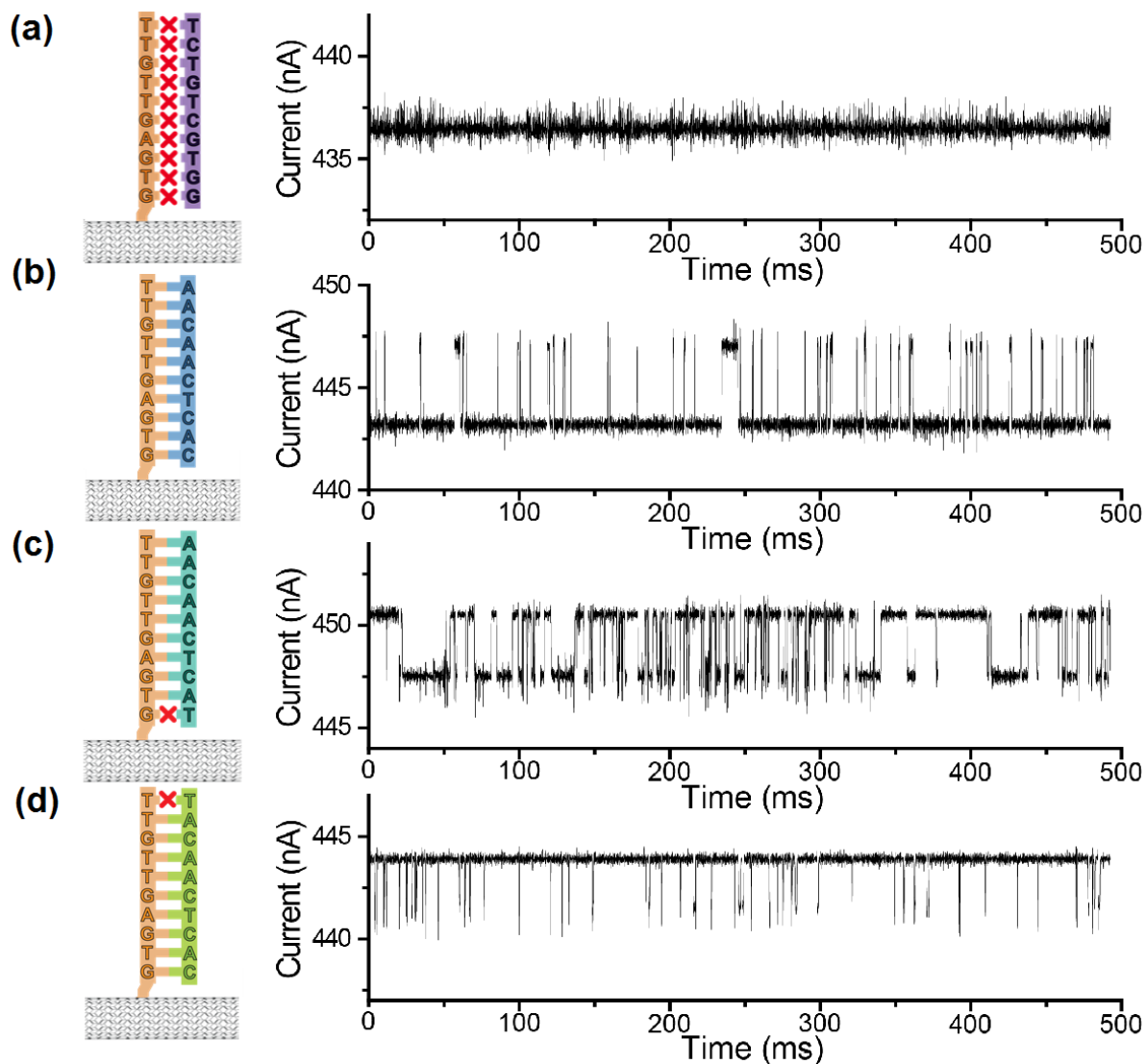
Figure 3.2. DNA hybridization dynamics are sensitive to target DNA sequence. (a) Noncomplementary DNA shows no current fluctuations. (b) Complementary DNA shows two-state activity that has been shifted toward the upper state in the case of both (c) the CNT-side mismatched DNA and (d) the solution-side mismatched DNA.

sidewall [42]. For each of these truncated sequences the two-state DNA hybridization signal was observed to shift away from the hybridized duplex DNA state. Additionally the magnitude of conductance fluctuations decreases as the target DNA strand is shortened, consistent with Debye screening theory [42]. Here we keep the target DNA length constant but alter the location of a single mismatch from CNT-side to solution-side. As shown in Figure 3.2, the two-state smFET signal observed with the complementary DNA probe is absent in the presence of 100

nM noncomplementary DNA and is altered significantly with a single nucleotide mismatch DNA. It is significant to note that while the smFET signal for these target DNA sequences is similar, each is distinct enough to allow discrimination between complement and single-mismatch as well as the location of the mismatch. An extremely short-lived third state with a lowered conductance value is visible in the CNT-side mismatch case. This additional state could be explained by fluctuations of the CNT-side unpaired nucleotide towards the CNT surface, which would increase the negative charge near the smFET and lower the conductance under our experimental conditions.

Analyzing these two-state DNA hybridization signals using a hidden Markov model, we obtained transition rates between the hybridized (low-current) and melted (high-current) states. (Fig. 3.3) Consistent with a simple two-state binding model, in the case of both the CNT-side and solution-side mismatched DNA it is the DNA melting rate that is sensitive to mismatches in the target DNA sequence. The free energy of the DNA duplex formation, ΔG, can be determined from the measured transition rates, k_{on} and k_{off}, for each sequence as follows:

$$\Delta G = -RT\ln K_D$$

where R is the universal gas constant, T is the temperature of the system, and K_D is the dissociation constant, equal to the ratio between k_{off} and k_{on}. A comparison of the free energies derived from smFET analysis compare favorably to those calculated using the nearest-neighbor method as presented in Table 3.2 [132], [133]. Notably, our smFET devices consistently overestimate the stability of duplex DNA (see Table 3.2). It is likely that this effect is caused by the existence of an electrical double layer (EDL) whereby, due to the gate bias placed on solution, the concentration of DNA target and/or ions of opposite charge is greater near the surface of the smFET than the bulk value in solution [134]. Further studies using various gate biases would need to be conducted in order to verify this hypothesis.
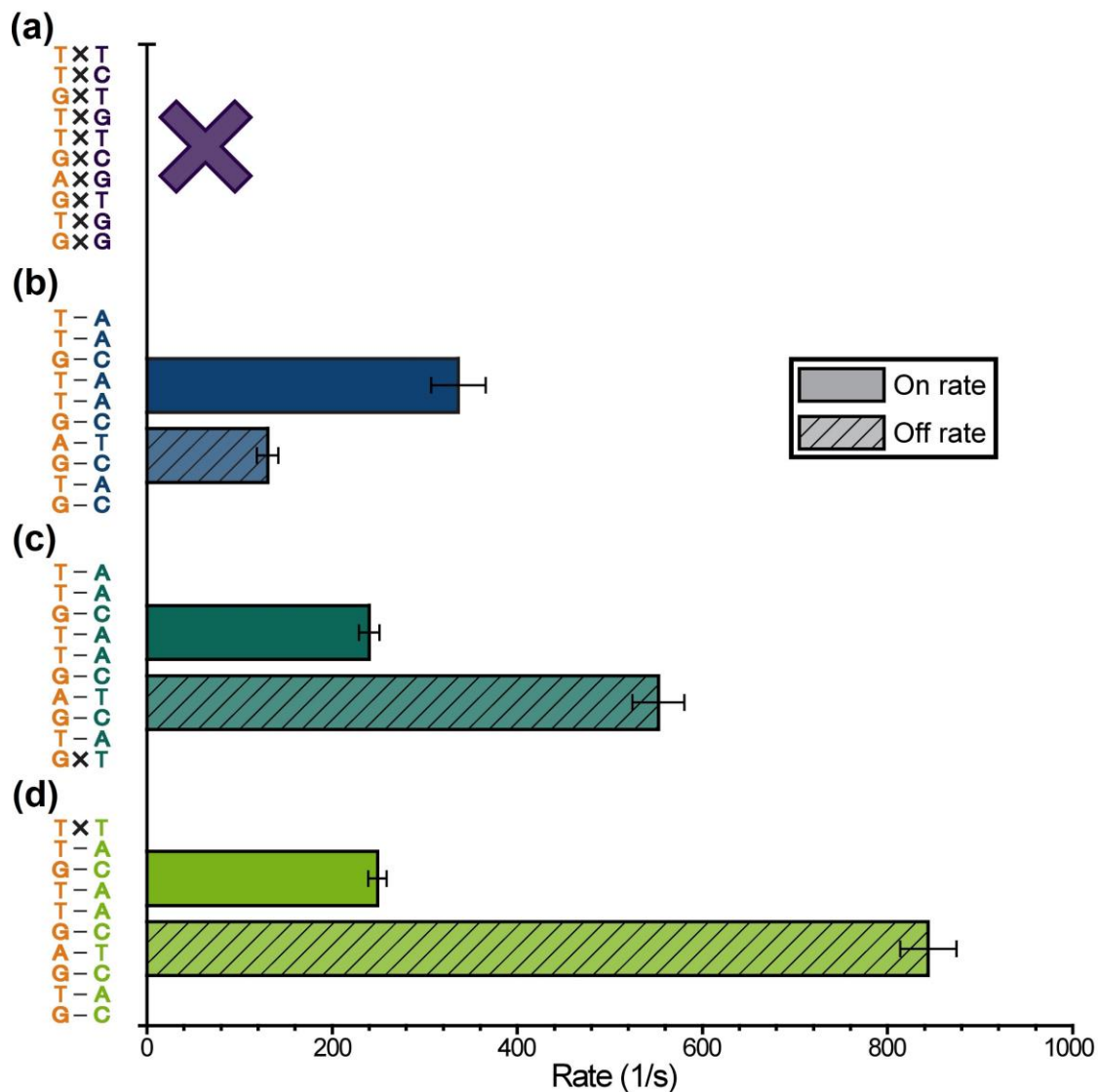
Figure 3.3. DNA hybridization observed on and off rates in the presence of 100 nM target DNA determined using HMM analysis. No transitions were observed in the case of (a) noncomplementary DNA. (b) Complementary DNA and both (c) CNT-side mismatched DNA and (d) solution-side mismatched DNA rates are plotted.

Table 3.2. Summary of target DNA sequences. Melting temperature (T_m) were calculated at room temperature with 100 nM target DNA in sodium phosphate buffer (45 mM, pH 8.0) using the nearest neighbor method [132].

	DNA ID	Sequence	$\Delta G_{predicted}$	$\Delta G_{observed}$
1	Noncomplement	5'-TCT GTC GTG G-3'	>0	n/a
2	Complement	5'-AAC AAC TCA C-3'	-9.08	-10.1 ± 0.0741
3	CNT-side mismatch	5'-AAC AAC TCA T-3'	-8.37	-9.05 ± 0.0406
4	Solution-side mismatch	5'-TAC AAC TCA C-3'	-8.38	-8.82 ± 0.0316

3.2   G-Quadruplex Dynamics†

3.2.1   Experimental setup

Here we demonstrate the ability of the smFET platform to support a second level of functionalization after the nanowell-confined aryl diazonium chemistry described in Section 2.2.3, by covalently tethering an individual biomolecule to the primary single-molecule probe and measuring its conformational dynamics in real-time. For these experiments, we use a 24-nucleotide, 5′-amino-modified, single-stranded DNA oligomer that models human telomeric DNA in that it is composed of four repeats of the TTAGGG guanine-rich sequence typically found in the terminal, single-stranded, telomeric region of human chromosomes [135]. The DNA oligomer was purchased (Integrated DNA Technologies, HPLC grade), with the following sequence: 5'-$NH_2(CH2)_6$ AGA GGG TTA GGG TTA GGG TTA GGG-3' with the alkyl amine functionalization placed at the 5' terminus. This sequence can fold into a structure called a G-quadruplex that is comprised of a series of stacked guanine tetrads as illustrated in Figure 3.4a. Monovalent cations, in particular K^+ and, to a lesser extent, Na^+, stabilize the folded form of the G-quadruplex sequence by binding between (K^+) or within (Na^+) the plane of the guanine tetrads [136]–[138].

On the same microfluidic-integrated array of ten smFETs described in Table 2.1, we covalently attached the 5′-amino-modified DNA oligomer to the primary single-molecule probe on the carbon nanotube via an amide bond formed using a two-step EDC/NHS coupling protocol [117]. In the first reaction, the carboxyl termination of the single-molecule probe was activated using 1 mM EDC (Thermo Scientific) and 1 mM NHS (Sigma-Aldrich 98%) in dimethylformamide (DMF) for 10 minutes [116]. In the second reaction, we introduced 100 µM of the 5'-amino-modified DNA oligomer in a sodium phosphate buffer solution (100 mM, pH 8.4) for 30 minutes. The 5' amino moiety reacts with the NHS ester [117] to form an amide bond
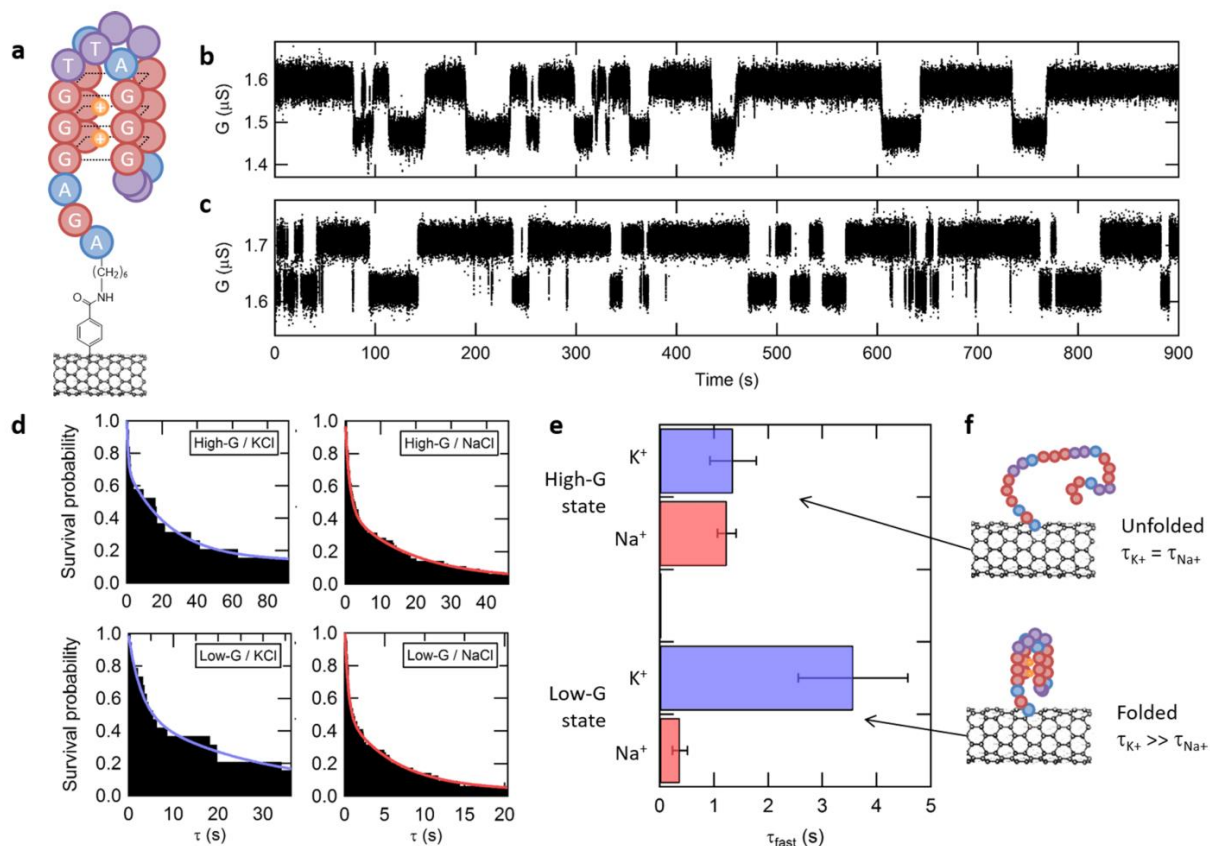
Figure 3.4. Single-molecule observation of DNA G-quadruplex folding. (a) Representation of a folded G-quadruplex DNA sequence capturing two K^+ cations, bound to an initial single-molecule probe on a nanotube. (b−c) Real-time trajectories with baseline correction, showing two-state fluctuations in conductance in the presence of 10mM KCl or NaCl, respectively. (d) Survival probability plots for each conductance state (high-G/low-G) and each ion type (K^+/Na^+) are fitted with a double-exponential kinetic model. (e) Average lifetime $\langle\tau_{fast}\rangle$ and error bars extracted from the survival plots in panel d for the high-G and low-G states as well as both K^+ and Na^+ ions. (f) High-G and low-G conductance states are attributed to the unfolded and folded DNA configurations, respectively. The folded configuration is found to have a longer lifetime in the presence of K^+ cations than Na^+. Figure and caption adapted from Ref. [43].

between the 5' terminus of the DNA oligomer and the carboxyphenyl single-molecule probe on

the nanotube. After the reaction, the flow cell was flushed with Tris-HCl buffer (10 mM, pH 7.5)

for 10 minutes at 45 °C to rinse away any residual unconjugated DNA oligomer, EDC and NHS

traces, and the Na^+ ions that were introduced from the sodium phosphate buffer.

3.2.2 G-quadruplex DNA exhibits a salt-dependent two-state smFET signal

After functionalization with the DNA oligomer, we measure the conductance of all ten devices in real time and at room temperature, with V_{DS} = 100 mV and V_L = −300 mV. The conductance of the devices is recorded in real-time for 15 minutes in Tris-HCl buffer (10 mM, pH 7.5) supplemented with 10 mM KCl. Under these conditions, one device exhibits fluctuations between a low-conductance state (low-G) centered at 1.49 µS and a high-conductance state (high-G) centered at 1.61 µS, as shown in the baseline-corrected trajectory in Figure 3.4b (raw traces are provided in Figure 3.5). After once again flushing the flow cell thoroughly, we collect real-time data for 15 minutes and at room temperature in Tris-HCl buffer supplemented with 10 mM NaCl. As observed in the presence of K^+, the trajectory recorded in the presence of Na^+ shows fluctuations between a low-G state and a high-G state, respectively centered at conductance values of 1.64 µS and 1.73 µS (Fig. 3.4c). A control experiment recorded using the same device, but in the presence of only the Tris-HCl buffer (i.e., in the absence of K^+ or Na^+ ions), does not exhibit such fluctuations, which is consistent with other studies reporting only weak interaction between pristine carbon nanotubes and G-quadruplex DNA [139], [140]. Similarly, measurements using an unexposed control device do not exhibit such fluctuations, either in the presence of KCl or NaCl. Each of these controls is presented in Figure 3.6.

In order to rigorously assign the low-G and high-G states to configurations of the G-quadruplex oligomer, we perform a statistical analysis of the transitions between these states. To do so, we use a hidden Markov model as previously described [41], [109], [110] to calculate the most probable sequence of transitions between the low-G- and high-G states forming the trajectories (i.e., the idealized paths) (see Fig. 3.5). Survival probability plots of the dwell times spent in low-G state prior to transitioning to the high-G state and, conversely, of the dwell times spent in high-G state prior to transitioning to the low-G state are shown in Figure 3.4d.
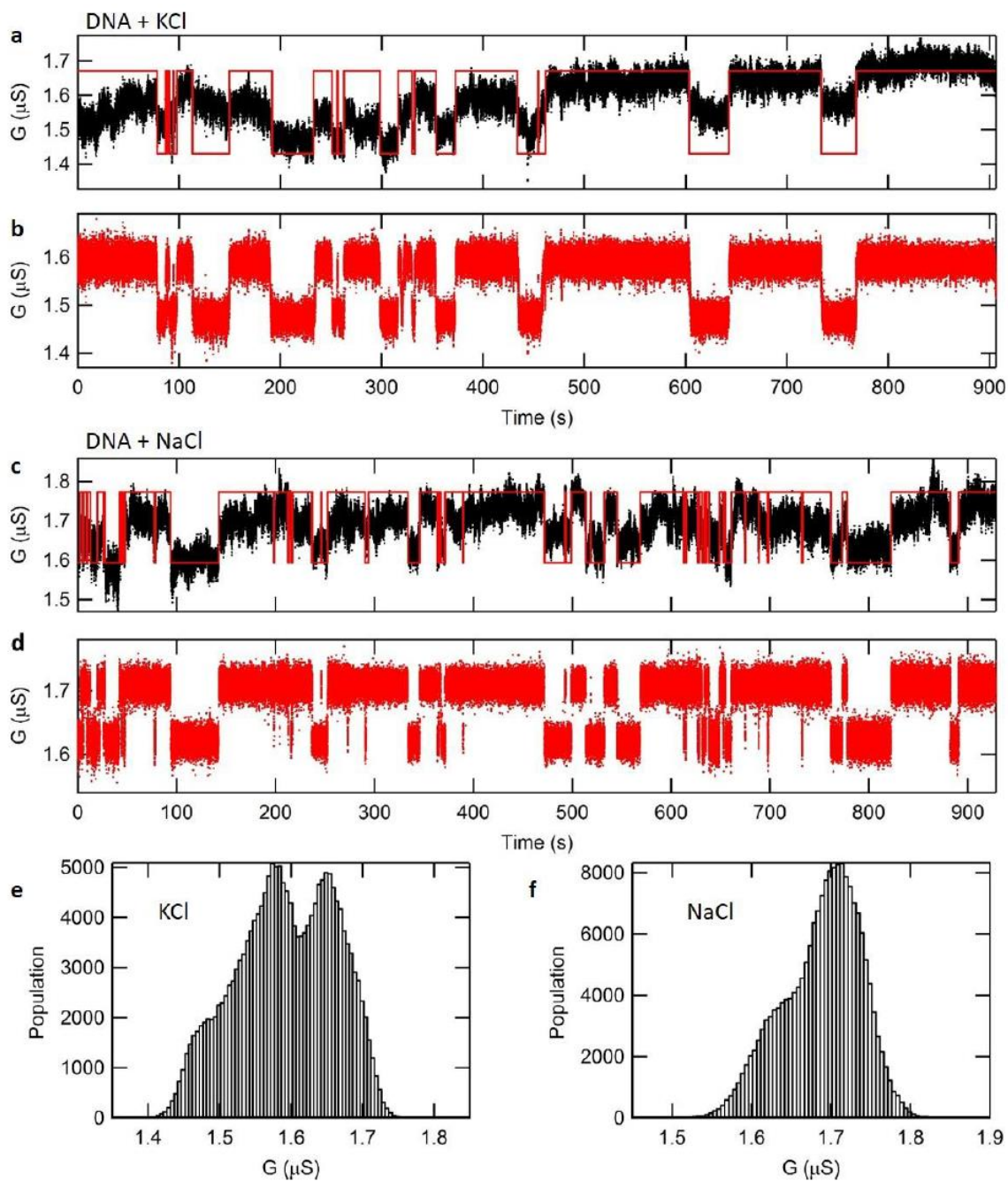
Figure 3.5. Real-time trajectories for DNA activity. (a) Full raw trajectory in presence of 10mM KCl, superimposed with the idealized trajectory (red) obtained from the HMM fit. (b) Baseline-corrected trajectory for KCl environment, according to the HMM fit. (c) Full raw trajectory in presence of 10mM NaCl, superimposed with the idealized trajectory (red) obtained from the HMM fit. (b) Baseline-corrected trajectory for NaCl environment, according to the HMM fit. (e) Distribution of conductance values for the KCl trace in a, showing two peaks as indicative of two-state dynamics. The shoulder seen on the left side is attributed to the slow drift of the conductance baseline. (f) Distribution of conductance values for the NaCl trace in a, showing two peaks as indicative of two-state dynamics. Figure and caption adapted from Ref. [43].

54
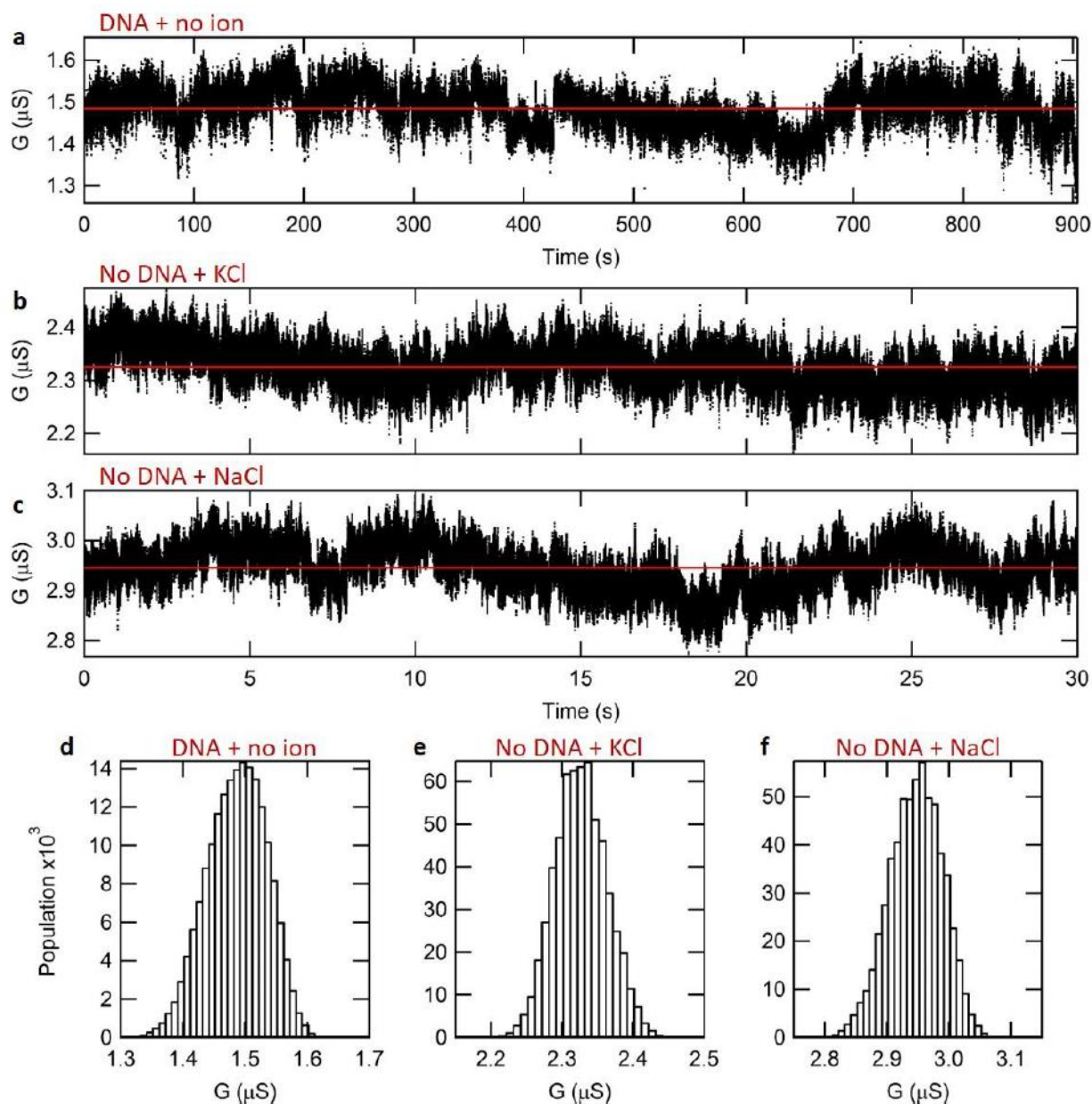
Figure 3.6. Real-time trajectories for DNA activity. (a) Full raw trajectory for DNA in buffer in absence of any monovalent cation like K+ or Na+. Superimposed is the average value of the conductance. (b/c) Raw trajectories for a control device in presence of 10mM KCl (b) and 10mM NaCl (c). Superimposed is the average value of the conductance. (d/e/f) Distribution of conductance values in the above traces, showing a single Gaussian shape indicative of single-state dynamics. Figure and caption adapted from Ref. [43].

3.2.3 G-quadruplex folding and unfolding rates are cation-specific

Consistent with previous single-molecule biophysical studies of G-quadruplex sequences [136], [141], [142], each survival probability plot is best described by a double exponential decay function (Fig. 3.7), yielding two characteristic lifetimes (τ_{fast} and τ_{slow}) for both the low- and high-G states (see Table 3.3). While the small number of long dwells that predominantly contribute to τ_{slow} render this lifetime particularly susceptible to the effects of possible missed transitions, the much larger number of short dwells that predominantly contribute to τ_{fast} render this lifetime
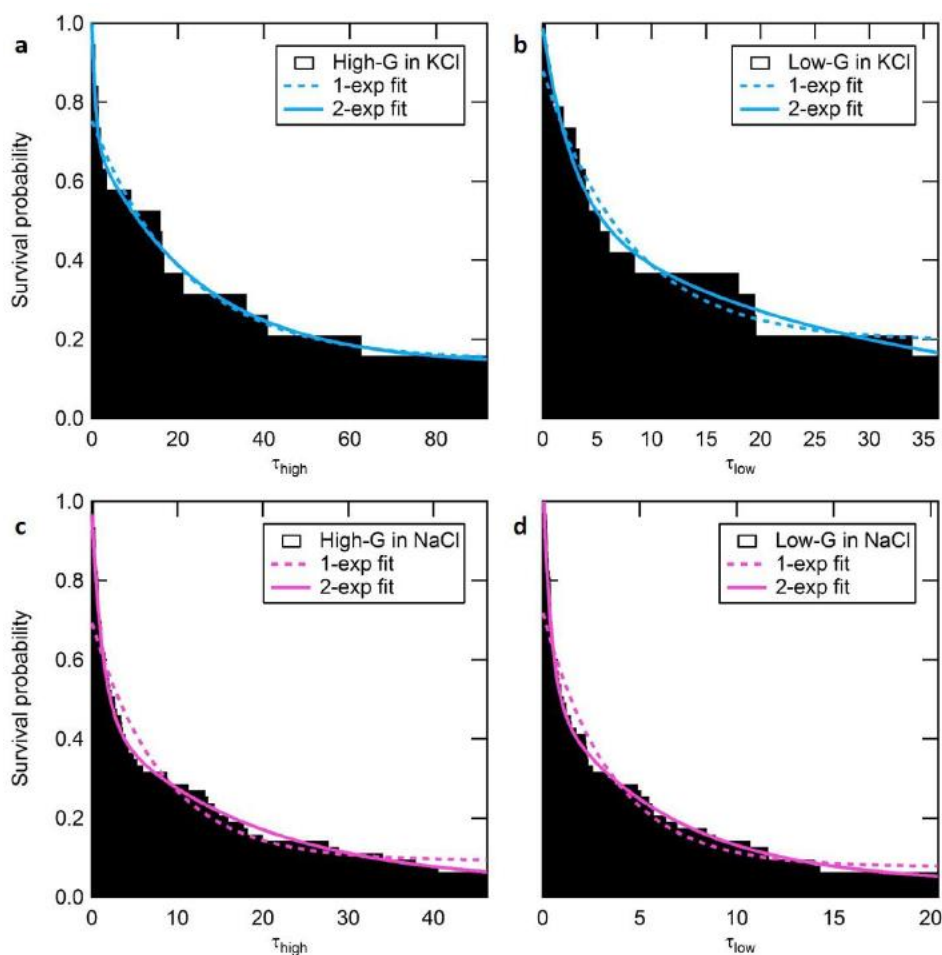
Figure 3.7. Survival probability for transitions from high-G to low-G state (left) and low-G to high-G state (right) as a function of dwell time. Data obtained in the presence of K+ ions (top) or Na+ ions (bottom). 18 distinct dwells were identified in the K+ idealized trace, and 53 dwells in the Na+ idealized trace. Dotted lines show fits with a simple exponential model and plain lines show fits with a double-exponential model. The double-exponential model is a better fit in each case, as it captures both the short-lived and long-lived dwells. Figure and caption adapted from Ref. [43].

Table 3.3. Characteristic lifetimes of low-G and high-G states, in presence of K+ or Na+ ions. Time constants are obtained from the double-exponential fits in Fig. 3.4. Errors are obtained from standard bootstrapping.

		Lifetimes (s)		Error on lifetimes (s)		DNA state
		τ_{fast}	τ_{slow}	$\Delta\tau_{fast}$	$\Delta\tau_{slow}$	
High-G	K+	1.354	75.036	0.42876	38.282	**Unfolded**
	Na+	1.0832	21.252	0.17153	2.6706	
Low-G	K+	3.5682	34.191	1.0119	7.6984	**Folded**
	Na+	0.44885	10.042	0.13827	2.0055	
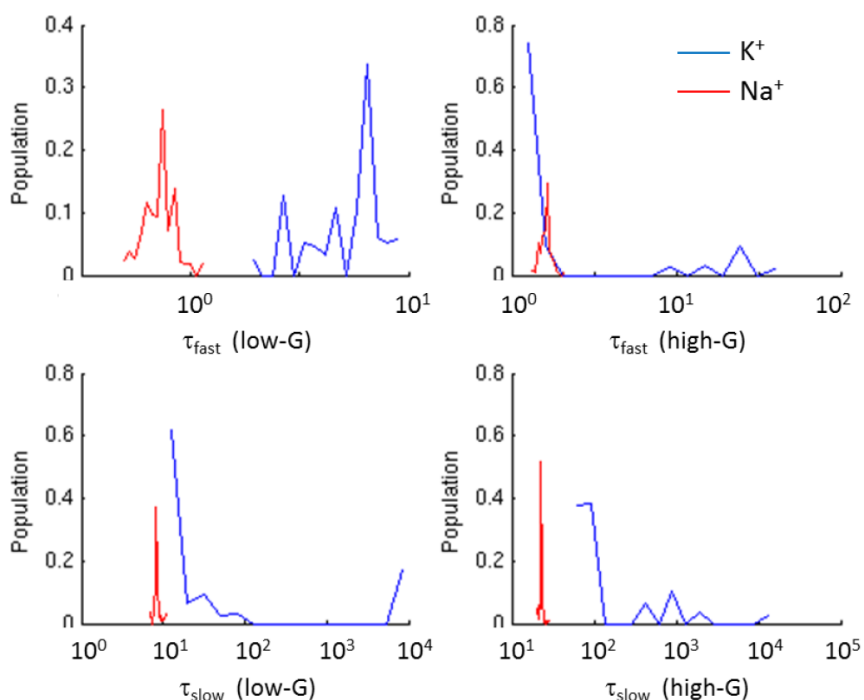
Figure 3.8. Stability of τ estimates with respect to dwell assignation. Lifetime estimates for each state were calculated 1000x with the introduction of a random dwell inversion. Fast lifetimes form well-delimited distributions, indicating good stability in regard to dwell assignation errors; slow lifetime distributions are on the contrary very sensitive to dwell assignation, due to the fact that they are much less sampled in the trajectories. Figure and caption adapted from Ref. [43].

significantly resistant to the effects of possible missed transitions (Fig. 3.8). Consequently, τ_{fast} is a much more robust lifetime measurement and is therefore presented in Figure 3.4e for each state and each ion type. For the low-G state, we find that τ_{fast} obtained in the presence of K+ is 10 times longer than that obtained in the presence of Na+. In contrast, for the high-G state, we find that τ_{fast} obtained in the presence of K+ is within error of that in the presence of Na+.

Previous studies of G-quadruplex sequences similar to that investigated here have demonstrated that, at any particular monovalent ion concentration, the folded form of the G-quadruplex sequence should be more stable in the presence of K^+ versus Na^+, whereas the stability of the unfolded form should be independent of the identity of the ion [143]. Given that all of our experiments are conducted at the same monovalent ion concentration and given our finding that K^+ stabilizes the low-G state by a factor of 10 over Na^+, whereas the stability of the high-G state is independent of the identity of the ion, we unambiguously assign the low-G and high-G states of the trajectories to the folded and unfolded forms of the G-quadruplex sequence, respectively (see Fig. 3.4f). We note that the values of τ_{fast} for both the folded and unfolded forms of the G-quadruplex sequence reported here are in close agreement with the corresponding lifetimes of the folded and unfolded forms of a similar G-quadruplex sequence obtained from smFRET studies performed under similar experimental conditions to those used here [136]. In addition, the existence of two classes of dwells (i.e., τ_{fast} and τ_{slow}) in both the folded and unfolded forms of the G-quadruplex sequence is fully consistent with previous smFRET studies of similar G-quadruplex sequences [136], [144]. The close correspondence between our results and the results of smFRET studies of analogous G-quadruplex sequences suggests that tethering of the G-quadruplex to the surface of the carbon nanotube device does not impair the folding/unfolding dynamics of the G-quadruplex. This observation validates the use of the smFET devices described here for single-molecule studies of biomolecular folding and structural dynamics. Notably, the label-free-, increased time-resolution-, and expanded observation time aspects of the smFET approach described here should enable investigations of biomolecular folding reactions and dynamic processes that are currently difficult or impossible

---

to investigate using more conventional single-molecule biophysical approaches such as smFRET [145], single-molecule force spectroscopy [30], or single-molecule tethered-particle motion [146] approaches.

Chapter 4

Studies of Riboswitch Dynamics

4.1 Overview of the *pbuE* Riboswitch

Purine-sensing riboswitches are one of the most well-studied riboswitch classes due to their relatively small size. Found in bacterial species such as *Bacillus subtilis* and *Vibrio vulnificus,* purine riboswitches have been found to be involved in both transcriptional control and translational control as both on and off switches for the genes they regulate. A model purine riboswitch is the adenine-sensing *pbuE* riboswitch found in *Bacillus subtilis*, which has been studied using a variety of single-molecule and ensemble techniques, as well as by molecular dynamics (MD) simulation [147]–[153]. The *pbuE* riboswitch sequence consists of an aptamer domain that is responsible for recognition and binding of the target metabolite adenine, an expression platform domain that is responsible for forming the terminator hairpin that interacts with transcription machinery, and a switching sequence that belongs to both domains [147]. In the absence of adenine the aptamer structure gives way to formation of the more stable terminator hairpin, which arrests production of mRNA. Adenine binding, however, provides stability to the aptamer, inhibiting the formation of the terminator hairpin and allowing mRNA production and expression of the *pbuE* gene to continue (Fig. 4.1). Because the *pbuE* gene encodes an adenine efflux pump, this cycle forms a negative feedback loop. The rate of adenine association and uptake into the aptamer *versus* the rate of transcription forms the central competition affecting the outcome of riboswitch regulation [154], [155]. This kinetic balance affects both the generation of the expression platform and the relative position of RNA polymerase (RNAP) to the riboswitch, both of which are thought to play a more significant role in

the regulatory ability of the *pbuE* riboswitch than ligand binding thermodynamics alone [149], [154], [155].
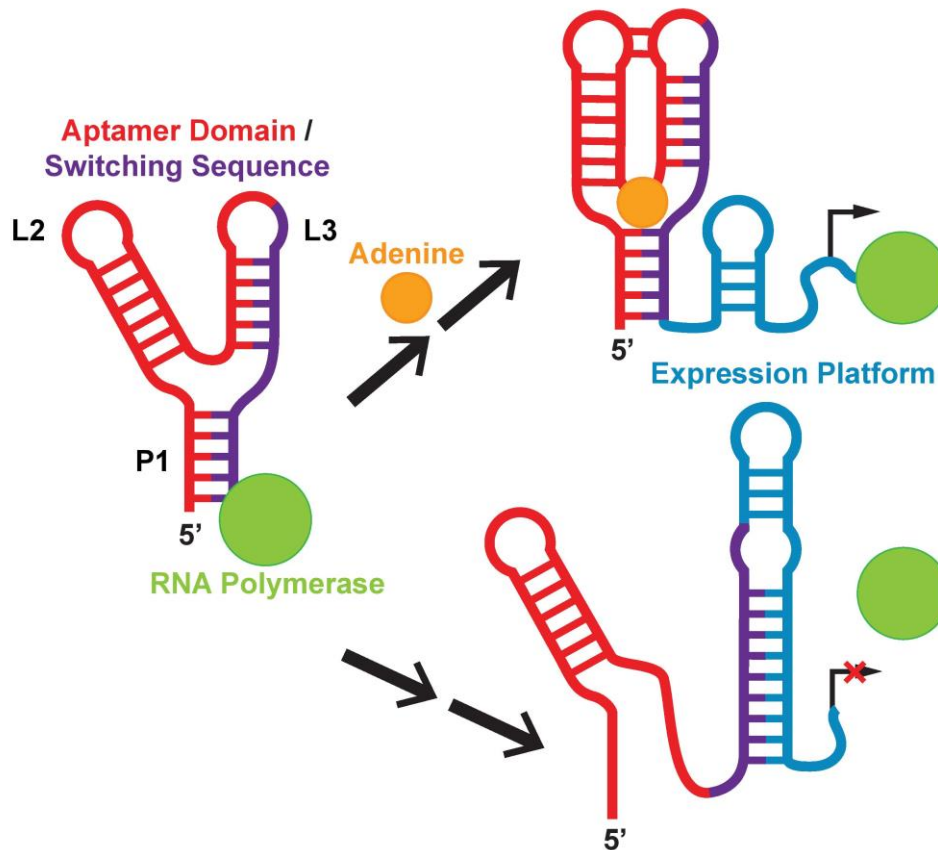
Figure 4.1. Transcriptional regulation of the *pbuE* gene by its riboswitch. In the absence of adenine the transcription of the expression platform results in the formation of a terminator hairpin which prevents transcription of the *pbuE* gene. If adenine binds in the aptamer binding pocket, transcription of the expression platform results in the formation of an antiterminator hairpin and expression of the *pbuE* gene is allowed.

Following adenine binding to the *pbuE* riboswitch, further regulation is required to communicate the decision to RNAP. This is accomplished by adenine-induced stabilization of the first five and last five nucleotides of the aptamer domain into a five base pair helix, known as the P1 stem [156]. Formation of the P1 stem sequesters base pairs required by the expression platform to form the terminator hairpin, making it a critical component of the *pbuE* riboswitch regulatory mechanism [148]. However, dynamics of the P1 stem, consisting entirely of base-pair rearrangements, are difficult to characterize because both the lifetimes as well as the distance

scales of base pairing are short [157]–[160]. Structures of purine family riboswitches [148], [161], [162], as well as NMR characterizations of solution conformations [163]–[165] and smFRET studies [150], [166], have established that the tertiary structure of the *pbuE* riboswitch transitions to its native state following binding of adenine. Furthermore, in the bound state, more than 90% of the solvent exposed surface of adenine is surrounded by RNA, leading to the suggestion that adenine entering the binding pocket is coupled with significant structural changes in the aptamer domain [148], [161], [163], [164]. It is unclear, however, how stabilization of the binding pocket and formation of the tertiary structure of the aptamer domain of the riboswitch influence the stability of the P1 stem and therefore the transcription of the *pbuE* gene.

Structural rearrangements of the P1 stem, either to allow ligand recognition or in response to ligand binding, are critical aspects of regulation by the *pbuE* gene that to date have not been investigated at the single-molecule level [150], [151]. The single-molecule biophysical techniques most commonly used to probe riboswitches, fluorescence resonance energy transfer (smFRET) and single-molecule force spectroscopy, have difficulty measuring millisecond-scale dynamics, such as base pair rearrangements, as well as observing unperturbed individual molecules for long times.

Here we identify adenine-dependent dynamics of the P1 stem of the *pbuE* riboswitch aptamer on the microsecond timescale by correlating smFET conductance fluctuations with predicted RNA structural rearrangements and by mutagenesis of the aptamer sequence. We demonstrate how long-lived, ligand-dependent intermediates form at a base pair level and describe their consequence for riboswitch-regulation by adenine uptake into the aptamer. Using smFET technology we have achieved the first observation of RNA zipping and unzipping at the single-molecule level, as well as label-free observations of the effects of a three-way junction motif on helix zipping and unzipping.

4.2   Effects of Salt on RNA Stability

As discussed in Sections 1.2.3 and 1.3.2, CNTFET sensitivity and RNA dynamics are both dependent on salt concentration. In order to determine buffer conditions for smFET experiments that both (i) maximize device sensitivity to changes in local charge density by reducing ionic strength and (ii) maintain sufficient salt to approximate *in vivo* RNA dynamics, a bulk fluorescence assay was used under a range of salt concentrations. It has been shown that the *pbuE* riboswitch binds adenine and 2-aminopurine (2AP) with similar affinity [147], though the measured rate of association of these metabolites varies by a factor of three [149]. As has been reported elsewhere, 2AP can be selectively excited and its fluorescence, which is quenched by base stacking [167], can be monitored to measure quenching caused by binding to the *pbuE* riboswitch aptamer [150]. We performed fluorescence-quenching assays using a Perkin Elmer LS55 luminescence spectrophotometer and collected spectra over the wavelength range 330-450 nm with 300 nm excitation. RNA samples (prepared using *in vitro* transcription and purification as described previously [168]) were heated to 95°C for 2 minutes in either 0.01X, 0.1X, or 1X phosphate-buffered saline (PBS) followed by slow cooling to 25°C before addition of 10 mM $MgCl_2$ to allow for proper folding of the aptamer. The concentration of PBS rather than $MgCl_2$ was reduced due to the critical importance of divalent cations in the formation of RNA tertiary contacts such as those between the L2 and L3 loops of the *pbuE* riboswitch aptamer [169]. Data was collected at 25°C with a fixed 2AP concentration of 50 nM and a range of RNA concentrations in excess of 2AP to simplify the ligand binding equation to:

$$\Delta F/F = (1-\alpha)[RNA]/(K_D + [RNA])$$

where $\Delta F/F$ is the percent fluorescence intensity lost upon the addition of a known concentration of riboswitch, [RNA]. The parameter α is proportional to the quantum yield of 2AP fluorescence and K_D represents the equilibrium dissociation constant of 2AP from the riboswitch [150]. As shown in Figure 4.2, with 10 mM $MgCl_2$ a change in monovalent salt between 0.01X and 1X

PBS does not significantly affect the binding of 2AP to the *pbuE* aptamer. Using the binding equation presented, the K_D value was determined for each concentration and compared against the previously reported value of 300 nM (Table 4.1) [147]. Using these results it was determined that all smFET experiments on the *pbuE* aptamer could be performed under reduced monovalent salt conditions, namely in 0.1x PBS, without perturbing adenine binding.
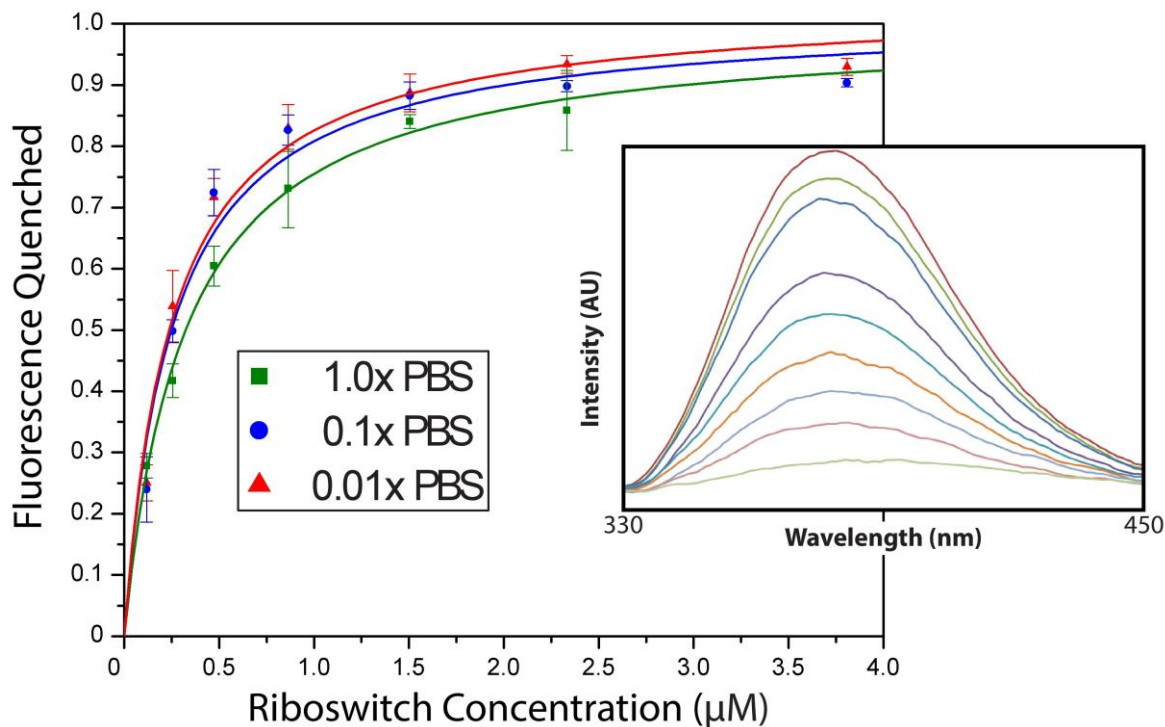
Figure 4.2. Fluorescence quenching assay of 2AP binding to the *pbuE* riboswitch aptamer measured with 10 mM $MgCl_2$ and varying PBS concentrations at 17°C. The inset shows an example RNA titration which quenches fluorescence of 2AP.

Table 4.1. Measured K_D values for 2AP binding to the *pbuE* aptamer where 1.0x PBS represents a pH 7.4 buffer consisting of 10 mM phosphate, 137 mM NaCl, and 2.7 mM KCl.

Salt Concentration	K_D (nM)
0.01x PBS	252 ± 40.
0.1x PBS	255 ± 49
1.0x PBS	322 ± 26

4.3   smFET Experimental Setup

RNA sequences for single-molecule experiments were purchased (GE Dharmacon, HPLC purified and 2'-ACE protected) with primary amine functionalities, either 5'-Amino modifier C6 for labelling at position U1 or 5-Aminoallyl-uridine for internal modification at U20 (Fig. 4.3). RNA samples were incubated at 60°C in 100 mM acetic acid, pH 3.8 for 30 minutes in order to remove the 2'-ACE group followed by ethanol precipitation, lyophilization, and resuspension in 0.1X PBS [170]. RNA samples were heated to 95 °C for 2 minutes followed by slow cooling to room temperature before addition of 10 mM $MgCl_2$. This thermal refolding of the riboswitch has the additional benefit of precluding interactions between the RNA and the CNT, which require the nucleic acid sequence to be entirely unpaired as well as to possess a particular base composition [139], [140]. After functionalization of smFET devices with 1-pyrenebutyric acid NHS ester as described in Section 2.2.2, devices were incubated in a solution of 10 µM amine-functionalized RNA and 10mM $MgCl_2$ in 10 mM sodium phosphate buffer, pH 8.4 for 10 minutes. After the incubation period the system was flushed with 10mM $MgCl_2$ in 0.1X PBS. After functionalization the platinum electrodes were set to V_L = -300 mV while V_{DS} was set between 10 and 100 mV in order to maintain a tens to hundreds nA-scale current for all measured devices. Between measurements 10 mM $MgCl_2$ in 0.1X PBS was flowed through the system before incubating the system in the desired buffer for 15 minutes and beginning data collection. Extensive flushing of water and DMSO at 80°C was used to clean the microfluidic flow cell between experiments with different RNA sequences.

4.4   Results of *pbuE* Riboswitch Aptamer Studies

4.4.1   The wild-type P1 stem zips and unzips discretely and sequentially on the millisecond time-scale
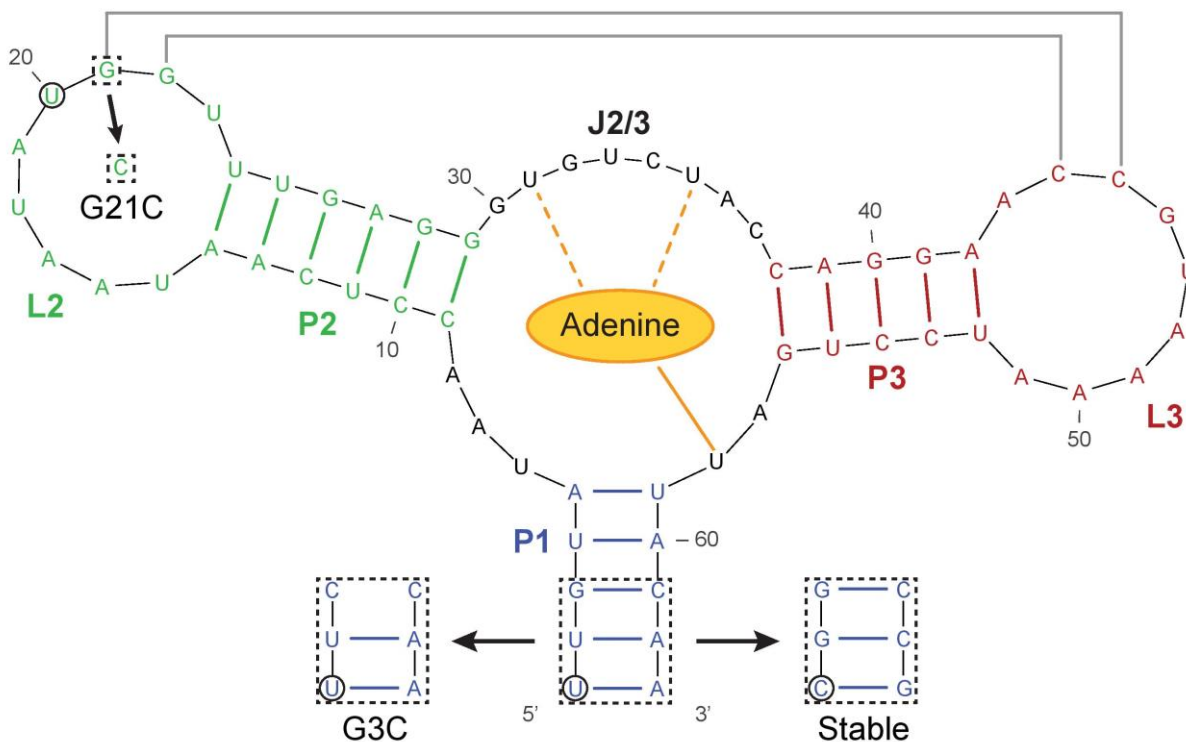
Figure 4.3. Sequence of the *pbuE* riboswitch aptamer with secondary and select tertiary interactions shown. The base pairs of the P1, P2, and P3 stems are colored blue, green, and red, respectively. Adenine interactions in the aptamer binding pocket are shown in orange. Tertiary contacts between loops L2 and L3 are shown in gray. A single-point mutant of the L2 sequence, G21C, disrupts this interaction. Mutagenesis of the P1 stem to a less stable G3C construct and a more stable construct are shown in dashed boxes. The circled nucleotides at positions 1 and 20 denote the sites for amine modification and subsequent tethering to smFET devices.

To characterize rearrangements of the P1 stem (Fig. 4.3), we used riboswitch aptamer sequences with a hexylamine modification at the 5' terminal phosphate. Following attachment of the riboswitch aptamer to a CNT, we observed that structural rearrangements of the riboswitch resulted in three discrete smFET conductance classes in the absence of adenine (Fig. 4.4a). We analyzed the data using an adaptation of baseline correction algorithms to merge with those normally used in analysis of smFRET intensity *versus* time trajectories, and use the transition matrix to infer the rate constants [109], [171]. The lifetimes of all observed classes fell within a range of 100 µs to 10 ms (Table 4.2). Subsequent addition of adenine led to transitions between four discrete conductance classes, including an apparently new class characterized by a very short lifetime and significantly-lowered conductance (Fig. 4.4b). Titration of adenine from 30 nM

66
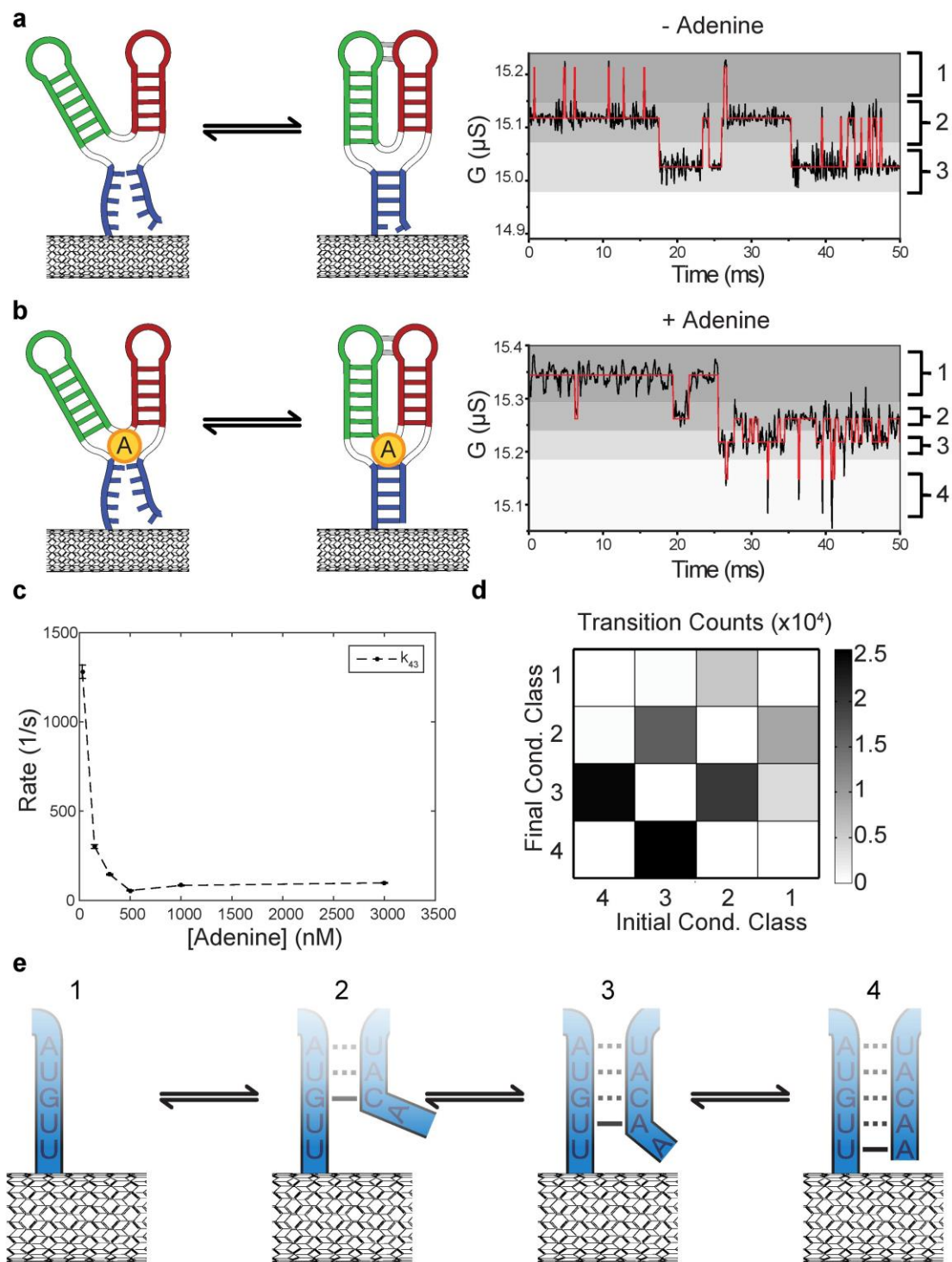
Figure 4.4. smFET conductance fluctuations following single-molecule attachment of the wild type *pbuE* riboswitch. (a),(b) Addition of adenine (3 μM) shifts the signal from a three- to a four-conductance class time-series. (c) the new conductance class continues to be stabilized by addition of adenine because the rate out of class 4, k_{43}, continues to decrease. (d) the four conductance classes only transition between adjacent classes. Counts are from the 3 μM adenine condition of the wild type aptamer. (e) a proposed model where base-pairs serially unzip beginning at the terminal pair.

to 3 µM stabilized the lowest conductance class, extending its average lifetime by 13-fold

between 30 nM and 3 µM adenine (Fig. 4.4c). This result implies that the lowest conductance

class is actively stabilized by addition of adenine.

Table 4.2. Transition rates (1/s) between three or four conductance classes (as labeled in Fig. 4.4) for the wild-type *pbuE* aptamer with varied adenine concentration as calculated using an HMM fit of smFET conductance traces. 95% confidence intervals are also reported.

[Adenine] nM	k_{12}	Δk_{12}	k_{21}	Δk_{21}	k_{23}	Δk_{23}	k_{32}	Δk_{32}	k_{34}	Δk_{34}	k_{43}	Δk_{43}
0	96.2	1.77	25.5	0.555	29.2	0.618	34.0	0.716	n/a	n/a	n/a	n/a
30	24.0	0.534	26.5	0.628	21.9	0.566	73.1	1.88	33.1	1.25	1280	37.4
150	33.7	0.829	34.9	0.659	34.7	0.661	108	2.24	33.9	1.19	302	10.5
300	50.8	1.15	37.2	0.765	27.3	0.881	85.7	1.61	26.8	1.07	145	3.88
500	40.3	0.797	38.3	0.712	17.4	0.389	36.0	0.676	10.5	0.309	55.4	1.88
1000	43.2	0.958	42.3	0.875	30.3	0.640	43.0	0.707	14.1	0.358	83.8	2.21
3000	33.1	0.831	27.6	0.648	21.1	0.542	51.4	1.08	19.5	0.615	98.2	3.41

Together with the general observation that more negative charge near the CNT surface

tends to lead to lower conductance under our experimental conditions [41]–[43], these results

led us to hypothesize that the lowest conductance class represents a fully base-paired P1 stem,

an observation consistent with the results of NMR spectra [156]. With this interpretation,

addition of adenine leads to stabilization of the fully paired conformation of the P1 stem. It is

likely that this conductance class was too short lived to be observed in the absence of adenine,

consistent with RNA secondary structure calculations using MFOLD we initiated suggesting that

the terminal base is unpaired [172]. This model is supported by competition experiments,

wherein a DNA oligomer complementary to the P1 stem was incubated with the riboswitch,

leading to transient extinction of the four conductance class signal. Upon consideration of

Debye screening, we interpret each of these conductance classes as a P1 stem structure with a

different terminally paired base proximal to the CNT in the paired state (Fig. 4.4e). If the P1

stem base pair closest to the CNT is formed, the 3' end of the phosphate backbone would not diffuse appreciably from a position near the nanotube surface, thereby increasing the average negative charge in the vicinity of the smFET and lowering device conductance. In the case where the same base pair is broken, the average position of the 3' terminal phosphate group in the RNA backbone would be located farther away from the nanotube surface, resulting in a higher device conductance. The conductance class depends only on the terminally paired base – bases above may be paired or unpaired with no consequences for conductance because the phosphate backbone adopts a similar set of conformations. In the following, we will use the notation wherein conductance classes are enumerated in order from highest to lowest and, for instance, k_{21} denotes the rate constant for transitions from the second-highest conductance class into the highest conductance class.

Further analysis of the fluctuations between the three or four conductance classes in the conductance *versus* time trajectories revealed that each conductance class predominantly transitioned to a conductance class that was adjacent in conductance (Fig. 4.4d). This kinetic pattern implies that the riboswitch aptamer P1 stem zips or unzips only at the terminal base (Fig. 4.4e). As an example, if the CNT is in conductance class 4 when the last base unpairs, but the penultimate base is already unpaired, one would observe a transition from conductance class 4 to conductance class 2. However, these off-diagonal transitions, in either direction, are extremely rare. Therefore, the P1 stem zips and unzips in sequential steps that initiate at the terminally paired base.

4.4.2 Comparison of aptamers with stabilized and destabilized P1 stems suggest that adenine binding promotes P1 helicity by destabilizing the unpaired state

Previous studies on the native *pbuE* riboswitch sequence have suggested a crucial role for the central G-C base pair of the P1 stem [149], [151], [152]. In force pulling studies by Greenleaf *et al.* and Frieda *et al.*, an observed transition state for P1 stem unfolding was located at a

69

pulling distance corresponding to the G-C base pair [151], [152]. To confirm the zipping model in the previous section, as well as to assess the role of the central G-C base pair in P1 stem stability, we performed smFET studies on two *pbuE* aptamer mutants (see Fig. 4.3). First, an aptamer with a P1 stem destabilized by a C-C mismatch in the third position, referred to as the G3C aptamer, and second, an aptamer with a P1 stem stabilized without altering the relative distance between the CNT surface and the *pbuE* aptamer structure by switching the two terminal A-U base pairs for G-C base pairs, referred to as the stable aptamer.

Both of these aptamers displayed two conductance classes, in contrast to the wild-type aptamer which displayed four (Fig. 4.5a & b). We continue to utilize the same numbering convention as above. While the wild-type, G3C, and stable aptamers all have equivalent adenine binding thermodynamics under our conditions, as monitored by a 2AP fluorescence
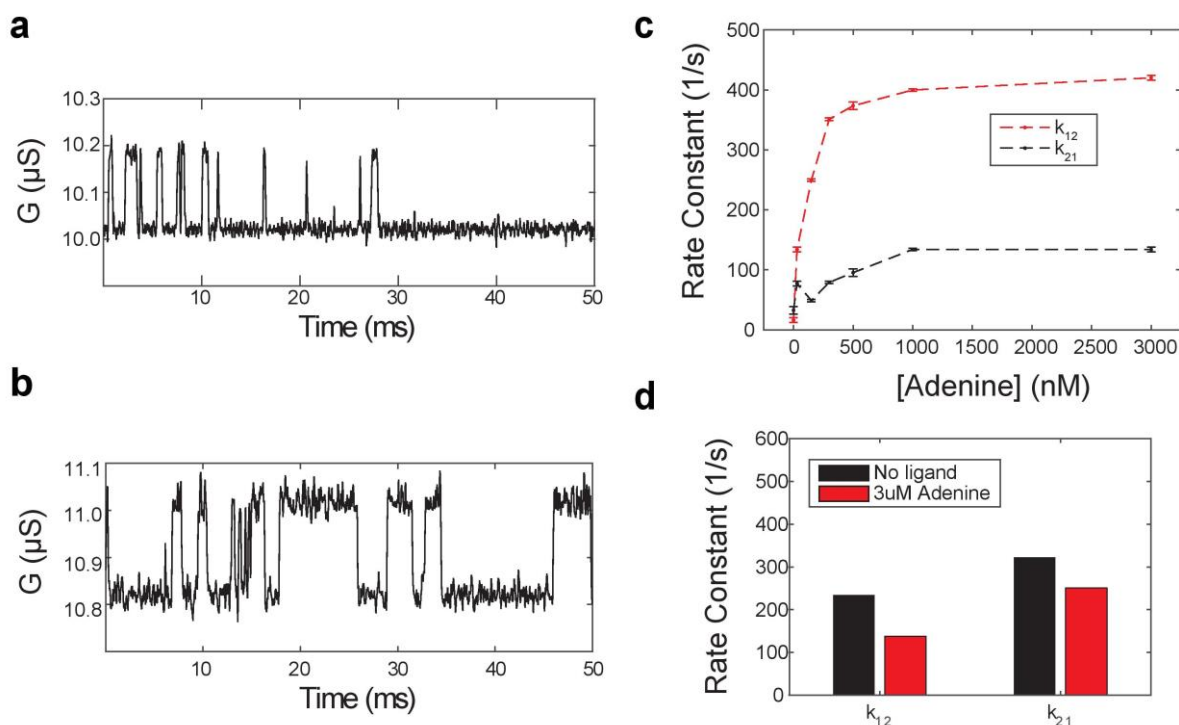
Figure 4.5. smFET conductance fluctuations in P1 stem mutants. Both the (a) G3C, and (b) stable mutant aptamers display fluctuations between two conductance classes, both shown at 3 μM adenine. While (c) the G3C aptamer has dynamics that depend strongly on the presence and concentration of adenine, (d) the stable aptamer does not have a strong adenine dependence.

binding assay (Fig. 4.6 and Table 4.3), the P1 rearrangements of the two mutants responded differently to adenine over the same range as in the wild-type, 30 nM to 3 µM. The G3C aptamer k_{12} increased with adenine concentration by a factor of 25 at saturation while the rate k_{21} increased a more modest 4-fold (Fig. 4.5c). In contrast, the dynamics of the stable aptamer were only modestly affected by the addition of adenine (Fig. 4.5d).
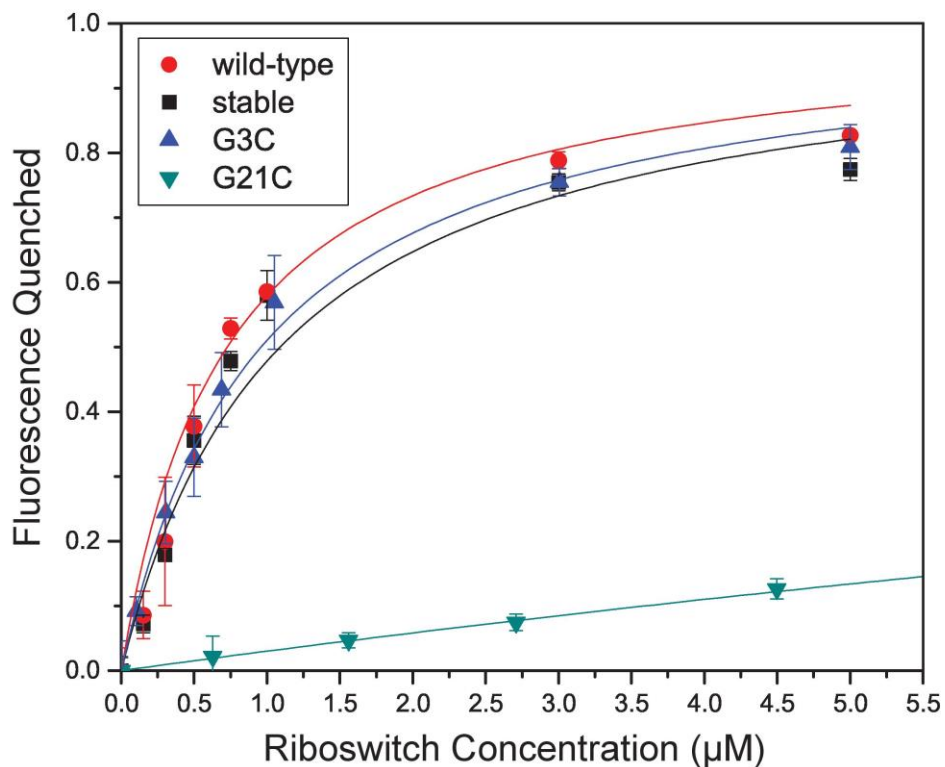
Figure 4.6. Fluorescence quenching assay of 2AP binding to *pbuE* riboswitch aptamer mutants measured with 10 mM $MgCl_2$ and 0.1x PBS at 25°C. Only the G21C mutant has a significantly reduced affinity for 2AP as compared to the wild-type aptamer.

Table 4.3. Measured K_D values for 2AP binding to the wild-type *pbuE* aptamer and mutant constructs as denoted in Figure 4.3.

Construct	K_D (nM)
Wild-type	730 ± 30.
Stable	1100 ± 100.
G3C	960 ± 30.
G21C	32400 ± 500.

For the G3C aptamer, these results are consistent with an assignment of conductance class 2 being a P1 stem conformer with the A1 and U63 paired, which is relatively stabilized by adenine binding, and conductance class 1 being a state with a predominantly unpaired P1 stem. This is because binding pocket rearrangements are in close proximity to the predominantly unpaired state of the helix and are likely to have a much more pronounced effect, rearranging the phosphate backbone to a state close to the paired state when adenine is in the bound state. On the other hand the fact that the fully paired state is weakly destabilized as adenine is added is consistent with the interpretation that the C-C mismatch tends to destabilize the helical conformation, in addition to abolishing the intermediate stacked states observed in the wild-type aptamer.

For the stable aptamer, our results are consistent with an assignment of conductance class 1 and 2 both being paired states of P1, with conductance class 2 fully paired and conductance class 1 being almost fully paired, likely with numerous missed events. Together with the results of the G3C aptamer, this interpretation explains the fact that the stable aptamer has a weak adenine dependence as well – if the structural outcome of adenine binding is to promote helicity of the P1 stem, when P1 helicity is already sufficiently stabilized by sequence composition, then adenine binding has no effect. This result is consistent with the observation that P1 helicity and adenine binding can be antagonistic – if the helicity established by elongating the P1 stem is not the same enforced by the binding pocket, then the stem can outcompete binding [156]. Taken together, the results of these mutagenesis studies support the hypothesis that our smFET signal reports directly on rearrangements of the P1 stem and that adenine binding mainly promotes the fully paired P1 stem by destabilizing the unpaired state. Importantly, comparison of the adenine dependence of the G3C aptamer in our smFET assay with its 2AP dependence in a fluorescence ligand binding assay (see Fig. 4.6) suggest that the binding pocket plays a direct role in stabilizing the paired conformation of the P1 stem, but under our conditions, disruption of P1 stem rearrangements has little to no effect on the binding pocket.

4.4.3 Second-scale dynamic heterogeneity of the P1 stem depends upon distal tertiary rearrangements

Structures of purine family riboswitches[148], [161], [162], as well as NMR characterizations of solution conformations[163]–[165] have established that the conserved base pairs between the tandem guanine nucleotides (nts) in L2 (G21 and G22) and the tandem cytosine nts in L3 (C44 and C45) form a tertiary interaction to complete the folded conformation of the riboswitch. smFRET studies of both adenine and guanine sensing riboswitches have revealed that this interaction possesses a lifetime on the order of seconds [150], [166], and the folded conformation is stabilized by the presence of ligand [156], [163], [166]. Formation of this tertiary contact by necessity greatly restricts the available conformations of J2/3, the three-way junction element between P2 and P3, which caps the P1 stem [161], [163]. Therefore, we reasoned that, having observed that adenine-dependent rearrangements of the *pbuE* aptamer modulate the dynamics of the P1 stem (Fig. 4.4c and Fig. 4.5c), the L2-L3 tertiary stabilization may be directly correlated with zipping and unzipping of the P1 stem. Therefore, we performed smFET studies on a *pbuE* aptamer mutant with a destabilized L2-L3 tertiary interaction, which we refer to as the G21C aptamer [150] (Fig. 4.3), varying the concentration of adenine between 50 nM and 50 µM.

Like the wild-type aptamer, this mutant displayed four conductance classes in the presence of adenine. The G21C construct, however, spends a much greater proportion of its time in conductance class 1, the class with a fully unfolded P1 stem. Broadly speaking, therefore, the L2-L3 interaction is thermodynamically coupled to the adenine-dependent rearrangement driving P1 stem helicity outlined in the previous section. Next, we investigated how the kinetic details of the P1 rearrangements in the two aptamers revealed the precise effect of tertiary structure formation on P1 stem secondary structure.

Aside from possessing four conductance classes, both the wild-type and G21C aptamers possess a significant degree of second-scale dynamic heterogeneity – in other words, it cannot

be explained by a single transition matrix. To shed light on this observation, we analyzed the adenine titration data of both the wild-type and G21C aptamers with a hierarchical hidden Markov model and found that the best model for the heterogeneity in both datasets was a set of two interconverting kinetic states, each of which can access all four conductance classes (Fig. 4.7a & b). Because only three conductance classes were observed in the absence of adenine (Fig. 4.4a), only conductance *versus* time trajectories recorded when adenine was present were compared. For both, two interconverting kinetic states constitute the minimal model; initializing with three interconverting populations results in two with significant density, corresponding to the two-population model, and a third that is not populated. Because these two kinetic states conceptually are two interconverting types of P1 stem, we refer to these populations as P1^{A,wt} and P1^{B,wt}, and as P1^{A,G21C} and P1^{B,G21C} for the wild-type and G21C aptamers, respectively. In order to compare the kinetic states present in the wild-type and G21C time series, we first calculate, for each conductance class in each kinetic state:

$$\Delta G_i^A = ln \frac{k_{i,i+1}^A}{k_{i+1,i}^A}$$

$$\Delta G_i^B = ln \frac{k_{i,i+1}^B}{k_{i+1,i}^B}$$

which is the thermodynamic partition between entering conductance class *i* from a conductance class *i+1* within P1^A *versus* the reverse rate from conductance class *i+1* back to conductance class *i.* This corresponds to the probability of zipping rather than unzipping. On comparison, shown in Figure 4.7c & d, we identify P1^{A,wt} with P1^{A,G21C}, and P1^{B,wt} with P1^{B,G21C} (hereafter referred to simply as P1^A and P1^B wherever possible).

Thus, our analysis reveals two separate P1 stem conformations with two distinct stabilized intermediates – P1^A, which predominantly populates the intermediately unpaired state in conductance classes 1 and 2, and P1^B, which predominantly populates the intermediately unpaired state in conductance class 3, near the fully folded state (conductance class 4). The
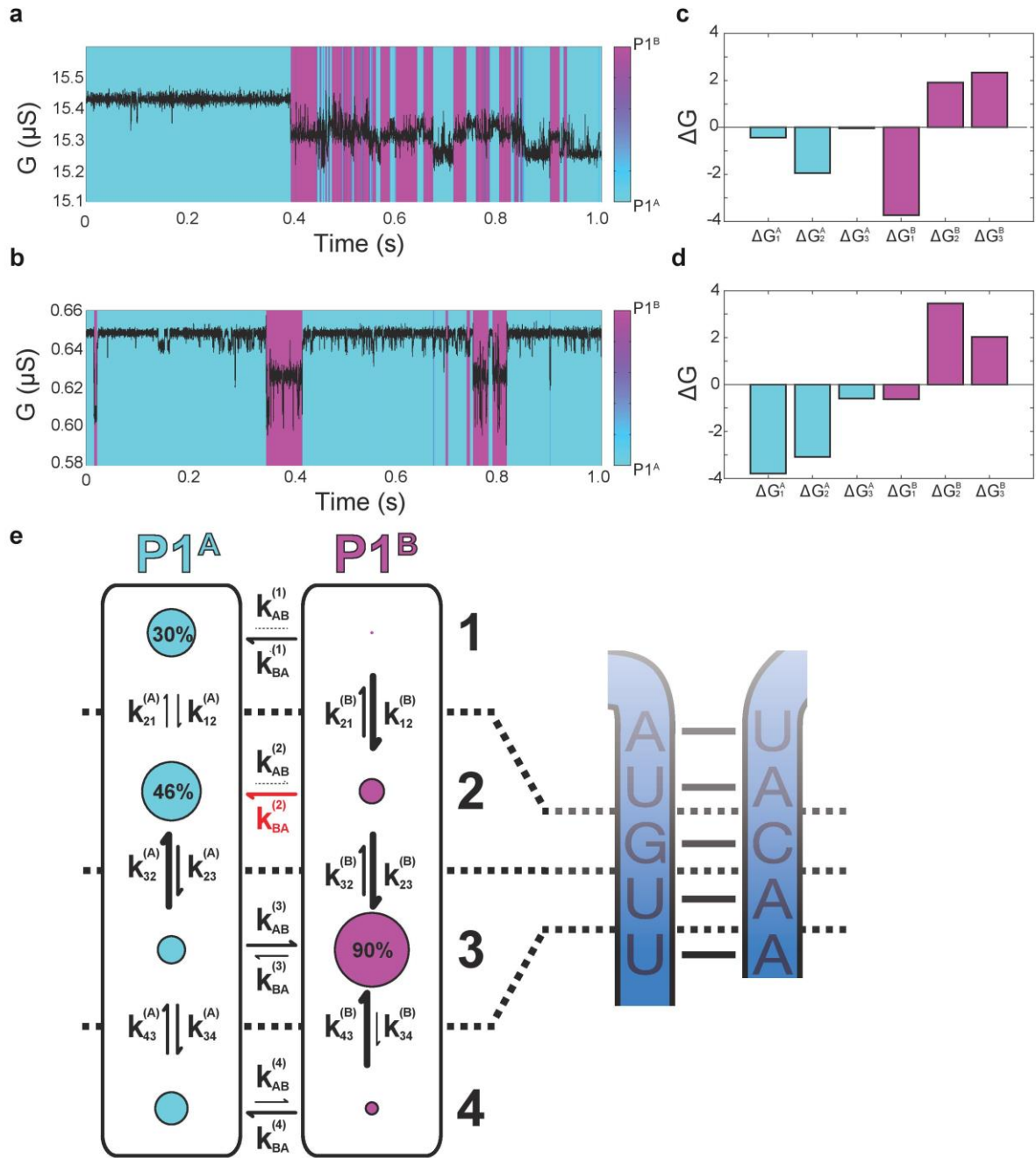
Figure 4.7. Dynamic heterogeneity of the wild-type and G21C constructs. a, P1^{A,wt} (cyan) and P1^{B,wt} (magenta), as discussed in the text, of the wild-type construct in 3 µM adenine. b, P1^{A,G21C} (cyan) and P1^{B,G21C} (magenta) for the G21C construct in 3 µM adenine. c, ΔG pattern of P1^{A,wt} (cyan) and P1^{B,wt} (magenta). d, ΔG pattern of P1^{A,G21C} (cyan) and P1^{B,G21C} (magenta). e, Kinetic model for the wild-type P1 stem. Arrows strength denotes the comparative rate constant. All numbers and arrows are drawn for the 3 µM adenine condition of the wild-type aptamer. Numbers next to the conductance class designations are the occupancy numbers normalized to the occupancy of each kinetic state, P1^A or P1^B. The cartoon to the right depicts our proposed designations for each conductance class – for example, in conductance class 3, we propose that every base is paired up until U2-A62.

rate constants for each transition type are schematized at saturating adenine for the wild-type aptamer in Figure 4.7e. Compared to the P1^{B,wt}, the intermediate in P1^{B,G21C} is relatively less stable, as with this mutation the aptamer more easily transitions directly into conductance class 1 with a 9-fold reduced reverse rate, from 6500 ±300 s^{-1} to 700 ±200 s^{-1}. Next, we examined transitions between P1^A and P1^B. We first note that, while the overall partition of the G21C aptamer conductance *versus* time trajectory between P1^A and P1^B does not change as the concentration of adenine is increased, for the wild-type aptamer the occupancy of P1^B increases as the concentration of adenine is raised, from 10% at 30nM adenine to ~40% at 3 μM adenine. This is primarily driven by a 3-fold decrease in the rate of transition from P1^B into P1^A *via* conductance class 2, from 370 ±10 s^{-1} to 144 ±6 s^{-1} indicating that addition of adenine raises the free energy barrier between P1^B and P1^A. As discussed below, this latter rate is now commensurate with the rate of transcription [173]–[175]. Together, these kinetic results imply that the L2-L3 interaction has two major effects: first, it prevents P1^B from entering the predominantly unpaired state (conductance class 1), and second, it prevents P1^B from entering P1^A any faster than the transcription rate.

4.5 Discussion

Our investigation has focused entirely on the role of RNA rearrangements in transient base pair formation. We find that the P1 stem of the *pbuE* riboswitch aptamer is highly dynamic even in the presence of adenine, a result that is loosely consistent with Nozinivic *et al.* [156]. However, we suspect, as others have, that this highly dynamic kinetic pattern characterizes all nucleic acid structures [176]–[178]. According to NMR results, the lifetime of an unpaired base, while highly sequence dependent, is on the order of 1-100 ms [157], [159], [160]. Furthermore, from studies of the zipping of hairpins, the rate at which bases transition from the paired to the unpaired once that motion has begun, and *vice versa*, is on the order of hundreds of

nanoseconds [176], [177], [179], [180], in loose agreement with our observation of instantaneous transitions even at 50 µs time resolution. These two features of pairing and unpairing dynamics lead to a highly complex ensemble of possible and constantly interconverting paired configurations – a hairpin consisting of just 10 base pairs has over 1500 unique configurations [177]. It is notable, therefore, that under our conditions, the P1 stem only accesses two pathways for discrete and sequential zipping and unzipping, P1^A and P1^B.

The wild-type P1 stem showed fluctuations between four conductance classes, which we interpreted, based on structural and Debye length arguments, in terms of the last base in the stem to be paired. On the other hand, the G3C aptamer, in particular, only displayed fluctuations between two conductance classes – this is likely because a folding nucleus for a helix consists of at least two base pairs. Furthermore, there is a net free energy loss from pairing a single base due to entropic effects, which are not offset by favorable hydrogen bonding between two complementary bases, as this is the same interaction they could make with water [81], [176], [177], [181]. However, in a helix with many pairs, base stacking mitigates these entropic effects. Therefore, our data are consistent with a model wherein the G3C aptamer only has apparent transitions between its two folding nuclei.

Examination of the kinetics of the interconversion between these two nuclei, as well as comparison with the kinetics of interconversion between paired states of the stable aptamer, revealed that the effect of adenine binding is transduced *via* element close to the predominantly unpaired state of the P1 stem, and that the effect of this stabilization dissipates further down the helix. Furthermore, while highly dynamic, we find that the pathway of unzipping and rezipping of the P1 stem is discrete and sequential. Despite the large ensemble of possible configurations we find that, within the limits our time-resolution, zipping or unzipping the wild-type P1 stem occurs one base at a time, the former beginning at the bases closest to the binding pocket and the latter beginning at the terminus of the aptamer. In concert with theoretical studies, this observation underscores the importance of three-way junctions in secondary structure stability

[178], [182]. Together with the adenine dependence of P1 stability in the wild-type as well as the adenine-destabilizing effect on the unzipped form in the G3C aptamer, we supply evidence that this pathway is a highly tuned by interactions with the binding pocket. That is, we hypothesize that, due to its structural proximity and participation in adenine binding [148], [161], [162], rearrangements in J2/3 lead to sequential zipping or unzipping of the P1 stem. On the other hand, our results also suggest that, under our conditions, the stability of P1 stem plays little or no role in the thermodynamics of adenine binding (see Fig. 4.6).

Invasion of the aptamer by the expression platform is under kinetic control, and the lifetime of the unzipped state of the P1 stem presents a first-passage chance for operation of the switch, the result of which is an intrinsically non-equilibrium process [149], [154], [155], [183], [184]. In the wild-type aptamer, our data suggest two ways in which the invasion by the expression platform is modulated. First, enhanced occupancy of $P1^B$ in its stabilized intermediate, conductance class 3, indirectly increases the occupancy of the fully folded P1 stem (Fig. 4.4c). We assert that in this configuration the expression platform cannot invade the P1 stem because it cannot interact with any bases in the helix. Second, assuming an invasion has begun at the first base pair of the P1 stem, while the aptamer will unfold if it is in $P1^A$, our model suggests that if the aptamer is in $P1^B$ it will unfold up until the third base, i.e. the G-C base pair. Indeed, this picture is consistent with the dramatic consequences of the removal of this base pair, as well as identification of the G-C base pair as the location of the unfolding transition state on the pulling coordinate [151] (Fig. 4.4b *versus* Fig. 4.5a). If adenine concentrations are low, transitions between $P1^B$ and $P1^A$ are significantly faster, ~370 s^{-1}, than the rate of transcription of the antiterminator, ~10-90 nt/s [173]–[175] for *E. coli* and perhaps faster for *B. subtilis* [185], though ~10 nt, or an RNAP footprint [186], [187] must be transcribed for RNAP to escape, an argument introduced in this context by Wickiser *et al.* [149]. As the reverse rate back into $P1^B$ is slow, ~25 s^{-1}, the aptamer enters $P1^A$ and continues to unfold. However, if adenine concentrations are high, transitions between $P1^B$ and $P1^A$, ~140 s^{-1}, are competitive with the rate

of transcription, and the refolding rate is very high – the aptamer resists invasion. Our data show that this barrier is significantly smaller in the absence of a stable L2-L3 tertiary interaction, suggesting that population and stabilization of P1^B is a primary consequence. These data suggest the existence of a dynamic correlation between L2-L3 dynamics [150], [166] and the base pair level dynamics of the P1 stem, over a distance of 32 Angstroms. This picture is supported by the observation that, in crystal structures of purine riboswitches [148], [161], [162], the junction element J2/3 caps the P1 stem, and further, that NMR studies have revealed that this junction element is disordered in the absence of adenine [163]–[165]. Together with these observations, our data suggest that opening and closing of the ligand-enclosing flap, a motion that is strongly influenced by the tertiary interaction between L2 and L3, reduces the probability of transition from P1^B to P1^A, and P1^B is inefficiently unzipped.

To augment our understanding of this dynamic correlation between tertiary structure formation and base-pair level zipping and unzipping of the P1 stem, we compare our results to the pattern of conservation of purine riboswitches. In general, the P2 and P3 stems are conserved in the sense that they remain paired regions of a certain length, but their precise sequences are variable (RF00167) [188]. L2 and L3 have a conserved length as well as conserved G-C linchpins, which come together to form the fully folded form of the riboswitch. The binding pocket element J2/3 is almost universally conserved, as are the two A-U base pairs of the P1 stem closest to the pocket, which terminates with an A-minor interaction between P2 and P3. The third base pair of the P1 stem, G-C in the case of the *pbuE* aptamer, (Fig. 4.3) is not conserved: it varies between an A-U and a G-C. Examining these results in more detail, we notice that if the P1 stem contains an AUG, the U of which base pairs with an A in the third (Fig. 4.3) position, its sequence always contains an additional four bases (two A-U pairs and two G-C pairs). On the basis of our results we propose that the purine riboswitch family has at least two classes of P1 stems – those that begin zipping and unzipping at the AU-UA pair in position 5 (Fig. 4.3), and those that begin zipping and unzipping at the AUG three bases down but contain

four extra bases in the P1 stem. While the *pbuE* riboswitch falls into the former class, the guanine-sensing *xpt* riboswitch is an example of the latter class. smFRET and single-molecule force pulling studies have revealed that the *pbuE* riboswitch does not fully fold in the absence of adenine [150], [151], whereas NMR studies of the *xpt* riboswitch have revealed that the riboswitch is close to its bound state even in the absence of adenine [164], [165]. We propose that these two families have differing designs of P1 stem in order to transfer metastability from the tertiary structure formation of L2-L3 to the secondary structure of the P1 stem. Furthermore, from comparison of the heterogeneity in wild-type sequences with sequences that cannot form stable L2-L3 interactions, we conjecture that the L2-L3 interaction exists on one side of a dynamic network whose consequence is zipping of the P1 stem.

4.6 Conclusions

There are three main classes of highly resolved studies of purine family riboswitch folding – those that focus on formation and deformation of highly structured pockets on a pulling coordinate [151], [152], those that examine equilibrium-scale rearrangements of the tertiary structure [150], [166], and those that examine the evolution of the average structure massive numbers of molecules [163]. Our methods utilizing single-molecule field effect transistors contrast from all of these, as we are able to provide a label-free high time-resolution single-molecule measurement of the *pbuE* riboswitch aptamer using its natural sequence without continuous perturbation. Previous studies have provided crucial information as to the organization of the relative structural elements of the switch, as well as the order in which they fold and the likely slow-timescale rearrangements that accompany ligand binding. In this work we present the first wide-bandwidth single-molecule measurements of base-pair level stability of the P1 stem. We find that zipping and unzipping of the stem is linear, sequential, and dependent on the presence of specific base pairs in the organization of the stem. Finally, we find that these

rearrangements are heterogeneous on the second timescale yet occur on the microsecond to millisecond timescale, making measurements from smFETs essential in order to describe the potential ensemble of unzipping pathways.

In future studies, smFETs could be used to probe the magnesium (Mg^{2+}) dependence of folding, as well as to study rearrangements of each portion of the riboswitch relative to every other. For instance, *xpt* riboswitches include a rearrangement between the P1 and P2 stems that cannot be detected using the 5' terminal tethering presented here [166]. However, the rate constants of this process have a very strong dependence on the concentration of Mg^{2+} ions, which quickly exit the observable time-resolution of most single-molecule methods. We expect that the smFET experimental platform can be applied to such situations, as well as, in general, systems with local charge fluctuations that have a wide mixture of time-scales.

Chapter 5

Outlook on smFET Technology

The work presented in this dissertation has increased the body of smFET literature. The development of a novel functionalization method using nanowell-confined chemistry allows for more reliable point defect generation and a more durable functional handle for biomolecule tethering. DNA hybridization experiments suggest a possible smFET-induced shift in hybridization dynamics that may be caused by an induced gradient of charged species near the CNT surface. This effect should be further investigated by performing DNA hybridization measurements in a variety of buffer concentrations and using different gate biases. Further G-quadruplex studies should focus on obtaining a cation titration series as well as sequence variation to further probe the two-state smFET signal generated. A notable achievement of this work is the first single-molecule evidence of RNA zipping and unzipping one base at a time. However, the complexity of the riboswitch aptamer data suggests that a better understanding of intramolecular RNA dynamics would be a useful contribution to the smFET field. A systematic study of RNA hairpin dynamics could be directly compared to single-molecule literature to confirm the validity of these studies. smFET provides a unique vantage point for single-molecule biophysical studies primarily due to its wide bandwidth. As more complex systems with a smaller existing body of literature are probed, a complete picture of the signal transduction mechanism and evaluation of the invasiveness of the technique will become necessary. This may require adopting novel device configurations, such as CMOS-integrated smFETs which can perform measurements at 1 MHz, or potentially passivated or suspended CNTs to reduce noise.

References

[1]   E. Neher and B. Sakmann, "Single-channel currents recorded from membrane of denervated frog muscle fibres.," *Nature*, vol. 260, no. 5554, pp. 799–802, 1976.

[2]   O. P. Hamill, A. Marty, E. Neher, B. Sakmann, and F. J. Sigworth, "Improved patch-clamp techniques for high-resolution current recording from cells and cell-free membrane patches," *Eur. J. Physiol.*, vol. 391, no. 2, pp. 85–100, 1981.

[3]   S. C. Blanchard, R. L. Gonzalez, H. D. Kim, S. Chu, and J. D. Puglisi, "tRNA selection and kinetic proofreading in translation.," *Nat. Struct. Mol. Biol.*, vol. 11, no. 10, pp. 1008–1014, 2004.

[4]   I. Tinoco and R. L. Gonzalez, "Biological mechanisms , one molecule at a time," pp. 1205–1231, 2011.

[5]   X. S. Xie, "Single molecule approach to enzymology," *Single Mol*, vol. 2, pp. 229–236, 2001.

[6]   A. N. Kapanidis and T. Strick, "Biology, one molecule at a time," *Trends Biochem. Sci.*, vol. 34, no. 5, pp. 234–243, 2009.

[7]   R. Rigler, Ü. . Mets, J. Widengren, and P. Kask, "Fluorescence correlation spectroscopy with high count rate and low background: analysis of translational diffusion," *Eur. Biophys. J.*, vol. 22, no. 3, pp. 169–175, 1993.

[8]   T. Förster, "Energiewanderung und Fluoreszenz," *Naturwissenschaften*, vol. 33, no. 6, pp. 166–175, 1946.

[9]   L. Stryer and R. P. Haugland, "Energy transfer: a spectroscopic ruler.," *Proc. Natl. Acad. Sci. U. S. A.*, vol. 58, no. 2, pp. 719–726, 1967.

[10]   T. Ha, T. Enderle, D. F. Ogletree, D. S. Chemla, P. R. Selvin, and S. Weiss, "Probing the interaction between two single molecules: fluorescence resonance energy transfer between a single donor and a single acceptor.," *Proc. Natl. Acad. Sci.*, vol. 93, no. 13, pp. 6264–6268, 1996.

[11]   T. Ha, X. Zhuang, H. D. Kim, J. W. Orr, J. R. Williamson, and S. Chu, "Ligand-induced conformational changes observed in single RNA molecules.," *Proc. Natl. Acad. Sci. U. S. A.*, vol. 96 VN-r, no. 16, pp. 9077–9082, 1999.

[12]   S. a McKinney, A.-C. Déclais, D. M. J. Lilley, and T. Ha, "Structural dynamics of individual Holliday junctions.," *Nat. Struct. Biol.*, vol. 10, no. 2, pp. 93–97, 2003.

[13]   X. Zhuang *et al.*, "A Single-Molecule Study of {RNA} Catalysis and Folding," *Science (80-.).*, vol. 288, no. June, pp. 2048–2051, 2000.

[14]   E. Betzig *et al.*, "Imaging intracellular fluorescent proteins at nanometer resolution.," *Science*, vol. 313, no. 2006, pp. 1642–1645, 2006.

[15]   M. J. Rust, M. Bates, and X. W. Zhuang, "Sub-diffraction-limit imaging by stochastic optical reconstruction microscopy (STORM)," *Nat Methods*, vol. 3, no. 10, pp. 793–795,

2006.

[16]   A. Yildiz, "Myosin V Walks Hand-Over-Hand: Single Fluorophore Imaging with 1.5-nm Localization," *Science (80-.).*, vol. 300, no. 5628, pp. 2061–2065, 2003.

[17]   L. S. Churchman, Z. Okten, R. S. Rock, J. F. Dawson, and J. A. Spudich, "Single molecule high-resolution colocalization of Cy3 and Cy5 attached to macromolecules measures intramolecular distances through time.," *Proc. Natl. Acad. Sci. U. S. A.*, vol. 102, no. 5, pp. 1419–23, 2005.

[18]   J. Elf, G.-W. Li, and X. S. Xie, "Probing transcription factor dynamics at the single-molecule level in a living cell.," *Science*, vol. 316, no. 5828, pp. 1191–4, 2007.

[19]   S. Nie, D. T. Chiu, and R. N. Zare, "Probing individual molecules with confocal fluorescence microscopy.," *Science*, vol. 266, no. 5187, pp. 1018–21, 1994.

[20]   D. Axelrod, "Total internal reflection fluorescence microscopy in cell biology," *Traffic*, vol. 2, no. 11, pp. 764–774, 2001.

[21]   P. Zhu and H. G. Craighead, "Zero-Mode Waveguides for Single-Molecule Analysis," *Annu. Rev. Biophys.*, vol. 41, no. 1, pp. 269–293, 2012.

[22]   C. D. Kinz-Thompson and R. L. Gonzalez, "SmFRET studies of the 'encounter' complexes and subsequent intermediate states that regulate the selectivity of ligand binding," *FEBS Lett.*, vol. 588, no. 19, pp. 3526–3538, 2014.

[23]   T. Ha and P. Tinnefeld, "Photophysics of Fluorescent Probes for Single-Molecule Biophysics and Super-Resolution Imaging," *Annu. Rev. Phys. Chem.*, vol. 63, no. 1, pp. 595–617, 2012.

[24]   M. Egger *et al.*, "Wet lipid-protein membranes imaged at submolecular resolution by atomic force microscopy," *J. Struct. Biol.*, vol. 103, no. 1, pp. 89–94, 1990.

[25]   H. Li, S. H. Park, J. H. Reif, T. H. LaBean, and H. Yan, "DNA-Templated Self-Assembly of Protein and Nanoparticle Linear Arrays," *J. Am. Chem. Soc.*, vol. 126, no. 2, pp. 418–419, 2004.

[26]   M. Grandbois, M. Beyer, M. Rief, H. Clausen-Schaumann, and H. E. Gaub, "How Strong is a Covalent Bond?," *Science (80-.).*, vol. 283, no. March, pp. 1727–1730, 1999.

[27]   M. Rief, M. Gautel, F. Oesterhelt, J. M. Fernandez, and H. E. Gaub, "Reversible Unfolgind of Individual Titin Immunoglobulin Domains by AFM," *Science (80-.).*, vol. 276, pp. 1109–1112, 1997.

[28]   G. U. Lee, L. a Chrisey, and R. J. Colton, "Direct Measurement of the Forces Between Complementary Strands of Dna," *Science (80-.).*, vol. 266, no. 5186, pp. 771–773, 1994.

[29]   N. Crampton *et al.*, "Fast-scan atomic force microscopy reveals that the type III restriction enzyme EcoP15I is capable of DNA translocation and looping.," *Proc. Natl. Acad. Sci. U. S. A.*, vol. 104, no. 31, pp. 12755–12760, 2007.

[30]   Keir C. Neuman and A. Nagy, "Single-molecule force spectroscopy: optical tweezers, magnetic tweezers and atomic force microscopy," *Nat Method*, vol. 5, no. 6, pp. 491–505, 2008.

[31] A. Ashkin, J. M. Dziedzic, J. E. Bjorkholm, and S. Chu, "Observation of a single-beam gradient force optical trap for dielectric particles.," *Opt. Lett.*, vol. 11, no. 5, p. 288, 1986.

[32] M. J. Schnitzer and S. M. Block, "Kinesin hydrolyses one ATP per 8-nm step.," *Nature*, vol. 388, no. 6640, pp. 386–90, 1997.

[33] G. J. Wuite, S. B. Smith, M. Young, D. Keller, and C. Bustamante, "Single-molecule studies of the effect of template tension on T7 DNA polymerase activity.," *Nature*, vol. 404, no. 6773, pp. 103–106, 2000.

[34] J. Liphardt, B. Onoa, S. B. Smith, I. Tinoco, and C. Bustamante, "Reversible unfolding of single RNA molecules by mechanical force.," *Science*, vol. 292, no. 5517, pp. 733–7, 2001.

[35] E. A. Abbondanzieri, W. J. Greenleaf, J. W. Shaevitz, R. Landick, and S. M. Block, "Direct observation of base-pair stepping by RNA polymerase.," *Nature*, vol. 438, no. 7067, pp. 460–5, 2005.

[36] T. R. Strick, V. Croquette, and D. Bensimon, "Single-molecule analysis of DNA uncoiling by a type II topoisomerase.," *Nature*, vol. 404, no. 6780, pp. 901–904, 2000.

[37] J. E. Curtis, B. A. Koss, and D. G. Grier, "Dynamic holographic optical tweezers," *Opt. Commun.*, vol. 207, no. 1–6, pp. 169–175, 2002.

[38] R. Berkovich, S. Garcia-Manyes, J. Klafter, M. Urbakh, and J. M. Fernandez, "Hopping around an entropic barrier created by force," *Biochem. Biophys. Res. Commun.*, vol. 403, no. 1, pp. 133–137, 2010.

[39] J. K. Rosenstein, S. G. Lemay, and K. L. Shepard, "Single-molecule bioelectronics," *Wiley Interdiscip. Rev. Nanomedicine Nanobiotechnology*, vol. 7, no. 4, pp. 475–493, 2015.

[40] S. B. Warren, S. Vernick, E. Romano, and K. L. Shepard, "Complementary Metal-Oxide-Semiconductor Integrated Carbon Nanotube Arrays: Toward Wide-Bandwidth Single-Molecule Sensing Systems," *Nano Lett.*, vol. 16, pp. 2674–2678, 2016.

[41] S. Sorgenfrei *et al.*, "Label-free single-molecule detection of DNA-hybridization kinetics with a carbon nanotube field-effect transistor," *Nat Nanotechnol*, vol. 6, no. 2, pp. 126–132, 2011.

[42] S. Sorgenfrei, C. Chiu, M. Johnston, C. Nuckolls, and K. L. Shepard, "Debye Screening in Single-Molecule Carbon Nanotube Field-Effect Sensors," pp. 3739–3743, 2011.

[43] D. Bouilly *et al.*, "Single-Molecule Reaction Chemistry in Patterned Nanowells," *Nano Lett.*, vol. 16, no. 7, pp. 4679–4685, Jun. 2016.

[44] Y. Choi *et al.*, "Single-Molecule Lysozyme Dynamics Monitored by an Electronic Circuit," *Science (80-.).*, vol. 335, no. 6066, pp. 319–324, 2012.

[45] Y. Choi *et al.*, "Single-molecule dynamics of lysozyme processing distinguishes linear and cross-linked peptidoglycan substrates," *J. Am. Chem. Soc.*, vol. 134, no. 4, pp. 2032–2035, 2012.

[46] T. J. Olsen *et al.*, "Electronic measurements of single-molecule processing by DNA

polymerase i (Klenow fragment)," *J. Am. Chem. Soc.*, vol. 135, no. 21, pp. 7855–7860, 2013.

[47]   R. H. Baughman, A. a Zakhidov, and W. a de Heer, "Carbon nanotubes --- the route toward applications," *Science (80-.).*, vol. 297, no. 5582, pp. 787–92, 2002.

[48]   E. J. Garcia, B. L. Wardle, and A. John Hart, "Joining prepreg composite interfaces with aligned carbon nanotubes," *Compos. Part A Appl. Sci. Manuf.*, vol. 39, no. 6, pp. 1065–1070, 2008.

[49]   B. Gong and Z. Shao, "Self-assembling organic nanotubes with precisely defined, sub-nanometer pores: Formation and mass transport characteristics," *Acc. Chem. Res.*, vol. 46, no. 12, pp. 2856–2866, 2013.

[50]   P. Avouris, Z. Chen, and V. Perebeinos, "Carbon-based electronics.," *Nat. Nanotechnol.*, vol. 2, no. 10, pp. 605–15, 2007.

[51]   Y. Liu, X. Dong, and P. Chen, "Biological and chemical sensors based on graphene materials," *Chem Soc Rev*, vol. 41, no. 6, pp. 2283–2307, 2012.

[52]   K. Cho, X. Wang, S. Nie, Z. Chen, and D. M. Shin, "Therapeutic nanoparticles for drug delivery in cancer," *Clin. Cancer Res.*, vol. 14, no. 5, pp. 1310–1316, 2008.

[53]   M. Miao, "Yarn spun from carbon nanotube forests: Production, structure, properties and applications," *Particuology*, vol. 11, no. 4, pp. 378–393, 2013.

[54]   D. Tasis, N. Tagmatarchis, A. Bianco, and M. Prato, "Chemistry of carbon nanotubes," *Chem. Rev.*, vol. 106, no. 3, pp. 1105–1136, 2006.

[55]   M. S. Dresselhaus, G. Dresselhaus, and P. C. Eklund, *Science of Fullerenes and Carbon Nanotubes*. New York, NY: Academic Press, 1996.

[56]   M. S. Dresselhaus, G. Dresselhaus, R. Saito, and A. Jorio, "Raman spectroscopy of carbon nanotubes," *Phys. Rep.*, vol. 409, no. 2, p. 47, 2005.

[57]   M. C. Hersam, "Progress towards monodisperse single-walled carbon nanotubes.," *Nat. Nanotechnol.*, vol. 3, no. 7, pp. 387–394, 2008.

[58]   L. Guan, K. Suenaga, and S. Iijima, "Smallest carbon nanotube assigned with atomic resolution accuracy," *Nano Lett.*, vol. 8, no. 2, pp. 459–462, 2008.

[59]   R. Zhang, Y. Zhang, Q. Zhang, H. Xie, W. Qian, and F. Wei, "Growth of half-meter long carbon nanotubes based on Shulz-Flory distribution," *ACS Nano*, vol. 7, no. 7, pp. 6156–6161, 2013.

[60]   H. Wang, Y. Yuan, L. Wei, K. Goh, D. Yu, and Y. Chen, "Catalysts for chirality selective synthesis of single-walled carbon nanotubes," *Carbon N. Y.*, vol. 81, no. 1, pp. 1–19, 2015.

[61]   D. Sun *et al.*, "Flexible high-performance carbon nanotube integrated circuits," *Nat. Nanotechnol.*, vol. 6, no. 3, pp. 156–161, 2011.

[62]   S. Tans, A. Verschueren, and C. Dekker, "Room-temperature transistor based on a single carbon nanotube," *Nature*, vol. 672, no. 1989, pp. 669–672, 1998.

[63]   D. Jariwala, V. K. Sangwan, L. J. Lauhon, T. J. Marks, and M. C. Hersam, "Carbon nanomaterials for electronics, optoelectronics, photovoltaics, and sensing.," *Chem. Soc. Rev.*, vol. 42, pp. 2824–60, 2013.

[64]   K. Besteman, J. O. Lee, F. G. M. Wiertz, H. A. Heering, and C. Dekker, "Enzyme-coated carbon nanotubes as single-molecule biosensors," *Nano Lett.*, vol. 3, no. 6, pp. 727–730, 2003.

[65]   A. Star, E. Tu, J. Niemann, J.-C. P. Gabriel, C. S. Joiner, and C. Valcke, "Label-free detection of DNA hybridization using carbon nanotube network field-effect transistors," *Proc. Natl. Acad. Sci.*, vol. 103, no. 4, pp. 921–926, 2006.

[66]   D. a Heller *et al.*, "Peptide secondary structure modulates single-walled carbon nanotube fluorescence as a chaperone sensor for nitroaromatics.," *Proc. Natl. Acad. Sci. U. S. A.*, vol. 108, no. 21, pp. 8544–8549, 2011.

[67]   F. Schwierz, "Graphene transistors.," *Nat. Nanotechnol.*, vol. 5, no. July, p. 487, 2010.

[68]   R. Martel *et al.*, "Ambipolar Electrical Transport in Semiconducting Single-Wall Carbon Nanotubes," *Phys. Rev. Lett.*, vol. 87, no. 25, p. 256805, 2001.

[69]   Z. Chen, J. Appenzeller, J. Knoch, Y. Lin, and P. Avouris, "The Role of Metal / Nanotube Contact in the Performance of Carbon Nanotube Field-Effect Transistors," *Nano Lett.*, vol. 5, no. 7, pp. 1497–1502, 2005.

[70]   P. G. Collins, M. S. Fuhrer, A. Zettl, P. G. Collins, M. S. Fuhrer, and A. Zettl, "1/F Noise in Carbon Nanotubes," *Appl. Phys. Lett.*, vol. 76, no. 2000, pp. 894–896, 2000.

[71]   J. Tersoff, "Low-frequency noise in nanoscale ballistic transistors," *Nano Lett.*, vol. 7, no. 1, pp. 194–198, 2007.

[72]   G. J. Zhang *et al.*, "DNA sensing by silicon nanowire: Charge layer distance dependence," *Nano Lett.*, vol. 8, no. 4, pp. 1066–1070, 2008.

[73]   E. Stern, R. Wagner, F. J. Sigworth, R. Breaker, T. M. Fahmy, and M. A. Reed, "Importance of the debye screening length on nanowire field effect transistor sensors," *Nano Lett.*, vol. 7, no. 11, pp. 3405–3409, 2007.

[74]   D. C. Grahame, "The electrical double layer and the theory of electrocapillarity.," *Chem. Rev.*, pp. 441–501, 1947.

[75]   J. Watson and F. Crick, "Molecular structure of nucleic acids," *Nature.*, vol. 171, no. 4356, pp. 737–8, 1953.

[76]   A. Rich and D. R. Davies, "A new two stranded helical structure: Polyadenylic acid and poly uridylic acid," *J Am Chem Soc*, vol. 78, no. 14, pp. 3548–3549, 1956.

[77]   R. W. HOLLEY *et al.*, "Structure of a Ribonucleic Acid," *Science (80-.).*, vol. 147, no. 3664, pp. 1462–1465, 1965.

[78]   P. Belmont, J. F. Constant, and M. Demeunynck, "Nucleic acid conformation diversity: from structure to function and regulation," *Chem. Soc. Rev.*, vol. 30, no. 1, pp. 70–81, 2001.

[79] D. Duzdevich, S. Redding, and E. C. Greene, "DNA dynamics and single-molecule biology," *Chem. Rev.*, vol. 114, no. 6, pp. 3072–3086, 2014.

[80] R. M. Voorhees and V. Ramakrishnan, "Structural basis of the translational elongation cycle. TL - 82," *Annu. Rev. Biochem.*, vol. 82 VN-r, pp. 203–236, 2013.

[81] D. Tinoco, I., Turner, D., Crothers, "Nucleic Acids," 1st ed., University Science Press, 2000.

[82] A. M. Mustoe, C. L. Brooks, and H. M. Al-Hashimi, "Hierarchy of RNA Functional Dynamics.," *Annu. Rev. Biochem.*, vol. 83, pp. 441–466, 2014.

[83] E. A. Dethoff, J. Chugh, A. M. Mustoe, and H. M. Al-Hashimi, "Functional complexity and regulation through RNA dynamics.," *Nature*, vol. 482, no. 7385, pp. 322–30, 2012.

[84] M. Gellert, M. N. Lipsett, and D. R. Davies, "Helix Formation By Guanylic Acid," *Proc. Natl. Acad. Sci.*, vol. 48, no. 12, pp. 2013–2018, 1962.

[85] J. T. Davis, "G-Quartets 40 Years Later: From 5'-GMP to Molecular Biology and Supramolecular Chemistry," *Angew. Chemie - Int. Ed.*, vol. 43, no. 6, pp. 668–698, 2004.

[86] J. Tang, Z. Y. Kan, Y. Yao, Q. Wang, Y. H. Hao, and Z. Tan, "G-quadruplex preferentially forms at the very 3′ end of vertebrate telomeric DNA," *Nucleic Acids Res.*, vol. 36, no. 4, pp. 1200–1208, 2008.

[87] J. Husby, A. K. Todd, J. A. Platts, and S. Neidle, "Small-molecule G-quadruplex interactions: Systematic exploration of conformational space using multiple molecular dynamics," *Biopolymers*, vol. 99, no. 12, pp. 989–1005, 2013.

[88] R. R. Breaker, "Riboswitches and the RNA World," pp. 1–15, 2010.

[89] W. Winkler, A. Nahvi, and R. R. Breaker, "Thiamine derivatives bind messenger RNAs directly to regulate bacterial gene expression.," *Nature*, vol. 419, no. 6910, pp. 952–6, 2002.

[90] M. Mandal, B. Boese, J. E. Barrick, W. C. Winkler, and R. R. Breaker, "Riboswitches control fundamental biochemical pathways in Bacillus subtilis and other bacteria," *Cell*, vol. 113, no. 5, pp. 577–586, 2003.

[91] K. F. Blount and R. R. Breaker, "Riboswitches as antibacterial drug targets," *Nat Biotechnol*, vol. 24, no. 12, pp. 1558–1564, 2006.

[92] R. Penchovsky and R. R. Breaker, "Computational design and experimental validation of oligonucleotide-sensing allosteric ribozymes.," *Nat. Biotechnol.*, vol. 23, no. 11, pp. 1424–1433, 2005.

[93] S. K. Desai and J. P. Gallivan, "Genetic screens and selections for small molecules based on a synthetic riboswitch that activates protein translation," *J. Am. Chem. Soc.*, vol. 126, no. 41, pp. 13247–13254, 2004.

[94] S. M. Elbashir, J. Harborth, W. Lendeckel, A. Yalcin, K. Weber, and T. Tuschl, "Duplexes of 21 ± nucleotide RNAs mediate RNA interference in cultured mammalian cells," *Nature*, vol. 411, no. 6836, pp. 494–498, 2001.

[95]   S. Iijima, "Helical microtubules of graphitic carbon," *Nature*, vol. 354, no. 6348, pp. 56–58, 1991.

[96]   A. G. Rinzler *et al.*, "Large-scale purification of single-wall carbon nanotubes: process, product, and characterization," *Appl. Phys. A Mater. Sci. Process.*, vol. 67, no. 1, pp. 29–37, 1998.

[97]   P. Nikolaev *et al.*, "Gas-phase catalytic growth of single-walled carbon nanotubes from carbon monoxide," *Chem. Phys. Lett.*, vol. 313, no. 1–2, pp. 91–97, 1999.

[98]   Z. Ren *et al.*, "Synthesis of large arrays of well-aligned carbon nanotubes on glass," *Science*, vol. 282, no. 5391, pp. 1105–7, 1998.

[99]   Z. P. Huang, J. W. Xu, Z. F. Ren, J. H. Wang, M. P. Siegal, and P. N. Provencio, "Growth of highly oriented carbon nanotubes by plasma-enhanced hot filament chemical vapor deposition," *Appl. Phys. Lett.*, vol. 73, no. 26, pp. 3845–3847, 1998.

[100]   Z. F. Ren *et al.*, "Growth of a single freestanding multiwall carbon nanotube on each nanonickel dot," *Appl. Phys. Lett.*, vol. 75, no. 8, pp. 1086–1088, 1999.

[101]   E. T. Thostenson, Z. Ren, and T.-W. Chou, "Advances in the science and technology of carbon nanotubes and their composites: a review," *Compos. Sci. Technol.*, vol. 61, no. 13, pp. 1899–1912, 2001.

[102]   V. Jourdain and C. Bichara, "Current understanding of the growth of carbon nanotubes in catalytic chemical vapour deposition," *Carbon N. Y.*, vol. 58, pp. 2–39, 2013.

[103]   M. Kumar and Y. Ando, "Chemical vapor deposition of carbon nanotubes: a review on growth mechanism and mass production.," *J. Nanosci. Nanotechnol.*, vol. 10, no. 6, pp. 3739–3758, 2010.

[104]   G. D. Nessim, "Properties, synthesis, and growth mechanisms of carbon nanotubes with special focus on thermal chemical vapor deposition," *Nanoscale*, vol. 2, no. 8, pp. 1306–1323, 2010.

[105]   Y. Li, W. Kim, Y. Zhang, M. Rolandi, D. Wang, and H. Dai, "Growth of single-walled carbon nanotubes from discrete catalytic nanoparticles of various sizes," *J. Phys. Chem. B*, vol. 105, no. 46, pp. 11424–11431, 2001.

[106]   C. Thomsen, S. Reich, and J. Maultzsch, "Resonant Raman spectroscopy of nanotubes.," *Philos. Trans. A. Math. Phys. Eng. Sci.*, vol. 362, no. 1824, pp. 2337–2359, 2004.

[107]   Y. Kataura, H; Kumazawa, Y; Maniwa, Y; Umezu, I; Suzuki, S; Ohtsuka, Y; Achiba, "Optical Properties of Single-Wall Carbon Nanotubes," *Synth. Met.*, vol. 103, pp. 1–4, 1999.

[108]   M. A. Pimenta, G. Dresselhaus, M. S. Dresselhaus, L. G. Cançado, A. Jorio, and R. Saito, "Studying disorder in graphite-based systems by Raman spectroscopy," *Phys. Chem. Chem. Phys.*, vol. 9, no. 11, pp. 1276–1291, 2007.

[109]   W. J. Bruno, G. Ullah, D. O. Daniel Mak, and J. E. Pearson, "Automated maximum likelihood separation of signal from baseline in noisy quantal data," *Biophys. J.*, vol. 105, no. 1, pp. 68–79, 2013.

[110] J. E. Bronson, J. Fei, J. M. Hofman, R. L. Gonzalez, and C. H. Wiggins, "Learning rates and states from biophysical time series: A Bayesian approach to model selection and single-molecule FRET data," *Biophys. J.*, vol. 97, no. 12, pp. 3196–3205, 2009.

[111] S. Niyogi *et al.*, "Chemistry of Single-Walled Carbon Nanotubes," pp. 1105–1113, 2002.

[112] X. Guo *et al.*, "Covalently bridging gaps in single-walled carbon nanotubes with conducting molecules.," *Science*, vol. 311, no. 5759, pp. 356–9, 2006.

[113] R. J. Chen, Y. Zhang, D. Wang, and H. Dai, "Noncovalent Sidewall Functionalization of Carbon Nanotubes for Protein Immobilization," *J. Am. Chem. Soc.*, vol. 123, no. 16, pp. 3838–3839, 2001.

[114] B. R. Goldsmith, J. G. Coroneus, V. R. Khalap, A. A. Kane, G. A. Weiss, and P. G. Collins, "Conductance-Controlled Point Functionalization of Single-Walled Carbon Nanotubes," *Science (80-.).*, vol. 315, no. 5808, pp. 77–81, 2007.

[115] J. G. Coroneus, B. R. Goldsmith, J. A. Lamboy, A. A. Kane, P. G. Collins, and G. A. Weiss, "Mechanism-guided improvements to the single molecule oxidation of carbon nanotube sidewalls," *ChemPhysChem*, vol. 9, no. 7, pp. 1053–1056, 2008.

[116] B. R. Goldsmith, J. G. Coroneus, a a Kane, G. a Weiss, and P. G. Collins, "Monitoring single molecule reactivity on a carbon nanotube," *Nano Lett.*, vol. 8, pp. 189–194, 2008.

[117] B. D. Gates, Q. Xu, M. Stewart, D. Ryan, C. G. Willson, and G. M. Whitesides, "New Approaches to Nanofabrication: Molding, Printing, and Other Techniques," *Chem. Rev.*, vol. 105, no. 4, pp. 1171–1196, 2005.

[118] J. L. Bahr and J. M. Tour, "Covalent chemistry of single-wall carbon nanotubes," *J. Mater. Chem.*, vol. 12, no. 7, pp. 1952–1958, 2002.

[119] M. L. Kovarik and S. C. Jacobson, "Nanofluidics in lab-on-a-chip devices," *Anal. Chem.*, vol. 81, no. 17, pp. 7133–7140, 2009.

[120] G. Schmidt, S. Gallon, S. Esnouf, J. P. Bourgoin, and P. Chenevier, "Mechanism of the coupling of diazonium to single-walled carbon nanotubes and its consequences," *Chem. - A Eur. J.*, vol. 15, no. 9, pp. 2101–2110, 2009.

[121] E. R. Margine, M.-L. Bocquet, and X. Blase, "Thermal Stability of Graphene and Nanotube Covalent Functionalization," *Nano Lett.*, vol. 8, no. 10, pp. 3315–3319, 2008.

[122] J. Cabana, S. Lavoie, and R. Martel, "Thermal Chemistry of Methylene- and Phenyl-Functionalized Carbon Nanotubes.," *J. Am. Chem. Soc.*, vol. 132, no. 4, pp. 1389–1394, 2010.

[123] D. Bouilly, J. L. Janssen, J. Cabana, M. Côté, and R. Martel, "Graft-Induced Midgap States in Functionalized Carbon Nanotubes," *ACS Nano*, vol. 9, no. 3, pp. 2626–2634, 2015.

[124] G. T. Hermanson, "The Reactions of Bioconjugation," in *Bioconjugate Techniques*, 3rd ed., 2013, pp. 229–258.

[125] H. McNab and L. C. Monahan, "3-Hydroxypyrroles and 1H-pyrrol-3(2H)-ones. Part 8. Reactions of 1-isopropyl-2,2-dimethyl-1H-pyrrol-3(2H)-one with electrophiles," *J. Chem.*

Soc. Perkin Trans. 1, vol. 53, no. 3, p. 419, 1989.

[126] C. Wang, Q. Cao, T. Ozel, A. Gaur, J. a. Rogers, and M. Shim, "Electronically selective chemical functionalization of carbon nanotubes: Correlation between Raman spectral and electrical responses," *J. Am. Chem. Soc.*, vol. 127, no. 32, pp. 11460–11468, 2005.

[127] R. Graupner, "Raman spectroscopy of covalently functionalized single-wall carbon nanotubes," *Journal of Raman Spectroscopy*, vol. 38, no. 6. pp. 673–683, 2007.

[128] A. López-Bezanilla, F. Triozon, S. Latil, X. Blase, and S. Roche, "Effect of the chemical functionalization on charge transport in carbon nanotubes at the mesoscopic scale," *Nano Lett.*, vol. 9, no. 3, pp. 940–944, 2009.

[129] H. Wilson *et al.*, "Electrical monitoring of sp3 defect formation in individual carbon nanotubes," *J. Phys. Chem. C*, vol. 120, no. 3, pp. 1971–1976, 2016.

[130] M. K. Ashraf, N. A. Bruque, R. R. Pandey, P. G. Collins, and R. K. Lake, "Effect of localized oxygen functionalization on the conductance of metallic carbon nanotubes," *Phys. Rev. B - Condens. Matter Mater. Phys.*, vol. 79, no. 11, pp. 1–11, 2009.

[131] N. Wrobel, M. Schinkinger, and V. M. Mirsky, "A novel ultraviolet assay for testing side reactions of carbodiimides.," *Anal. Biochem.*, vol. 305, no. 2, pp. 135–8, 2002.

[132] J. SantaLucia, H. T. Allawi, and P. A. Seneviratne, "Improved nearest-neighbor parameters for predicting DNA duplex stability," *Biochemistry*, vol. 35, no. 11, pp. 3555–3562, 1996.

[133] D. H. Turner, "Conformational Changes," in *Nucleic Acids: Structures, Properties, and Functions*, 1st ed., 2000, pp. 259–317.

[134] R. B. Schoch, J. Han, and P. Renaud, "Transport phenomena in nanofluidics," *Rev. Mod. Phys.*, vol. 80, no. 3, pp. 839–883, 2008.

[135] S. Burge, G. N. Parkinson, P. Hazel, A. K. Todd, and S. Neidle, "Quadruplex DNA: Sequence, topology and structure," *Nucleic Acids Res.*, vol. 34, no. 19, pp. 5402–5415, 2006.

[136] J. Y. Lee, B. Okumus, D. S. Kim, and T. Ha, "Extreme conformational diversity in human telomeric DNA.," *Proc. Natl. Acad. Sci. U. S. A.*, vol. 102, no. 52, pp. 18938–18943, 2005.

[137] L. Ying, J. J. Green, H. Li, D. Klenerman, and S. Balasubramanian, "Studies on the structure and dynamics of the human telomeric G quadruplex by single-molecule fluorescence resonance energy transfer," *Proc. Natl. Acad. Sci. U. S. A.*, vol. 100, no. 25, pp. 14629–14634, 2003.

[138] A. Ambrus, D. Chen, J. Dai, T. Bialis, R. A. Jones, and D. Yang, "Human telomeric sequence forms a hybrid-type intramolecular G-quadruplex structure with mixed parallel/antiparallel strands in potassium solution," *Nucleic Acids Res.*, vol. 34, no. 9, pp. 2723–2735, 2006.

[139] H. Sun, J. Ren, and X. Qu, "Carbon Nanomaterials and DNA: From Molecular Recognition to Applications," *Acc. Chem. Res.*, vol. 49, no. 3, pp. 461–470, 2016.

[140] X. Li, Y. Peng, J. Ren, and X. Qu, "Carboxyl-modified single-walled carbon nanotubes

selectively induce human telomeric i-motif formation.," *Proc. Natl. Acad. Sci. U. S. A.*, vol. 103, no. 52, pp. 19658–19663, 2006.

[141] A. Y. Q. Zhang and S. Balasubramanian, "The kinetics and folding pathways of intramolecular G-quadruplex nucleic acids," *J. Am. Chem. Soc.*, vol. 134, no. 46, pp. 19297–19308, 2012.

[142] R. D. Gray, L. Petraccone, J. O. Trent, and J. B. Chaires, "Characterization of a K+-induced conformational switch in a human telomeric DNA oligonucleotide using 2-aminopurine fluorescence," *Biochemistry*, vol. 49, no. 1, pp. 179–194, 2010.

[143] H. Deng and W. H. Braunlin, "Kinetics of sodium ion binding to DNA quadruplexes," *J. Mol. Biol.*, vol. 255, pp. 476–483, 1996.

[144] R. D. Gray, J. O. Trent, and J. B. Chaires, "Folding and unfolding pathways of the human telomeric G-quadruplex," *J. Mol. Biol.*, vol. 426, no. 8, pp. 1629–1650, 2014.

[145] R. Roy, S. Hohng, and T. Ha, "A practical guide to single-molecule FRET.," *Nat. Methods*, vol. 5, no. 6, pp. 507–516, 2008.

[146] H. Yin, R. Landick, and J. Gelles, "Tethered particle motion method for studying transcript elongation by a single RNA polymerase molecule.," *Biophys. J.*, vol. 67, no. 6, pp. 2468–2478, 1994.

[147] M. Mandal and R. R. Breaker, "Adenine riboswitches and gene activation by disruption of a transcription terminator," *Nat. Struct. Mol. Biol.*, vol. 11, no. 1, pp. 29–35, 2004.

[148] A. Serganov *et al.*, "Structural basis for discriminative regulation of gene expression by adenine- and guanine-sensing mRNAs," *Chem. Biol.*, vol. 11, no. 12, pp. 1729–1741, 2004.

[149] J. K. Wickiser, M. T. Cheah, R. R. Breaker, and D. M. Crothers, "The kinetics of ligand binding by an adenine-sensing riboswitch," *Biochemistry*, vol. 44, no. 40, pp. 13404–13414, 2005.

[150] J.-F. Lemay, J. C. Penedo, R. Tremblay, D. M. J. Lilley, and D. A. Lafontaine, "Folding of the Adenine Riboswitch," *Chem. Biol.*, vol. 13, no. 8, pp. 857–868, 2006.

[151] W. J. Greenleaf, K. L. Frieda, D. A. N. Foster, M. T. Woodside, and S. M. Block, "Direct observation of hierarchical folding in single riboswitch aptamers.," *Science*, vol. 319, no. 5863, pp. 630–3, 2008.

[152] K. L. Frieda and S. M. Block, "Direct observation of cotranscriptional folding in an adenine riboswitch.," *Science*, vol. 338, no. 6105, pp. 397–400, 2012.

[153] Z. Gong, Y. Zhao, C. Chen, and Y. Xiao, "Role of ligand binding in structural organization of add A-riboswitch aptamer: A molecular dynamics simulation," *J. Biomol. Struct. Dyn.*, vol. 29, no. 2, pp. 403–416, 2011.

[154] J. F. Lemay *et al.*, "Comparative study between transcriptionally- and translationally-acting adenine riboswitches reveals key differences in riboswitch regulatory mechanisms," *PLoS Genet.*, vol. 7, no. 1, 2011.

[155] K. L. Frieda and S. M. Block, "Direct Observation of Cotranscriptional Folding in an

Adenine Riboswitch," *Science (80-.).*, vol. 338, no. 6105, pp. 397–400, 2012.

[156] S. Nozinovic *et al.*, "The importance of helix P1 stability for structural pre-organization and ligand binding affinity of the adenine riboswitch aptamer domain," *RNA Biol.*, vol. 11, no. 5, pp. 83–82, 2014.

[157] J. L. Leroy, M. Kochoyan, T. Huynh-Dinh, and M. Gu??ron, "Characterization of base-pair opening in deoxynucleotide duplexes using catalyzed exchange of the imino proton," *J. Mol. Biol.*, vol. 200, no. 2, pp. 223–238, 1988.

[158] M. Kochoyan, G. Lancelot, and J. L. Leroy, "Study of structure, base-pair opening kinetics and proton exchange mechanism of the d-(AATTGCAATT) self-complementary oligodeoxynucleotide in solution," *Nucleeic Acids Res.*, vol. 16, no. 15, pp. 7685–7702, 1988.

[159] J. Leroy, D. Broseta, M. Gubronf, and E. Polytechnique, "Proton Exchange and Base-pair Kinetics of Poly (rA) poly (rU) and Poly (r1) poly (rC)," pp. 165–178, 1985.

[160] M. Guéron and J.-L. Leroy, "Base-Pair Opening in Double-Stranded Nucleic Acids," *Nucleic Acids Mol. Biol.*, vol. 6, pp. 1–22, 1992.

[161] S. D. Gilbert, C. D. Stoddard, S. J. Wise, and R. T. Batey, "Thermodynamic and Kinetic Characterization of Ligand Binding to the Purine Riboswitch Aptamer Domain," *J. Mol. Biol.*, vol. 359, no. 3, pp. 754–768, 2006.

[162] V. Delfosse *et al.*, "Riboswitch structure: An internal residue mimicking the purine ligand," *Nucleic Acids Res.*, vol. 38, no. 6, pp. 2057–2068, 2009.

[163] J. Buck, B. Fürtig, J. Noeske, J. Wöhnert, and H. Schwalbe, "Time-resolved NMR methods resolving ligand-induced RNA folding at atomic resolution.," *Proc. Natl. Acad. Sci. U. S. A.*, vol. 104, no. 40, pp. 15699–15704, 2007.

[164] J. Noeske, J. Buck, B. Fürtig, H. R. Nasiri, H. Schwalbe, and J. Wöhnert, "Interplay of 'induced fit' and preorganization in the ligand induced folding of the aptamer domain of the guanine binding riboswitch," *Nucleic Acids Res.*, vol. 35, no. 2, pp. 572–583, 2007.

[165] O. M. Ottink, S. M. Rampersad, M. Tessari, G. J. Zaman, H. A. Heus, and S. S. Wijmenga, "Ligand-induced folding of the guanine-sensing riboswitch is controlled by a combined predetermined induced fit mechanism," *Rna*, vol. 13, no. 12, pp. 2202–2212, 2007.

[166] M. D. Brenner, M. S. Scanlan, M. K. Nahas, T. Ha, and S. K. Silverman, "Multivector fluorescence analysis of the xpt guanine riboswitch aptamer domain and the conformational role of guanine," *Biochemistry*, vol. 49, no. 8, pp. 1596–1605, 2010.

[167] D. C. Ward, E. Reich, and L. Stryer, "Fluorescence studies of nucleotides and polynucleotides," *J. Bioloi Chem.*, vol. 244, no. 5, pp. 1228–1237, 1969.

[168] J. F. Milligan and O. C. Uhlenbeck, "Synthesis of small RNAs using T7 RNA polymerase," *Methods Enzymol.*, vol. 180, pp. 51–62, 1989.

[169] J. Noeske, H. Schwalbe, and J. W??hnert, "Metal-ion binding and metal-ion induced folding of the adenine-sensing riboswitch aptamer domain," *Nucleic Acids Res.*, vol. 35, no. 15, pp. 5262–5273, 2007.

[170] GE Dharmacon, "Deprotection 2 â€™ - ACE Protected RNA," p. 9880, 2014.

[171] J.-W. van de Meent, J. E. Bronson, F. Wood, R. L. Gonzalez, and C. H. Wiggins, "Hierarchically-coupled hidden Markov models for learning kinetic rates from single-molecule data," *J. Mach. Learn. Res. Work. Conf. Proc.*, vol. 28, no. 2, pp. 361–369, 2013.

[172] M. Zuker, "Mfold web server for nucleic acid folding and hybridization prediction," *Nucleic Acids Res.*, vol. 31, no. 13, pp. 3406–3415, 2003.

[173] S. F. Tolic-Norrelykke, A. M. Engh, R. Landick, and J. Gelles, "Diversity in the Rates of Transcript Elongation by Single RNA Polymerase Molecules," *J. Biol. Chem.*, vol. 279, no. 5, pp. 3292–3299, 2004.

[174] K. Adelman, A. La Porta, T. J. Santangelo, J. T. Lis, J. W. Roberts, and M. D. Wang, "Single molecule analysis of RNA polymerase elongation reveals uniform kinetic behavior.," *Proc. Natl. Acad. Sci. U. S. A.*, vol. 99, no. 21, pp. 13538–13543, 2002.

[175] J. Yu, J. Xiao, X. Ren, K. Lao, and X. S. Xie, "Probing gene expression in live cells, one protein molecule at a time.," *Science*, vol. 311, no. 5767, pp. 1600–1603, 2006.

[176] S. V. Kuznetsov and A. Ansari, "A kinetic zipper model with intrachain interactions applied to nucleic acid hairpin folding kinetics," *Biophys. J.*, vol. 102, no. 1, pp. 101–111, 2012.

[177] W. Zhang and S.-J. Chen, "RNA hairpin-folding kinetics," *Proc. Natl. Acad. Sci. U. S. A.*, vol. 99, no. 4, pp. 1931–6, 2002.

[178] S. Cocco, J. F. Marko, and R. Monasson, "Slow nucleic acid unzipping kinetics from sequence-defined barriers," *Eur. Phys. J. E*, vol. 10, no. 2, pp. 153–161, 2003.

[179] D. Porschke, "A direct measurement of the unzippering rate of a nucleic acid double helix," *Biophys. Chem.*, vol. 2, no. 2, pp. 97–101, 1974.

[180] M. T. Woodside, P. C. Anthony, W. M. Behnke-Parks, K. Larizadeh, D. Herschlag, and S. M. Block, "Direct measurement of the full, sequence-dependent folding landscape of a nucleic acid.," *Science*, vol. 314, no. 5801, pp. 1001–4, 2006.

[181] C. A. Morgado, D. Svozil, D. H. Turner, and J. Šponer, "Understanding the role of base stacking in nucleic acids. MD and QM analysis of tandem GA base pairs in RNA duplexes.," *Phys. Chem. Chem. Phys.*, vol. 14, no. 36, pp. 12580–91, 2012.

[182] A. Lescoute and E. Westhof, "Topology of three-way junctions in folded RNAs.," *RNA*, vol. 12, no. 1, pp. 83–93, 2006.

[183] J. K. Wickiser, W. C. Winkler, R. R. Breaker, and D. M. Crothers, "The speed of RNA transcription and metabolite binding kinetics operate an FMN riboswitch," *Mol. Cell*, vol. 18, no. 1, pp. 49–60, 2005.

[184] B. Lutz, M. Faber, A. Verma, S. Klumpp, and A. Schug, "Differences between cotranscriptional and free riboswitch folding," *Nucleic Acids Res.*, vol. 42, no. 4, pp. 2687–2696, 2014.

[185] I. Artsimovitch, V. Svetlov, L. Anthony, R. Burgess, R. Landick, and R. R. Burgess, "RNA Polymerases from Bacillus subtilis and Escherichia coli Differ in Recognition of

Regulatory Signals In Vitro RNA Polymerases from Bacillus subtilis and Escherichia coli Differ in Recognition of Regulatory Signals In Vitro," 2000.

[186] N. Komissarova and M. Kashlev, "Functional topography of nascent RNA in elongation intermediates of RNA polymerase.," *Proc. Natl. Acad. Sci. U. S. A.*, vol. 95, no. 25, pp. 14699–14704, 1998.

[187] J. a Monforte, J. D. Kahn, and J. E. Hearst, "RNA folding during transcription by Escherichia coli RNA polymerase analyzed by RNA self-cleavage.," *Biochemistry*, vol. 29, no. 34, pp. 7882–90, 1990.

[188] P. P. Gardner *et al.*, "Rfam : updates to the RNA families database," vol. 37, no. October 2008, pp. 136–140, 2009.